ARO 24988.1-EL

②

SOLID STATE ELECTRONICS LABORATORY

STANFORD ELECTRONICS LABORATORIES
DEPARTMENT OF ELECTRICAL ENGINEERING
STANFORD UNIVERSITY · STANFORD, CA 94305

DIRECT IMPLANTATION PROCESS DEVELOPMENT AND CHARACTERIZATION IN ADVANCED $Hg_{1-x}Cd_xTe$ EPI LAYERS

Final Report

by

Thomas W. Sigmon

U. S. Army Research Office

November 1989

Prepared under

DTIC
ELECTE
MAR 0 1 1990
S E D

90 02 26 061

THE VIEW, OPINIONS, AND/OR FINDINGS CONTAINED IN THIS
REPORT ARE THOSE OF THE AUTHOR(S) AND SHOULD NOT BE
CONSTRUED AS AN OFFICIAL DEPARTMENT OF THE ARMY POSITION,
POLICY, OR DECISION, UNLESS SO DESIGNATED BY OTHER
DOCUMENTATION.

REPORT DOCUMENTATION PAGE

1a. REPORT SECURITY CLASSIFICATION	1b. RESTRICTIVE MARKINGS
Unclassified	

2a. SECURITY CLASSIFICATION AUTHORITY	3. DISTRIBUTION / AVAILABILITY OF REPORT
	Approved for public release;
2b. DECLASSIFICATION / DOWNGRADING SCHEDULE	distribution unlimited.

4. PERFORMING ORGANIZATION REPORT NUMBER(S)	5. MONITORING ORGANIZATION REPORT NUMBER(S)
	ARO 24988.1-EL

6a. NAME OF PERFORMING ORGANIZATION	6b. OFFICE SYMBOL (If applicable)	7a. NAME OF MONITORING ORGANIZATION
The Board of Trustees of the Leland Stanford Junior University		U. S. Army Research Office

6c. ADDRESS (City, State, and ZIP Code)	7b. ADDRESS (City, State, and ZIP Code)
Sponsored Projects Office 125 Panama Street Stanford, CA 94305	P.O. Box 12211 Research Triangle Park, NC 27709-2211

8a. NAME OF FUNDING / SPONSORING ORGANIZATION	8b. OFFICE SYMBOL (If applicable)	9. PROCUREMENT INSTRUMENT IDENTIFICATION NUMBER
U. S. Army Research Office		DAAL03-87-k-0109

8c. ADDRESS (City, State, and ZIP Code)	10. SOURCE OF FUNDING NUMBERS			
P.O. Box 12211 Research Triangle Park, NC 27709-2211	PROGRAM ELEMENT NO.	PROJECT NO.	TASK NO.	WORK UNIT ACCESSION NO

11. TITLE (Include Security Classification)
Direct Implantation Process Development and Characterization in Advanced $Hg_{1-x}Ce_xTe$ EPI Layers

12. PERSONAL AUTHOR(S)
Thomas W. Sigmon

13a. TYPE OF REPORT	13b. TIME COVERED	14. DATE OF REPORT (Year, Month, Day)	15. PAGE COUNT
Final	FROM 10/1/87 TO 11/30/89	November 1989	151

16. SUPPLEMENTARY NOTATION The view, opinions and/or findings contained in this report are those of the author(s) and should not be construed as an official Department of the Army position, policy, or decision, unless so designated by other documentation.

17.	COSATI CODES		18. SUBJECT TERMS (Continue on reverse if necessary and identify by block number)
FIELD	GROUP	SUB-GROUP	$Hg_{1-x}Cd_xTe$, Ion Implantation, Rapid Thermal Annealing, Rapid Theramal Annealing, Ion Channeling, Rutherford Backscattering Spectrometry, Process Modeling, Lasers, Semiconductors

19. ABSTRACT (Continue on reverse if necessary and identify by block number)

Planer device fabrication processes, such as offered by ion implantation are highly desirable for the production of $Hg_{1-x}Cd_xTe$ infrared photovoltaic focal plane arrays. Unfortunately, implantation is a poorly understood process in this material with damage layers frequently being used to form n^+-p junctions. Junctions formed using activated dopants are expected to have several advantages over defect doping and thus warrant evaluation.

In an effort to better understand the results of implantation in MCT, we have calculated ion and damage profiles. Comparison of calculated atom ranges and profiles to π data has been carried out to evaluate the accuracy of the calculations and make appropriate changes. Systematic changing of the implant parameters has been performed and related to experimentally obtained parameters such as damage and electrical performance of the implanted layers.

20. DISTRIBUTION / AVAILABILITY OF ABSTRACT	21. ABSTRACT SECURITY CLASSIFICATION
☒ UNCLASSIFIED/UNLIMITED ☐ SAME AS RPT. ☐ DTIC USERS	Unclassified

22a. NAME OF RESPONSIBLE INDIVIDUAL	22b. TELEPHONE (Include Area Code)	22c. OFFICE SYMBOL

DD FORM 1473, 84 MAR   83 APR edition may be used until exhausted.   SECURITY CLASSIFICATION OF THIS PAGE

All other editions are obsolete.   UNCLASSIFIED

ABSTRACT

A planar device fabrication process, such as that offered by ion implantation, is highly desirable for the production of $Hg_{1-x}Cd_xTe$ (MCT) infrared photovoltaic focal plane arrays. Unfortunately, implantation is still a poorly understood process in this material. Implantation of "anything" into MCT causes the formation of an n^+ layer due to radiation damage. This damaged layer is frequently used to form n^+-p junctions without annealing because of the tendency of MCT to lose Hg even under very mild annealing conditions. Devices with excellent properties have been made using these "damage junctions", but the junction depths and carrier profiles of junctions formed in this manner are highly dependent on the structure of residual implant damage and background impurities. Junctions formed using activated dopants are expected to have several advantages over defect doping, but just as in silicon the optimal annealing procedure will depend on the level and structure of residual implant damage. Thus, whichever method of junction formation is chosen, it is obvious that a detailed understanding of ion ranges and damage production as a function of implant parameters is at least as important in MCT as it is in Si and GaAs device fabrication.

In an effort to better understand the effects of implantation in MCT we calculated ion and damage profiles using two implant simulators, the Boltzmann Transport Equation method and TRIM. Comparison of calculated atom ranges and profiles to SIMS data taken from our own experiments and data from the literature allowed us to modify the implant simulators and obtain excellent agreement between calculation and experiment for a wide range of implanted ion masses and energies. We also studied the effects of systematically changing implant parameters such as ion mass, ion energy, target temperature, and ion current by relating residual implant damage as measured by MeV ion channeling to van der Paaw-Hall measurements, damage calculations, and calculations of ion beam heating. These measurements show that residual implant damage depends more strongly on the

density of energy deposition than on the total deposited energy. We find that dynamic annealing is more efficient for lower deposited energy densities, resulting in lower damage levels as measured by channeling and consistently higher sheet carrier concentrations in as-implanted material. We also investigated the repair of implant damage and the activation of four different implanted ions as a function of annealing step using the above characterization methods as well as low temperature photoluminescence. After the multiple step annealing sequence, the boron and indium implanted samples are n-type while the neon and fluorine implanted samples revert to p-type activity. Also, photoluminescence reappears after annealing and is actually more intense than before implantation. These observations indicate that the electrically active damage is repaired by annealing and that the n-type activity observed in the boron and indium experiments is due to activation of the implanted ions.

CONTENTS

CHAPTER 1 – INTRODUCTION

CHAPTER 2 – EXPERIMENTAL TECHNIQUES

CHAPTER 3 – AS-IMPLANTED ION PROFILES AND DAMAGE: CALCULATION AND EXPERIMENT

LIST OF TABLES

LIST OF FIGURES

SYMBOLS

a	Screening parameter
a_0	Bohr radius (Å)
C_p	Heat capacity (J K^{-1} cm^{-3})
dE/dx	Energy loss per unit length (MeV/cm)
$dE/dx)_{ch}$	Energy loss per unit length in channeling mode (MeV/cm)
$dE/dx)_R$	Energy loss per unit length in random mode (MeV/cm)
d_i	Thickness of layer removed (cm)
dQ	Number of backscattered particles detected
e	Electronic charge
E	Energy of incident particle just before scattering (MeV)
E_A	Energy of acceptor level (eV)
E_b	Binding energy of atoms in target (eV)
E_c	Incident energy at which nuclear stopping is equal to electronic stopping
E_d	Displacement energy (eV)
E_D	Energy of donor level (eV)
E_g	Band gap (eV)
E_x	Exciton binding energy (eV)
E_0	Primary beam energy (MeV)
E_1	Energy of incident particle immediately after elastic collision (MeV)
E_2	Energy of target atom immediately after elastic collision (MeV)
ΔE	Energy straggling of incident particles (MeV)
F(p)	Momentum distribution function (BTE)
f(r/a)	Screening function
h	Planck's constant
H	Heat transfer coefficient (W/K)
k	Wave vector
k	Proportionality constant in LSS expression for electronic stopping
k_b	Boltzmann's constant
K_{M_2}	Kinematic factor for scattering off target atom M_2
L	Intensity of emission spectrum
M_1	Atomic mass of incident particle (amu)
M_2	Atomic mass of target atom (amu)
n_e	Density of free electrons (cm^{-3})
n_h	Density of free holes (cm^{-3})

n_i	Carrier concentration of ith layer (cm^{-3})
N	Atomic or molecular density for elemental or compound targets (cm^{-3})
N_A	Acceptor concentration (cm^{-3})
N_C	Density of states in conduction band (cm^{-3})
N_d	Total active dose (cm^{-2})
N_S	Sheet carrier concentration (cm^{-2})
N_V	Density of states in valence band (cm^{-3})
p	Exponent in LSS expression for electronic stopping
P_r	Radiative power transferred between wafer and surroundings
q	Electronic charge
Q	Number of incident alpha particles
$Q(\mathbf{p})$	Recoiled particles (BTE)
$Q(z)$	Energy deposited as heat during implantation
r	Separation distance (Å)
R	Ion range (μm or Å)
R_p	Projected range (μm or Å)
ΔR_p	Ion range straggle (μm or Å)
R_H	Sheet Hall coefficient
R_s	Sheet resistivity (Ω/sq)
S_e	Electronic stopping power (eV cm^2)
S_n	Nuclear stopping power (eV cm^2)
t	distance (thickness) traveled by an ion (cm)
T	Energy transferred from incident ion to target atom in an elastic collision (MeV)
T	Temperature (K or °C)
T_s	Temperature of surroundings
T_w	Wafer temperature
T_{wh}	Temperature of wafer holder
$V(r)$	Interatomic potential
x	Mole fraction of CdTe present
z	Distance into sample (BTE)
Z_1	Atomic number of incident particle
Z_2	Atomic number of target atom
β	Kurtosis
ϵ	Stopping cross section (eV cm^2)
ϵ	Dielectric constant
ϵ	Dimensionless energy (LSS)

ε^i	Stopping cross section (eV cm^2) of atomic species i
ε_m	Maximum in universal nuclear stopping curve
ε_s	Emissivity of surroundings
ε_w	Emissivity of wafer
γ	Skewness
κ	Thermal conductivity (W cm^{-1} K^{-1})
μ	Hall mobility (cm^2 V^{-1} s^{-1})
μ_i	Hall mobility (cm^2 V^{-1} s^{-1}) of ith layer
ν	Photon frequency
θ	Angle of scattered beam with respect to incident beam
ρ	Dimensionless range (LSS)
ρ	Density (g cm^{-3})
χ_{min}	Minimum yield
σ	Scattering cross section (cm^2)
σ	Stefan-Boltzmann constant
τ	Characteristic time in Morehead and Crowder theory (s)
$d\Omega$	Detector solid angle (steradians)

Chapter 1

Introduction

1.1 Background

Mercury cadmium telluride (MCT) has been extensively studied over the past thirty years, primarily as an optical detector material for the mid and far infrared. More recently researchers have also shown interest in other potential uses for the material such as optical communication devices, [1.1, 1.2] tunable lasers, and nonlinear optical devices [1.3].

The properties that make the alloy semiconductor MCT particularly suited for infrared detection include an energy gap that can be adjusted from a value of -0.3 eV for the semimetal HgTe to 1.6 eV for CdTe and a direct energy gap over all values of composition. The direct energy gap gives the material a large absorption coefficient which means that the detector needs to be only several microns thick to absorb all the radiation of interest. It thus lends itself readily to production-line processing utilizing standard photolithographic techniques. Additional favorable properties include a very high electron mobility, a high electron-to-hole mobility ratio, and a fairly low dielectric constant.

Most current research centers around the development of infrared detectors and imaging arrays sensitive to the wavelengths of the two atmospheric windows, 3-5 μm and 8-14 μm. These wavelengths correspond to alloy compositions of $0.3 \leq x \leq 0.4$ and $x \approx 0.22$, respectively, as shown in Fig. 1.1, where x is the mole fraction of CdTe in solution. The atmospheric windows are of great interest for communication and military applications. In addition, the maximum of thermal radiation emitted by room temperature bodies occurs at about 10 μm so that detectors operating in this region are useful for measuring temperature gradients in the environment and in medical applications.

Both photoconductive (PC) and photovoltaic (PV) detectors can be fabricated in MCT. The first generation of MCT detectors were linear PC arrays composed of up to 200
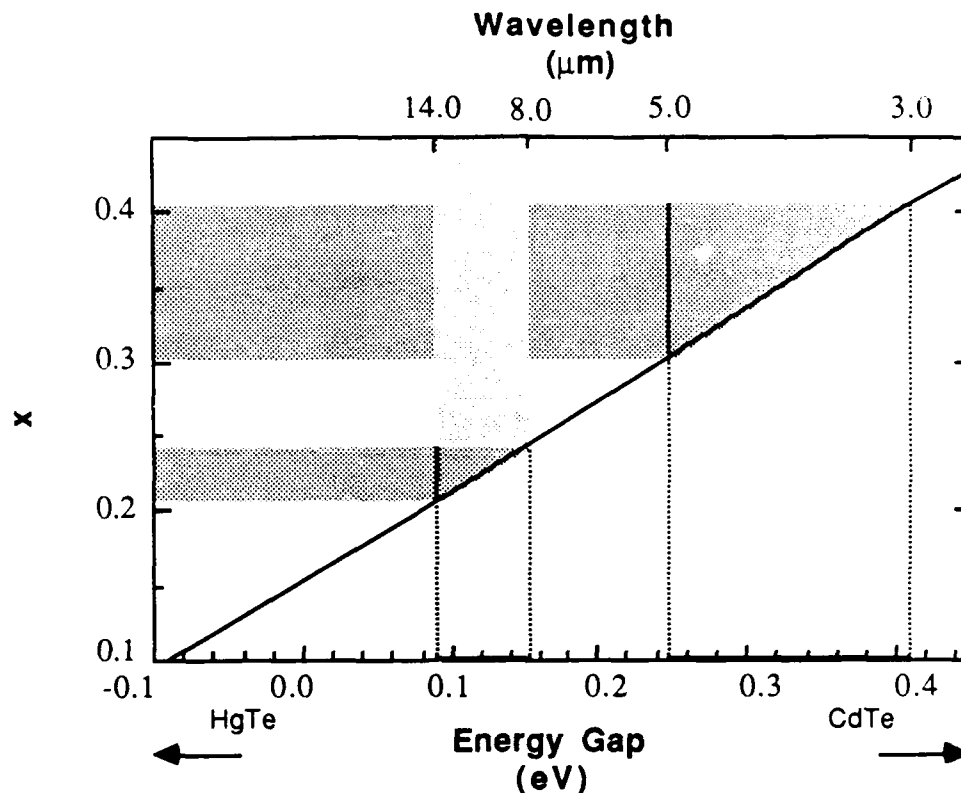
Wavelength
(μm)

Fig. 1.1 The relation between composition and energy gap for $Hg_{1-x}Cd_xTe$ at 77 K for $0.1 \leq x \leq 0.45$. The alloy compositions with band gaps corresponding to the wavelengths of the two atmospheric windows, 3 - 5 μm and 8 - 14 μm, are indicated. E_g versus x is calculated using the expression reported in [1.4].

discrete detectors operating near 77 K and coupled to the outside world by individual bias

and preamplifier leads [1.5]. Though PC technology is now mature, PV mode devices are

viewed as better candidates for future focal plane arrays because of the need to minimize

power dissipation. Unlike PC devices, PV mode devices require no bias current to operate

and they have a high impedance so they can match directly into the input stage of a silicon

CCD. Each PC device requires its own preamplifier which not only dissipates more

power, but occupies more space on the chip.

PV mode operation requires the presence of a space charge region whose internal

electric field separates photogenerated electron-hole pairs and creates either an open circuit

photovoltage or a short circuit photocurrent. This is commonly achieved with a p-n

junction. Many methods of junction formation have been tried in MCT, but Hg in-diffusion and especially ion implantation appear to be the most promising for preparing high-performance infrared photodiodes [1.6].

Ion implantation in Si and GaAs is well understood, convenient, and controllable. With these materials the conventional process is to anneal devices following implantation to repair the radiation damage. This reduces the noise sources, improves the mobility, and increases the activation of the implanted ions because it allows most of them to move onto lattice sites in the target. The situation in MCT, however, is somewhat more complicated. The tendency of MCT to lose Hg under even very mild annealing conditions is well known and only recently has a promising post-implant annealing process, involving a native oxide cap and a multiple stage anneal, been developed [1.7, 1.8]. To make p-n junctions before the development of an annealing process workers took advantage of the fact that as-implanted samples of MCT always exhibit n-type conductivity independent of the implanted ion or the carrier type of the substrate — "anything" implanted into MCT results in an n^+-p junction. The n-type activity is thus attributed to radiation damage rather than activation of the implanted atom, though the electrically active defects are as yet unidentified. Devices with excellent characteristics are produced using this "damage junction" approach [1.9], but there are several disadvantages to this method. Junction depths and carrier profiles are heavily dependant on the initial defect structure and residual impurities in the samples as well as the damage profiles resulting from implantation [1.10, 1.11]. Also, damage junction properties are likely to be unstable to the heat treatments used in subsequent processing and to the frequent temperature cycling finished devices experience (many devices are operated at 77 K). Thus it is accepted that true dopant activation involving a post-implant anneal is preferable to the use of damage junctions because it would allow precise control of doping concentration profiles and accurate prediction of junction position.

For the case of a "damage junction" the structure of the implant-induced damage determines the junction depth and carrier profile. For an annealed junction, just as with silicon and gallium arsenide, the structure of the residual implant damage will have a strong influence on the optimal annealing process. Thus whichever method of junction formation is chosen, it is obviously important to have a better understanding of the residual damage remaining after implantation. In addition, once the multiple stage annealing process has been optimized, it will be necessary to be able to calculate ion ranges and profiles, since the ion profile will then be controlling the carrier profile of the junction.

An early objective of this work was thus to calculate implanted atom and damage profiles in MCT for a variety of ions and implant energies. Atom ranges and profiles were compared to SIMS data taken from our own experiments as well as data from the literature. In addition, we examined the effects of systematically changing implant parameters such as ion mass, ion energy, target temperature, and ion current by relating residual implant damage as measured by MeV ion channeling to van der Pauw-Hall measurements and damage calculations. We also investigated the repair of implant damage and the activation of implanted ions as a function of annealing stage for several different implanted ions using the same characterization methods as above as well as low temperature photoluminescence.

1.2 Organization

This thesis is divided into six chapters addressing the major topics covered. The first chapter gives some background on the uses of MCT and outlines some of the fundamental problems of ion implantation in the material. In Chapter 2 we describe the experimental techniques used in preparing, implanting, and characterizing samples. The fundamentals of ion implantation are discussed in Chapter 3 along with the models used to calculate implanted atom and damage profiles. These calculations are then compared with SIMS measurements and the structural and electrical properties of as-implanted samples.

Chapter 4 addresses rate effects in implantation. We calculate the transient temperature rise caused by the ion beam and compare it to experiment and discuss the effects of dose and damage rate. Experiments on annealing and dopant activation are described in Chapter 5 for four implanted ions, boron, indium, neon, and fluorine. Chapter 6 summarizes this thesis and gives suggestions for future work.

1.3   Contributions

The primary contributions of this work are:

1) Atom and damage profiles have been calculated using the BTE method and TRIM as a function of energy for ^{4}He, ^{9}Be, ^{11}B, ^{19}F, ^{20}Ne, ^{27}Al, ^{35}Cl, ^{114}Cd, ^{115}In, ^{127}I, and ^{130}Te. Calculated ion ranges agree well with empirical data from the literature and calculated boron and indium profiles are in excellent agreement with SIMS measurements performed for this thesis. Damage as measured by MeV ion channeling follows the general trends predicted by the calculations.

2) Residual damage in as-implanted MCT is shown to be strongly dependent on collision cascade density and implant temperature. Low cascade densities and higher temperatures result in more "efficient" dynamic annealing and thus lower damage levels.

3) Lower density collision cascades and higher implant temperatures are found to consistently result in higher sheet carrier concentrations in as-implanted MCT. This suggests that several types of defects are formed by dynamic annealing, some electrically active and some not. Less "efficient" annealing promotes the formation of electrically inactive defects.

4) A computer code was written to calculate the transient temperature rise occurring as an ion beam passes over a spot on a MCT sample. The calculated temperature rise is found to be acceptable for the low beam currents typically used for implanting MCT.

5) Ion channeling results indicate that beam heating in combination with ion beam-induced epitaxy can significantly affect the profile of residual implantation damage in poorly heat sunk samples implanted at low temperatures.

6) Residual implantation damage as measured by RBS is found not to depend upon the current (dose rate) for values ranging from 0.2 to 5 μA.

7) A multiple step anneal removes almost all of the implantation induced damage that can be seen with MeV ion channeling, leaving behind a low level of defects. Bright photoluminescence spectra measured in post-implant annealed samples indicate these remaining defects are not detrimental.

8) It was confirmed that native oxide encapsulation and multiple stage annealing of boron-implanted MCT results in partial activation of boron through comparison with results for an inert (neon) implant undergoing identical annealing conditions. Annealed indium-implanted samples also show n-type activity, though fluorine implanted samples return to p-type activity.

9) SIMS results confirm that boron is relatively immobile in MCT under these processing conditions. Indium shows little movement due to the first two annealing steps, but most is lost through the surface during Anneal 3, indicating that improvements are needed in oxide growth. Following annealing, fluorine redistributes into a double peak structure due to decoration of defects and segregation as damage is repaired.

10) Photoluminescence is quenched in as-implanted samples, but reappears following the first annealing stage and increases in intensity with subsequent anneals. We see no evidence of near band gap defect levels induced by implantation in our luminescence spectra nor do we see any additional transitions due to dopant activation.

11) Photoluminescence intensity following post-implant annealing is up to 50 x brighter than that from unimplanted samples, indicating annealing removes other non-radiative centers from the material.

12) We observe a long wavelength peak in both unimplanted and post-implant annealed material that, to the best of our knowledge has not been previously reported from PL spectra of MCT of this composition. Though our measurements indicate that the peak energy is closer to $\frac{2E_g}{3}$, uncertainties in the composition-band gap relation and peak location make it possible that this peak can be identified with the $\frac{3E_g}{4}$ peak observed using DLTS.

1.4 References

[1.1]   R. Alabedra, B. Orsal, G. Lecoy, G. Pichard, J. Meslage, and P. Fragnon, IEEE Trans. Elec. Dev., **ED-32**(7), 1302 (1985).

[1.2]   T. Nguyen Duy, J. Meslage, and G. Pichard, J. Crys. Growth **72**, 490 (1985).

[1.3]   P.W. Kruse and J.F. Ready, "Nonlinear Optical Effects in $Hg_{1-x}Cd_xTe$" in *Semiconductors and Semimetals*, 16, Ed. Willardson and Beer, Academic Press Inc, New York, 1981.

[1.4]   G.L. Hansen, J.L. Schmit, and T.N. Casselmann, J. Appl. Phys. **53**, 7099 (1982).

[1.5]   R.K. Willardson and A.C. Beer, in Preface to *Semiconductors and Semimetals*, 18, Academic Press Inc, New York, 1981.

[1.6]   M.A. Herman and M. Pessa, J. Appl. Phys. **57**(8), 2671 (1985).

[1.7]   T.-M. Kao, T.W. Sigmon, and L.O. Bubulac, J. Vac. Sci. Technol. A **5**(5), 3175 (1987).

[1.8]   T.-M. Kao, Development of Direct Ion Implantation Processes and Characterization Techniques for Mercury Cadmium Telluride Epilayers, Ph.D. Thesis, Stanford University, May 1987.

[1.9]   G.L. Destefanis, J. Vac. Sci. Technol. A, **3**(1), 171 (1985).

[1.10] L.O. Bubulac, Appl. Phys. Lett. **46**(10), 976 (1985).

[1.11] L.O. Bubulac, W.E. Tennant, R.A. Riedel, and T.J. Magee, J. Vac. Sci. Technol., **21**(1), 251 (1982).

Chapter 2

Experimental Techniques

2.1 Introduction

As stated in the introductory chapter, this thesis studies the effects of various ion implantation parameters on the properties of annealed and as-implanted $Hg_{1-x}Cd_xTe$. This chapter describes the experimental techniques used in preparing, implanting, and characterizing samples. Preparation techniques common to the samples used in this thesis are described in §2.2 and the measurement techniques used used to evaluate the samples, including RBS, MeV ion channeling, van der Pauw measurements, photoluminescence, and SIMS are discussed in §2.3.

2.2 Sample Preparation

The material used in this work was p-type MCT (x = 0.3) grown by liquid phase epitaxy on CdTe or CdZnTe substrates. Typical electrical properties before implantation are $N_A = 1\text{-}3 \times 10^{16}$ cm^{-3} (attributed to Hg vacancies) with a Hall mobility of 300-400 cm^{2}V^{-1}s^{-1} at 77 K. The as-received epilayers are degreased and then etched back 4 to 5 microns in a dilute bromine methanol solution to remove any surface damage layer. The final layer thickness is about 19 µm. Before any further processing, the electrical properties are checked on representative samples with van der Pauw measurements and the x-value and structural quality of the epilayers are checked using RBS and MeV ion channeling. For implantation the samples are varnished (GE-7301) onto a silicon wafer which is then carefully mounted on a sample stage with thermally conducting paste. Implants are usually done at low current (< 1.5 µA cm^{-2}) to avoid any heating by the ion beam. The problem of beam heating will be discussed in more detail in Chapter 4. Following implantation the thermal paste is removed from the back of the silicon with isopropyl alcohol and a cotton swab after which the samples can be removed from the silicon by soaking in methanol. A thin native oxide layer ($\approx$ 200 Å) is then

photochemically grown on each sample in ozone using the process described in [2.1]. The encapsulated samples undergo a multi-stage anneal which consists of a 200° C furnace anneal in flowing N_2, a 320° C rapid thermal anneal in Ar, and another 200° C furnace anneal in flowing N_2. This annealing sequence will be described in more detail in chapter 5. The native oxide is removed after the anneal using an HCl etch. Electrical, structural, and optical properties are examined after implantation and following each annealing step using methods outlined in §2.3.

2.3 Measurement Techniques

2.3.1 Introduction

Measurement techniques for ion implantation effects must be able to give information specifically about the top one or two microns of the sample because of the low penetration depth of implanted ions. This is particularly true of MCT in which the range of even a light ion at a fairly high energy such as 250 keV ^{11}B is only around half a micron. Ideally, the profile shape of the implanted distribution (ion profile, damage profile, or electrically active profile) is obtained, but often integral information of the implanted distribution must be adequate, because of measurement sensitivity. For stoichiometry measurements and measurements of the structural damage caused by the implants, Rutherford Backscattering Spectrometry (RBS) and channeling RBS were chosen. Evaluation of the effects of implantation on the electrical properties of the samples before and after annealing was done using sheet and differential van der Pauw measurements. Effects of the implants on radiative transitions between the near bandgap states were measured using low temperature photoluminescence. Implanted and post-implant annealed ion profiles were measured using SIMS.

2.3.2 Rutherford Backscattering Spectrometry

Rutherford Backscattering Spectrometry is a fast, nondestructive technique that, together with ion channeling, can provide quantitative information on both the atomic
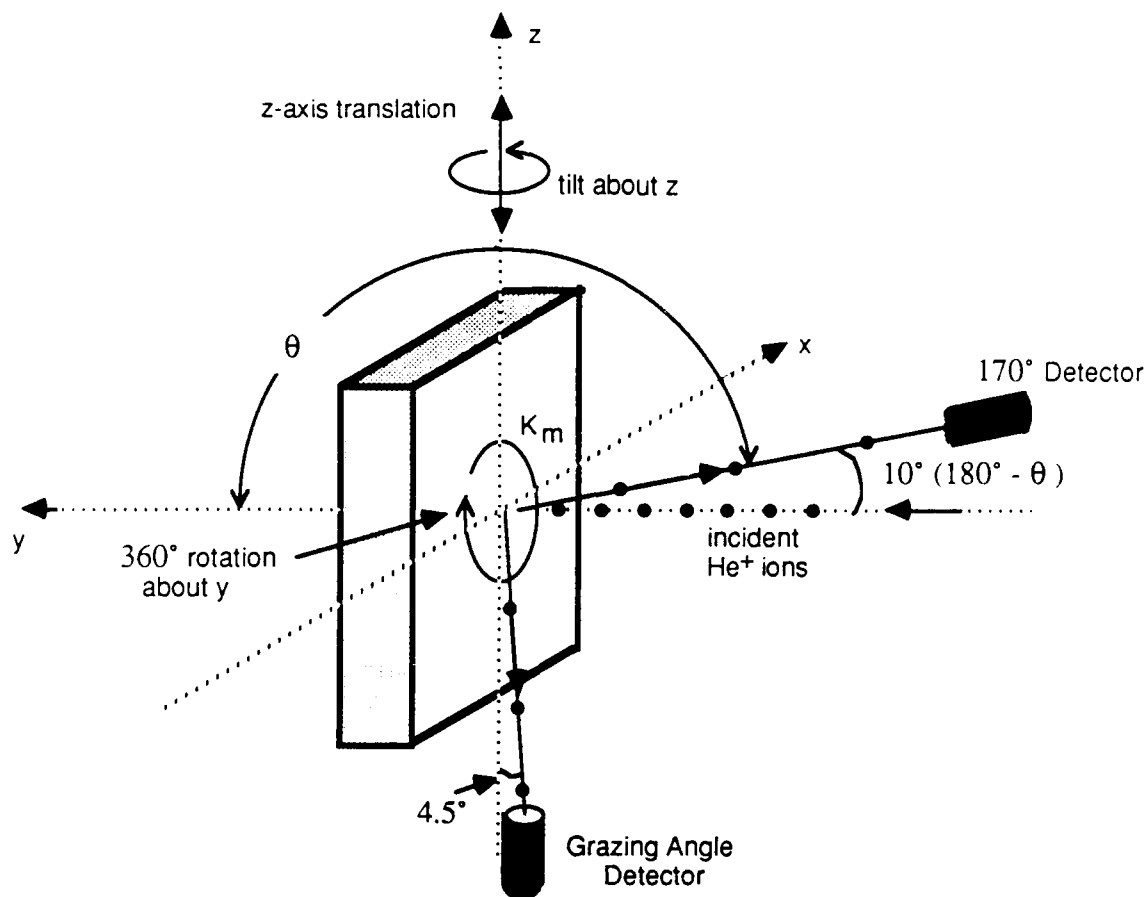
Fig. 2.1 Schematic illustration of the experimental setup used in RBS and channeling experiments. The incident alpha particles scatter off of atoms in the sample and are detected by a detector(s) placed at a known angle(s) from the incident beam. The three degrees of freedom of the goniometer (360° about y, tilt about z, and translation up and down z) allow samples to be analyzed in both the random and axial channeling orientations.

components and the crystal quality in the near surface region of crystalline materials. As such, it is ideal for the study of ion implanted samples. In this technique, a beam of collimated, monoenergetic alpha particles ($^4He^+$ nuclei) with high energy (1-3 MeV) impinge on a target as seen in Fig. 2.1. Some of these particles undergo a close collision with the nucleus of a target atom, radically changing the energy and direction of the ions. Particles scattered by angles > 90° can escape back out of the front surface of the target and be detected. One or more detectors are placed at known angles θ with respect to the incident beam direction and the detected particles are sorted according to their energy using a multi-channel analyzer. This information is then stored in a computer as the number of

$^4He^+$ ions or "counts" versus "channel number" (proportional to the energy). The energy distribution of the backscattered ions gives information about the atomic composition of the sample and the depth distribution of each atomic species. In addition, if the sample is a single crystal with a major crystallographic axis aligned with the beam, the beam will be channeled and information about crystal damage, the location of impurity atoms, and the thickness of amorphous layers can be obtained.
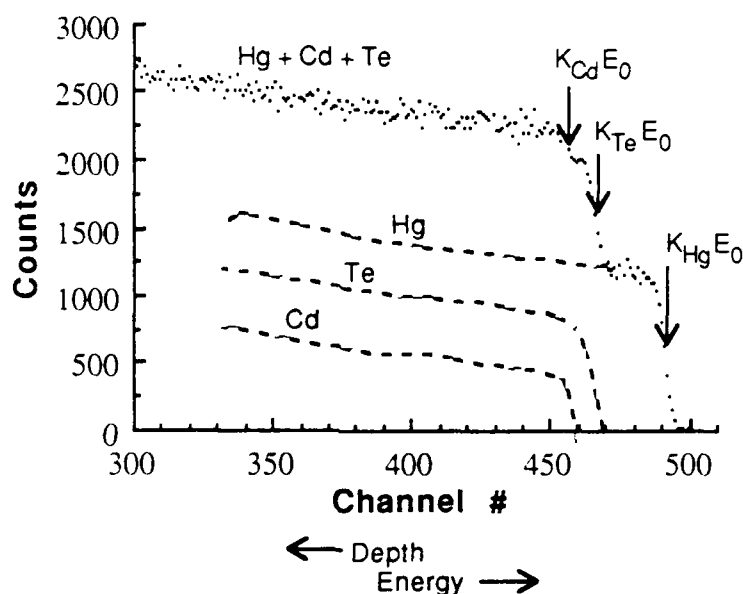
Fig. 2.2 A random MCT spectrum taken with the detector at 170°. The spectrum is composed of the sum of the contributions from Hg, Cd, and Te. The leading edge of each component is determined by $K_{M_2}E_0$ where $M_2 = $ Hg, Cd, or Te and $E_0 = 2.2$ MeV.

Fig. 2.2 shows a random MCT spectrum taken at 2.2 MeV with the detector at 170°. The spectrum is composed of the sum of the contributions from Hg, Cd, and Te. The leading edge of each component is determined by $K_{M_2}E_0$ where $M_2 = $ Hg, Cd, or Te, K_{M_2} is the kinematic factor for each target element, and $E_0 = 2.2$ MeV is the energy of the incident alpha particles. The kinematic factor increases with increasing mass so the Hg edge appears at a higher energy (channel #) than the Te edge which appears at a higher energy than the Cd edge. Note that at this beam energy the large difference between K_{Hg}

and K_{Te} allows a significant portion of the Hg sublattice to be resolved without interference from the other target constituents. The thickness of this region is ≈ 1000 Å, calculated using concepts that are discussed below. The spectrum height is proportional to the atomic fraction and the square of the atomic number of each atomic species. A more detailed explanation of these concepts is given in §2.3.2.B.

2.3.2.A Stanford RBS System

Equipment and typical parameters of the Stanford RBS system are shown in Table 2.1 along with the particular parameters used to study MCT. Dashes in the MCT column indicate parameters that are not changed for MCT. As indicated in the table, a lower beam current is used for MCT than for materials like silicon to avoid sample damage due to the weak mercury bond. This slows data collection, but is partially made up for by the fact that less total charge need be collected because the high mass of its components give a larger backscattered yield than lighter targets.

Table 2.1 PARAMETERS USED IN THE STANFORD RBS SYSTEM

Parameter	Typical Values	Used With MCT
beam ion	$^4He^+, {}^1H^+$	$^4He^+$
beam energy	1.2 - 2.8 MeV	2.2 MeV
beam energy spread	< 3 keV	---
beam collimation	< 0.03°	---
beam current	up to 30 nA	1 - 2 nA
beam area	$\approx 1\ mm^2$	---
collected charge	3 - 36 µC	3.6 µC
chamber vacuum	$\leq 10^{-6}$ Torr	---
detectors	Silicon Schottky barrier	---
detector angle (θ)	170°, 94.5°	---

The sample holder is a precision goniometer with three degrees of freedom: a 360° rotation about the beam; tilt about the z axis; and translation up and down the z axis (see Fig. 2.1). This arrangement allows samples to be analyzed using the random and axial channeling modes, both of which were used in this work. Channeling measurements will be discussed in §2.3.2.C. For a random spectrum, the sample is oriented so that the beam is not aligned with any planar or axial channels, but sees a random arrangement of atoms. The preferred method for obtaining a random spectrum from a single crystal specimen cut close to a low index plane is called a rotational random and involves tilting the sample 6° from the beam to avoid the axial channel and then rotating the crystal through 360° while taking the spectrum.

2.3.2.B Basic Principles

The physical processes that must be understood to interpret an RBS spectrum are those that govern the scattering and stopping of an energetic ion traveling through a target. These include the energy transferred per collision, the likelihood of a collision, the rate at which the incident ion loses energy between collisions, and the statistical nature of the above processes. The same processes are also operative in the lower energy regime used in ion implantation though their effects seem extremely different because of the different energies and incident ion masses involved. Because ion implantation modeling and RBS analysis are both major themes of this thesis, we will introduce the basic concepts here and discuss them in some detail, with the emphasis in this chapter being on the MeV energy range used in RBS. A more detailed discussion of RBS analysis can be found in [2.2].

a) Energy Transferred per Collision

Knowledge of the energy transfer, T, in an ion-target atom collision is what ultimately allows RBS, via the kinematic factor, to sense the mass of the target atom. The importance of T in ion implantation modeling is obvious. We can calculate T in both cases

by considering a classical two-body elastic collision in which a projectile of mass M_1 and energy E_0 strikes a stationary body of mass M_2 which then moves away (assuming T is greater than the binding energy of M_2) with energy E_2 as shown in Fig. 2.3. Applying the principles of conservation of energy and momentum to the problem it can be shown that T for a scattering angle θ in the center-of-mass system is:

$$T = \frac{2E_0 M_1 M_2}{(M_1 + M_2)^2}(1-\cos\theta) \qquad (2.1)$$

T is thus a function of both E_0 and θ as well as the projectile and target atom masses.

Note that the assumption that a collision between two atoms can be modeled by an elastic collision between two isolated particles is valid for a broad range of projectile energies with the lower bound being an energy significantly greater than the binding energy of the atoms in the target ($E_b \approx 10$ eV) and the upper bound being the energy at which nuclear energies and resonances begin to appear (≈ 3 MeV for alpha particles). Since the beam energy used for RBS is 2.2 MeV and typical ion implantation energies are 10 - 300 keV, we are well within these limits.
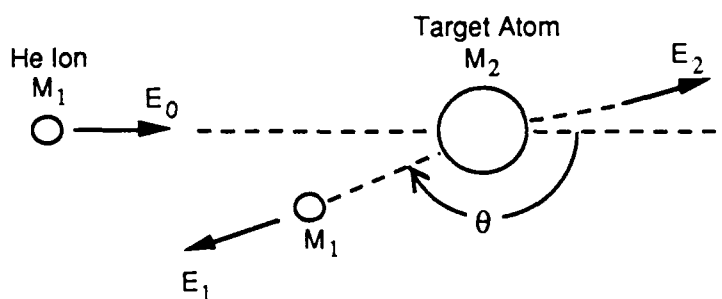
Fig. 2.3 Schematic representation of an elastic collision between an incident alpha particle of mass M_1 and energy E_0 and an (initially stationary) target atom of mass M_2. The energy, T, transferred to M_2 is a function of E_0 and θ as given in (2.1).

For ion implantation T is combined with the scattering cross section (see (c) below and §3.2.2.B) to eventually calculate the stopping power due to ion-target atom collisions

and the vacancy/recoiled atom profiles. In RBS analysis T is used to calculate the kinematic factor, K, which is the ratio between the incident energy of the projectile and the energy of the projectile immediately after a scattering event:

$$K_{M_2} \equiv \frac{E_1}{E_0} = \frac{(E_0 - T)}{E_0} \tag{2.2}$$

$$= 1 - \frac{2M_1M_2}{(M_1 + M_2)^2}(1-\cos\theta) \tag{2.3}$$

K depends only on θ and the projectile and target atom masses. Since the first two are known, we can then calculate the identity of the atom off of which the alpha particle scattered. For a given projectile, K_{M_2} increases with increasing M_2. Values of K_{M_2} for different scattering angles with He^+ as the projectile are tabulated in [2.2].

The maximum in mass resolution is obtained for $\theta = 180°$ since K is most sensitive to differences in target atom mass at this angle. It is obviously geometrically impossible to place a detector at exactly 180° since this would block the incident beam and in practice, detectors are commonly placed at 170° to obtain maximum mass resolution.

b) Energy Loss Rate

Here the treatment differs somewhat between ion implantation and RBS. Ion stopping calculations for RBS consist of one term with contributions from both nuclear and electronic stopping whereas calculations of electronic and nuclear stopping in ion implantation are done separately. Further discussion of ion stopping for ion implantation will be delayed until §3.2.2.

In RBS analysis, the He^+ ions that are not immediately backscattered from the surface atoms of the target penetrate into it and begin to slow down (i.e. lose kinetic energy) due to interactions with the electron cloud of the target atoms and to numerous small-angle collisions with nuclei that lie in the path of the beam. The amount of energy lost per distance traveled is known as the specific energy loss, dE / dx, and is a function of

the projectile and its energy, as well as the target density and composition. Since the energy loss by a particle depends on the areal density of atoms and the thickness traversed, it is usually more convenient to use the stopping cross section, defined as

$$\epsilon \equiv (1/N)(dE/dx) \qquad (2.4)$$

where N is the atomic density of the target. Calculation of the dependence of ϵ on energy and target element is extremely complicated, so semiempirical tables of stopping cross sections have been compiled [2.2]. From these data it is possible to generate a depth scale for a backscattering spectrum.

For compound targets such as MCT, it is assumed that interactions of the projectile with each atomic species are independent so that the stopping cross sections are additive. This is known as Bragg's rule and can be stated

$$\epsilon^{A_m B_n} = m\epsilon^A + n\epsilon^B \qquad (2.5)$$

c) Collision Probability

The probability for a given scattering event to occur between the incident ion and a target atom depends on the differential scattering cross section $d\sigma(E,T)$ of each atom. Any ion entering this area with energy E will be deflected by an angle θ and will emerge with an energy E - T where T is given by equation (2.1). The number of scattering centers per unit area multiplied by the differential scattering cross section $Nt\, d\sigma(E,T)$ gives the probability per unit area for a given scattering event to occur as the ion travels a distance t. In this way, implanted ion distributions can be followed as the ions move through the target. In RBS analysis the scattering cross section relates the number of incident particles Q to the number dQ that are scattered into the solid angle $d\Omega$ and detected. This determines the height of the backscattering spectrum and allows quantitative analysis of atomic composition. The relation for $dQ/d\Omega$ can be written:

$$\frac{dQ}{d\Omega} = QNt \; \frac{d\sigma}{d\Omega} \tag{2.6}$$

In the calculation of scattering cross sections some major differences in treatment between the energy regimes of ion implantation and RBS analysis arise. This is because a model must be chosen to describe the interatomic forces that act between the colliding projectile and target atom and these forces depend on the velocity of the ion. In the energy regime of ion implantation the nuclear charge of the incident ion is partially screened by its remaining electrons, modifying the simple coulombic force between them (this will be discussed in §3.2.2.B), whereas at the high energies used in RBS all of the projectile electrons are stripped away and the collision can be treated as unscreened. The result is that $d\sigma / d\Omega$ for a 2.2 MeV He$^+$ projectile can be written:

$$\frac{d\sigma}{d\Omega} = \left(\frac{Z_1 Z_2 e^2}{4E}\right)^2 \frac{4}{\sin^4\theta} \frac{\left\{\left[1 - \left(\frac{M_1}{M_2}\sin\theta\right)^2\right]^{1/2} + \cos\theta\right\}^2}{\left[1 - \left(\frac{M_1}{M_2}\sin\theta\right)^2\right]^{1/2}} \tag{2.7}$$

Z_1 and Z_2 are the atomic numbers of the projectile and the target atoms, respectively and E is the energy of the He$^+$ ion just before scattering. This is known as the Rutherford cross section. The calculation is much more complicated for the ion velocities used in ion implantation and various numerical approximation schemes have been developed as discussed in Chapter 3.

The fact that the cross section in equation (2.7) is proportional to the square of the atomic number of the target atom means that heavier elements will cause more backscattering and thus give a higher yield than light elements. The cross section is also inversely proportional to the square of the projectile energy so that it is greater for lower scattering energies. This is what causes the upwards slope of backscattering spectra at low energies.

d) Energy Straggling

An ion moving through a target loses energy through many individual interactions with target atoms. Any such process is subject to statistical fluctuations. The result is that particles of identical incident energy will undergo slightly different energy losses ΔE as they travel through a thickness t in a homogeneous medium. In ion implantation this causes a distribution of final ion ranges about some average range (see §3.2.1) and in RBS the effect is to place a limit on depth and mass resolution.

2.3.2.C Channeling

The channeling effect of the regular array of atoms in crystalline solids is widely used as a tool to study their crystal quality and to determine the amount, depth distribution, and annealing kinetics of the disorder produced by ion implantation [2.3]. In a channeling experiment, the sample is carefully oriented so that the ion beam will be aligned along a low index planar or axial direction in the crystal. This leads to a drastic lowering of the backscattered yield from the sample since the rows or planes of atoms steer the ions along the channel with correlated low-angle collisions and they do not approach the lattice atoms closely enough to undergo large-angle elastic scattering events. Note that for perfect crystals, $dE/dx)_{ch}$ (the energy loss with depth in the channeling configuration) is about 30% less than $dE/dx)_R$ and the depth profiles must be corrected accordingly.

Ions can be channeled along both atomic planes and axial directions (intersections of planes). Though planar channeling has special applications in lattice location and defect analysis, in this work planar channels were used only to help orient samples for axial channeling. The detailed alignment procedure is explained in [2.2]. In axial channeling, the sample is oriented such that the beam "sees" only the surface atoms with all the other atoms shadowed by the top layer. The solid line in Fig. 2.4 is sketch of the channeling spectrum expected from a perfect MCT crystal. The random spectrum is included for

comparison. The small peaks on the right (high energy) end of the channeled spectrum are due to the particles that scatter directly off the atoms on the surface of the target and thus appear at the same channel number as the Hg, Cd, and Te edges in the random spectrum. Because of the shadowing by the surface atoms, the yield from deeper within the sample is reduced by around an order of magnitude from the random yield.
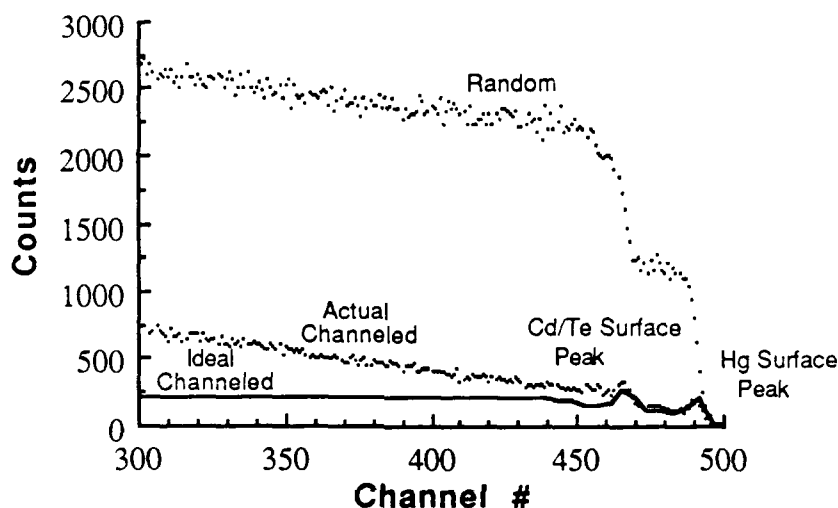
Fig. 2.4 Random and channeling spectra taken with the He beam aligned along the [111] axial channel. "Ideal channeled" is a schematic illustration of the spectrum expected from a perfect crystal at 0 K and "actual channeled" shows an a real spectrum obtained from a sample with a low level of defects at room temperature. The peaks on the right side of the spectra are due to particles scattering directly off of surface atoms.

The above description of channeling applies only to a perfect crystal at 0 K. At higher temperatures thermal vibrations reduce the shadowing effect of the surface atoms so that the beam is gradually dechanneled as it travels through the sample, causing the backscattering yield to increase slightly with increasing depth. Also, defects such as displaced lattice ions, interstitials, dislocations, etc. will cause additional scattering and an increase in the backscattered yield. These effects are illustrated by the dotted line in Fig. 2.4 labeled "actual channeled".

It is possible to extract information on the depth distribution of these structural defects in the near surface region. Just as it does with the atoms at the surface, the He^+ beam backscatters directly off of point defects in the channel such as displaced lattice atoms. If the disordered region is not too thick, this results in a sharp peak in the channeling spectrum at the energy corresponding to the depth of the point defects. For a thicker disordered or amorphous region the portion of the beam that is not actually backscattered will still undergo a sufficient number of forward scattering events to dechannel the beam and increase the aligned yield from the underlying good crystal. In contrast to point defects, extended defects such as dislocations and dislocation loops can be viewed as having a heavily distorted core surrounded by a large strained region. Though a small portion of the He^+ beam does directly scatter off the atoms terminating the extra planes in dislocations, the dominant contribution to the backscattered yield is due to the dechanneling of the ions as they travel through the large strained volume. Extended defects thus do not cause sharp peaks in the backscattering spectrum, but instead result in a gradual increase in the backscattered yield. For low defect levels the slope of the channeling spectrum is proportional to the defect concentration. Studying the dependance of the dechanneling on probe beam energy can give additional information about the identity of structural defects.

2.3.3 Van der Pauw Measurements

Electrical properties of the implanted layers are measured using the van der Pauw technique [2.4]. These measurements directly give the sheet resistivity R_s (Ω/sq) and the sheet Hall coefficient R_H. The sign of R_H indicates the carrier type of the layer, (-) for n-type and (+) for p-type. Assuming one carrier dominates conduction, the sheet carrier concentration is then given by $N_s = \pm \frac{1}{qR_H}$ (cm^{-2}) and the mobility is $\mu = \frac{R_H}{R_s}$ (cm^2 $V^{-1}s^{-1}$).

All measurements are done with the sample immersed in LN_2 because of the small band gap of MCT (0.29 eV @ 300 K for x = 0.3). In measurements at room temperature, thermally generated electrons and holes dominate conduction and make it impossible to detect any extrinsic effects. In addition, since the electron mobility in MCT is two orders of magnitude greater than the hole mobility, p-type samples have a negative Hall coefficient at room temperature. At 77 K the concentration of intrinsic carriers is reduced enough so that the material is extrinsic and the carrier type of the sample can be determined from the sign of the Hall coefficient.

Contact was made to the samples by soldering 99.9985% pure indium from Johnson Matthey [2.5] using a Weller controlled temperature soldering station with a very small tip. Because contact quality sometimes tends to degrade with decreasing temperature, and to double-check this method of making contacts, selected samples were tested for linearity at room temperature and 77 K and found to be ohmic. In addition, the contacts were routinely checked for reversibility at room temperature and 77 K and measurements found not to be reversible within 10% were discarded as invalid. It is unusual for contacts not to be reversible and generally problems only occur on the surface layer of annealed samples or in the transition region between the n-type implanted layer and the p-type substrate during differential Hall measurements.

Note that a single set of Hall data gives only a weighted average of the carrier concentration and mobility in the implanted layer. If the carrier concentration were uniform throughout the implanted layer these values would be the correct active sheet concentration and mobility, but in actuality, both the carrier concentration and the mobility vary as a function of depth. Since the mobility decreases with increasing carrier concentration, the measured N_s will be lower than the real active dose. To measure the real carrier concentration and mobility vs. depth in a material, differential van der Pauw measurements

must be performed. This method consists of alternately performing sheet measurements and stripping off thin layers of material until all of the implanted layer is removed. The mobility and carrier concentration of each individual layer can then be found from [2.6]:

$$\mu_i = \left(\frac{R_{H\,i}}{R_{s\,i}^2} - \frac{R_{H\,i+1}}{R_{s\,i+1}^2} \right) \left(\frac{1}{R_{s\,i}} - \frac{1}{R_{s\,i+1}} \right)^{-1}$$

(2.8)

$$n_i = \left(\frac{1}{R_{s\,i}} - \frac{1}{R_{s\,i+1}} \right) (q d_i \mu_i)^{-1}$$

(2.9)

where $R_{H\,i}$ and $R_{s\,i}$ refer to the sheet Hall coefficient and sheet resistivity measured following the ith layer removal and d_i is the thickness of the layer removed. The total active dose N_d is then

$$N_d = \sum_i n_i\, d_i$$

(2.10)

Sectioning for our differential van der Pauw measurements was done using a calibrated etch and a stop watch. The etching solution was composed of equal parts methanol and glycerine, stirred until the mixture was homogeneous, and 0.6% Br. This mixture decomposes rapidly and must be used within 20 minutes of the addition of the Br – all of our etching was done with an etch less than 10 minutes old. The etch rate for this solution is $\approx$ 0.48 μm/minute [2.7].

2.3.4 Photoluminescence

2.3.4.A Introduction

Optical properties of the as-implanted and annealed layers are explored using photoluminescence, a standard technique for observing defects and impurities in semiconductors. In a photoluminescence experiment, the sample is illuminated with light of energy greater than its band gap, generating excited electron-hole pairs as shown in Fig. 2.5. The photogenerated electrons and holes thermalize to the conduction band minimum

and the valence band maximum and then recombine through several competing mechanisms: the emission of a photon, called photoluminescence; surface recombination; nonradiative recombination through the emission of one or more phonons; or Auger recombination.
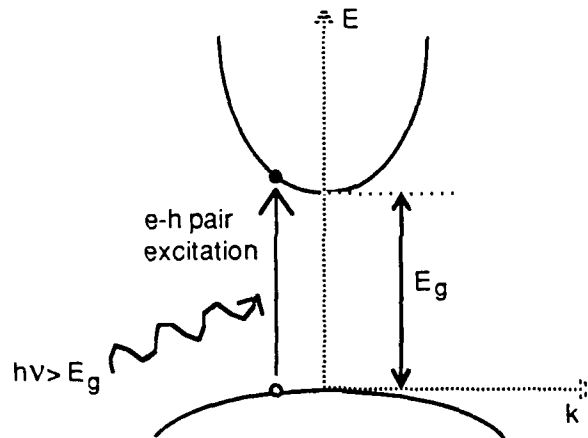
Fig. 2.5 Schematic illustration of the absorption of light with energy greater than the band gap in a direct band gap semiconductor. The subsequent radiative recombination of photogenerated electrons and holes is called photoluminescence.

2.3.4.B Absorption and Luminescence Processes

a) <u>Absorption</u>

Because its small, direct band gap, MCT absorbs very strongly at 2.4 eV, the photon energy of the laser used for the excitation. The absorption coefficient is between 2 x 10^5 cm^{-1} (HgTe) and 2.8 x 10^4 cm^{-1} (CdTe) [2.8], leading to an absorption depth of 1000 - 2000 Å. Since photogenerated carriers will move on the order of a diffusion length (several μm) before recombining, photoluminescence studies bulk properties.

Immediately after being produced, the electrons and holes are quite "hot" with respect to the lattice, but they very quickly thermalize down to the conduction band minimum and the valence band maximum via phonon emission. The time required for this

process is on the order of several nanoseconds and is much shorter than the recombination lifetimes of interest, so it is generally assumed that the photogenerated electrons and holes are in the lowest energy states available to them before recombination occurs.

b) Exciton Recombination

In a sufficiently pure material at low temperature, the lowest energy state of photogenerated electron-hole pairs is an exciton. When a free exciton recombines in a direct bandgap material, it produces a sharp peak of energy just below the bandgap:

$$h\nu = E_g - E_x \qquad (2.11)$$

where E_x is the exciton binding energy. Excitons may also be bound to impurities in which case their emission is a narrow peak of lower photon energy than the free exciton. Exciton formation is less favored in impure materials where local fields tend to break excitons up into free carriers and as the temperature increases beyond where $kT > E_x$. Hence excitonic peaks may not be visible at all in samples with defects and will become less intense as temperature is increased.

c) Band-to-band Transitions

Band-to-band recombination, or free carrier recombination, becomes more important at higher temperatures and in imperfect semiconductors. In a direct bandgap material the emission spectrum is

$$L(\nu) \propto (h\nu - E_g)^{1/2} \qquad (2.12)$$

so that it has a low energy threshold at $h\nu = E_g$. For higher temperatures and excitation rates, states deeper in the conduction and valence bands will become filled, causing emission at higher photon energies. Thus on the low energy side the emission spectrum should rise abruptly at $h\nu = E_g$ and the peak will shift to higher energies as the temperature or excitation rate is increased (neglecting the dependance of the bandgap on temperature). In addition, the density of free electrons, n_e, and free holes, n_h, increases with increasing

excitation rate and the transition probability is proportional to $n_e n_h$, so the peak intensity will increase with increasing pump power. Note that band to band transitions will be the highest energy transitions in a spectrum.

d) Band to Impurity Level Transitions

Examples of band to impurity level transitions are shown in Fig. 2.6. It is possible that the shallow transitions to neutralize ionized donors and acceptors shown to the left in the figure are radiative, but it is unlikely because the phonon emission process has been shown to be more probable [2.9]. In any case, such transitions would be in the far infrared and could not be studied with the apparatus used in this thesis.
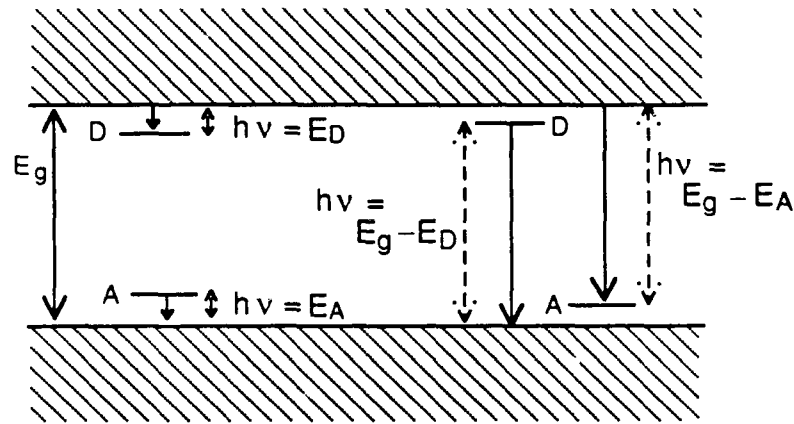
Fig. 2.6 Examples of possible transitions between a band and a defect level. The shallow transitions shown to the left are less probable than the phonon emission process [2.9] and, in any case, would appear at wavelengths too long to be studied in this thesis. Deeper transitions are shown to the right.

Deep transitions involving either the transition of an electron from the conduction band to an acceptor or from a donor to the valence band are shown to the right in Fig. 2.6. In direct bandgap materials these types of transitions will emit a photon of energy:

$$h\nu = E_g - E_D \text{ (or } E_A) \tag{2.13}$$

Since the transition probability is only proportional to n_e or n_h, the peak intensity should increase with increasing pump power, but not as fast as that for band to band transitions.
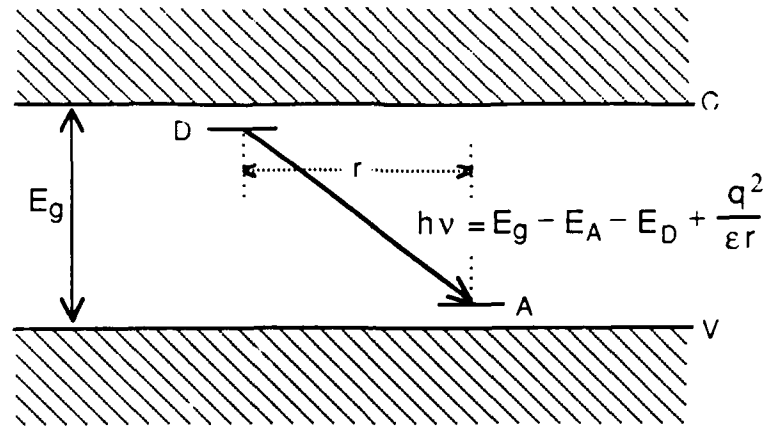
Fig. 2.7 Schematic illustration of a donor-to-acceptor transition. The energy of the final state is lowered by the coulomb interaction between the impurities. Because the strength of this interaction depends on the pair separation, the resulting luminescence peak is fairly broad.

e) Donor-Acceptor Transitions

When both donors and acceptors are present in a material, the coulomb interaction between them lowers their binding energies so that transitions between them result in photons of energy:

$$h\nu = E_g - E_A - E_D + \frac{q^2}{\varepsilon r} \tag{2.14}$$

where r is the donor-acceptor pair separation. Such a transition is illustrated in Fig. 2.7. Because of the variation of r, the resulting emission spectrum will be quite broad, with the lowest photon energy occurring for the most widely separated pairs. The transition probability is proportional to $\exp\left(\frac{-2r}{a}\right)$ where a is the effective Bohr radius of the electron.

Thus as r decreases the recombination rate goes up and the emission intensity at first increases, but as r continues to decrease the number of possible pairings decreases, causing the emission intensity to go through a maximum. The peak of the emission shifts to higher energy as the excitation rate is increased, again because of the variation of transition rate with r. At low pump powers only distant pairs with low transition ra es become saturated, but at higher pump power closer pairs are saturated, resulting in a shift of the emission peak to higher energies.

2.3.4.C Photoluminescence System

The photoluminescence set-up is shown in Fig. 2.8. Above band gap excitation of the MCT is provided by the 514.5 nm line of a Coherent 52 Ar ion laser, mechanically chopped at 2 kHz. The laser beam is focused to a spot size of several hundred μm and incident on the sample at a grazing angle with a typical intensity of 1 - 10 W cm^{-2}. Samples are mounted on a OFHC copper cold finger inside a Janis "SuperTran" Cryostat
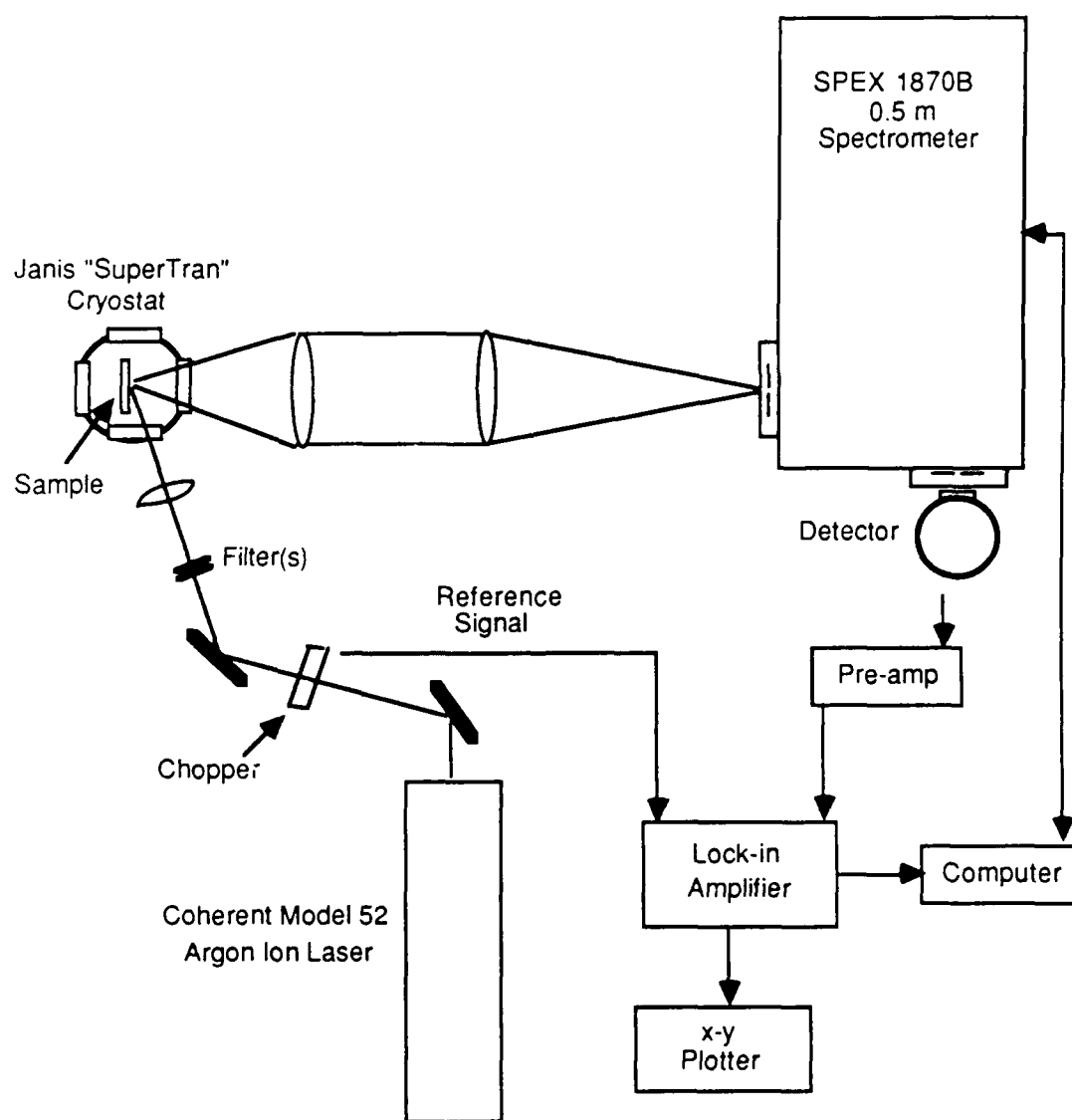
Fig. 2.8 Schematic of the photoluminescence system.

and temperature control is provided by a calibrated rhodium-iron resistance thermometer mounted just above the sample.

MCT's small band gap means that it will luminesce in the mid to far infrared, necessitating the use of special windows that will not absorb that radiation. Thus three of the four windows are made of 2 mm thick CaF_2 which has useful transmission extending from 200 nm to slightly beyond 10 μm. For longer wavelength work, the fourth is KRS-5 (thallium bromoiodide) which transmits from 600 nm to beyond 40 μm.

The light leaving the sample is focused with either CaF_2 or KCl lenses onto the entrance slit of a SPEX 1870B 0.5 m spectrometer. Luminescence is detected with either an Infrared Associates photovoltaic InSb detector for wavelengths up to 5.5 μm, an Infrared Associates photoconductive MCT detector for wavelengths from 4 to 8.5 μm, or a photoconductive MCT detector from Texas Instruments for wavelengths from 9 - 12.5 μm. Signals are processed with a PAR 5207 lock-in amplifier using the reference signal from the SRS mechanical chopper. Both the spectrometer and the lock-in are computer-controlled (HP 9000) so the PL spectra can either be recorded using the x-y plotter or stored in the computer.

2.3.5 SIMS Measurements

Secondary Ion Mass Spectrometry (SIMS) was done on selected samples in order to measure as-implanted ion profiles and ion profiles after the various post-implant annealing steps. All SIMS measurements for this thesis were done at Charles Evans & Associates in Redwood City. Sputtering was done with O_2^+ ion bombardment to measure the boron and indium profiles and Cs^+ ion bombardment to measure the fluorine distributions. For the ^{115}In implants molecular interference from species such as $^{114}Cd^1H$ increase the background level to about 10^{15} cm^{-3}, but this presents no problem because the peak of our indium implants are typically $\geq 5 \times 10^{17}$ cm^{-3}.

The implanted ion concentration is calculated by integrating the area under the curve for ion current and setting it equal to the implanted dose of each sample. The conversion of sputtering time to depth is based on the measurement of the analytical craters using a Tencor stylus profileometer. This procedure is nominally accurate to within 7-10%, but the surface roughness of LPE samples increases the uncertainty in the depth scale somewhat. The shape of the Cs^+ crater makes its depth especially difficult to measure, resulting in additional error in the depth profiles for the fluorine implants.

2.4 Summary

This chapter has described the sample preparation and measurement techniques that were used in this thesis. We discussed the use of RBS and MeV ion channeling in measuring sample composition and the level of implant-induced damage. We also explained the procedures used in making samples for sheet and differential van der Pauw measurements to assess the effects of implantation and post-implant annealing. In addition, the fundamental transitions responsible for photoluminescence spectra were reviewed and we described the experimental setup used to make our low temperature photoluminescence measurements on MCT. Finally we discussed the SIMS measurements made on the samples and commented on the limitations in the accuracy of the depth profiles caused by the roughness of the LPE samples.

2.5 References

[2.1]   T.-M. Kao, Development of Direct Ion Implantation Processes and Characterization Techniques for Mercury Cadmium Telluride Epilayers, Ph.D. Thesis, Stanford University, May 1987.

[2.2]   W.-K. Chu, J.W. Mayer, and M.-A. Nicolet, *Backscattering Spectrometry*, Academic Press, Inc., San Diego, 1978.

[2.3]   L.C. Feldman, J.W. Mayer, and S.T. Picraux, *Materials Analysis by Ion Channeling*, Academic Press, Inc., San Francisco, 1982.

[2.4]   L.J. van der Pauw, Philips Technical Review, **20**(8), 220 (1958/59).

[2.5]   Indium, Wire, 0.5 mm diameter, purity 99.9985%, ÆSAR.

[2.6]   J.W. Mayer, O.J. Marsh, G.A. Shifrin, and R. Baron, Canadian Journal of Physics. **45**, 4073 (1967).

[2.7]   private communication from R.C. Bean

[2.8]   Jacques I. Pankove, *Optical Processes in Semiconductors*, Dover Publications, Inc., New York, 54, 1971.

[2.9]   Jacques I. Pankove, *Optical Processes in Semiconductors*, Dover Publications, Inc., New York, 132, 1971.

Chapter 3

As-Implanted Ion Profiles and Damage:
Calculation and Experiment

3.1 Introduction

Ion implantation is the introduction of atoms into the surface region of a target by bombardment of the substrate with medium energy ions (usually 10 - 400 keV). The most common application is the doping of semiconductors during device fabrication [3.1]. The chief advantages of ion implantation over other doping methods are the ability to independently control the number of implanted dopant atoms (through the dose), the depth of the atoms (through the ion energy), and shape of the implanted atom profile (by implanting at more than one energy). Disadvantages include radiation damage, an inevitable result of bombardment with heavy ions, which is almost always undesirable in semiconductors because of its deleterious effects on the mobility and lifetime of carriers. An additional problem is that the as-implanted ions do not generally come to rest on regular lattice sites and so are not electrically active. A high temperature annealing treatment is necessary to restore the crystal lattice and to move the implanted ions on to electrically-active lattice sites. Care must be exercised at this stage to ensure that the profiles of earlier diffusion steps are not adversely affected.

For implantation to be practically useful it is necessary to be able to predict for any ion-target combination both the profile of the implanted ions and the changes in the target caused by the ions as they travel through (*i.e.* the radiation damage distribution). Knowledge of the latter is useful since the residual damage after an implant can strongly influence the effectiveness of post-implant annealing as well as dopant activation and redistribution during annealing [3.2]. To this end, a succession of theoretical models of the implantation process have been developed, based on the energy interaction mechanisms between the impinging ions and the atoms of the substrate.

Though the above description applies to ion implantation in semiconductors in general, some of the specifics appear different for MCT. In particular the statement that radiation damage is detrimental would seem to be false since, as discussed in Chapter 1, radiation damage remains one of the easier ways of forming an n-type layer on p-type MCT and high quality n-p junctions have been formed without annealing [3.3]. Even so, it is generally accepted that the properties of implanted junctions would be more predictable if a method of defect annealing and electrical activation of implanted ions could be developed for MCT [3.3, 3.4]. Whichever method of junction formation is chosen, it is obvious that a detailed understanding of ion ranges and damage production during implantation is at least as important in MCT as it is in Si and GaAs for device fabrication.

This chapter addresses the effects of implantation of different ions in MCT. The basic terminology of implantation is defined in §3.2. The evolution of models for predicting implant range and damage production is briefly discussed in §3.3 along with a more detailed description of the two implant simulators used to model profiles in this thesis. Ion profile calculations are presented in §3.4 and compared with SIMS measurements. Finally, §3.5 discusses damage calculations and compares them to experimental results from MeV ion channeling and van der Pauw measurements on as-implanted samples. The chapter is summarized in §3.6.

3.2 Ion Implantation Concepts

3.2.1 Ion Profile Definitions

As energetic ions penetrate a material they lose energy through collisions with the electrons and atomic nuclei of the target and eventually stop. The distance that they travel before coming to rest is known as the range, R. In the semiconductor industry, it is actually the projection of this distance along the direction parallel to the incident beam, called the projected range, that is of greater interest because it describes the penetration

depth of the ions. Some ions will experience relatively fewer scattering incidents and travel

deeper into the target and some ions will have relatively more collisions and come to rest

closer to the surface. Because of this statistical nature of the stopping process the projected

range is described by its average value R_p as well as by a standard deviation ΔR_p

(sometimes called straggle) along the direction of the incident ions. These concepts are

illustrated below in Fig. 3.1. One common approximation is to assume that the ion profile

can be described by a Gaussian distribution, in which case the relation between the peak

concentration (cm^{-3}) and the implanted dose (cm^{-2}) is as given in the figure.
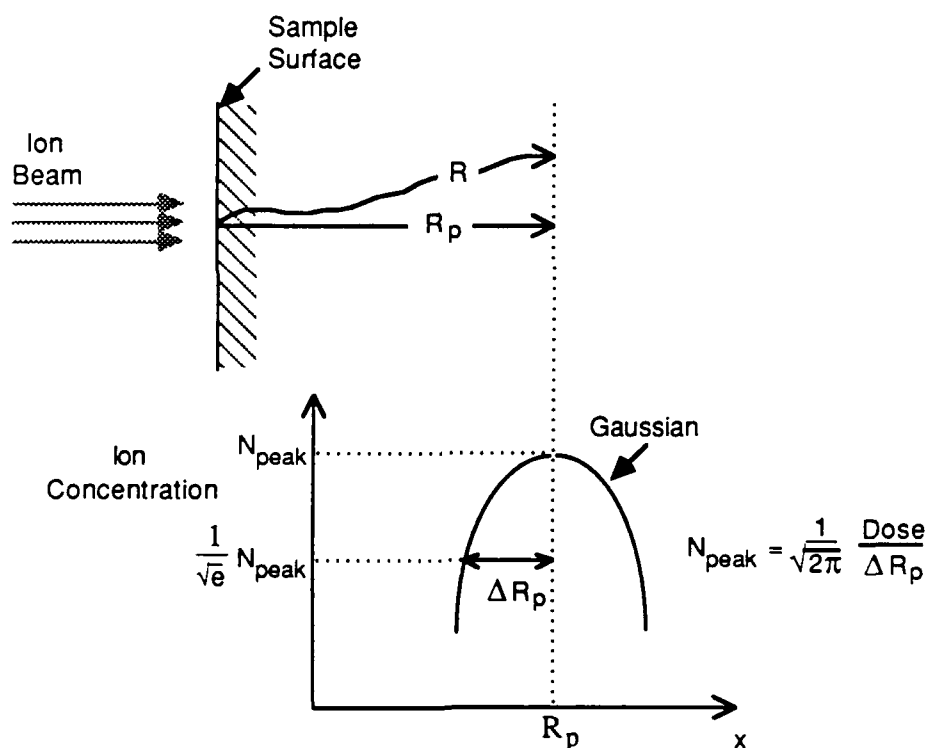
Fig. 3.1 Range and range distributions of implanted ions. The upper portion of the figure shows the definition of the range, R, and the projected range, R_p. The lower portion illustrates the relationship between the ion concentration at R_p and that at ΔR_p for a symmetrical Gaussian distribution. The relation between the implanted dose and the peak concentration for a Gaussian distribution is also given.

3.2.2 Ion Energy Loss Mechanisms

3.2.2.A Basic Description

The energy loss of an ion penetrating a solid is due to two major mechanisms, nuclear stopping and electronic stopping which, to a good approximation, operate independently of each other [3.5]. As discussed in Chapter 2, to interpret RBS spectra it is sufficient to lump both stopping mechanisms into a single term called the stopping cross section, but here we are interested in modeling what happens to the target during an implant, so we must treat each contribution separately.

In nuclear stopping energy is transferred to the target nuclei through elastic collisions characterized by large angle scattering of the incident ions and discrete energy losses. This is the process responsible for producing displaced lattice atoms. Such atoms, referred to as recoils, frequently receive sufficient energy to create recoils themselves and thus cause a cascade of collisions. Electronic stopping is an inelastic process due to interactions of the incident ion with the electrons of the target atoms. The energy losses are assumed to be continuous and there are negligible angular deflections and lattice damage.

3.2.2.B Nuclear Stopping

Consider an ion of atomic number Z_1 passing the nucleus of a target atom with atomic number Z_2 at a distance r. Since the positive charges on both the ion and the target atom are partially screened by their electrons, the simple coulombic force between them is modified by a screening function. The interatomic potential can be written:

$$V(r) = \frac{q^2 Z_1 Z_2}{r} f \left(\frac{r}{a} \right) \tag{3.1}$$

where a is a screening parameter and $f(r/a)$ is the screening function. For very high incident energies all of the electrons are stripped off the incident ion and the collision can be treated as unscreened. This corresponds to Rutherford stopping, discussed in Chapter 2. Knowledge of the form of the potential function allows the scattering cross section for each

type of target atom to be calculated. The energy transfer for each scattering angle is then calculated using conservation of energy and momentum as discussed in Chapter 2 and integrated over the scattering cross section to find the nuclear stopping power S_n (eV cm^2).

Many different forms for the screening function have been proposed over the years. The most successful (judged by popularity) was derived by Lindhard from the Thomas-Fermi model of the atom and is written [3.6]:

$$f\left(\frac{r}{a}\right) = \frac{r/a}{\left((r/a)^2 + 3\right)^{1/2}} \tag{3.2}$$

where a is the screening parameter:

$$a = \frac{0.8853 \, a_0}{\left(Z_1^{2/3} + Z_2^{2/3}\right)^{1/2}} \tag{3.3}$$

a_0 is the Bohr radius, and Z_1 and Z_2 refer to the atomic numbers of the incident and target atoms respectively. This form is still in common use today in the LSS model for ion ranges, an approach developed more than 25 years ago by Lindhard, Scharff, and Schiott. Calculations based on this model show that nuclear stopping increases with ion energy at low energies, reaches a maximum at some intermediate energy, and decreases at still higher ion energies. It is known that this screening function overestimates S_n for large interparticle separations.

The universal interatomic potential, developed by Ziegler, Biersack, and Littmark [3.5], is a more recent form that uses a single analytic function reduced from hundreds of interatomic potentials calculated from Hartree-Fock atoms. This method yields the same qualitative form for nuclear stopping as the LSS calculations and is more accurate, having a standard deviation of only 5% when compared with experiment.

3.2.2.C Electronic Stopping

The calculation of energy loss due to electronic stopping is a highly complex problem. particularly for heavy ions ($Z_1 > 2$), and the accuracy of current stopping tables decreases with decreasing ion energy [3.7]. Electronic stopping is well understood for high energy light ions where we can assume a direct ion-electron energy transfer in a Coulomb interaction field. The stopping for heavy ions in the Bethe-Bloch regime ($E > 10$ MeV) scales with light ion stopping powers because at these velocities the heavy ions are completely stripped of electrons. This leads to tables with accuracy better than 5% at high energies [3.7]. At lower energies the scaling laws begin to break down because the incident ion is not fully stripped of its electrons, but recently a model based on the ideas of Kreussler, Varelas and Brandt [3.8] and Brandt and Kitagawa [3.9] has extended the ability to predict electronic stopping values with reasonable accuracy down to ion energies > 30 keV/amu. This was done by calculating the effective charge of the heavy ion not by comparing the ion's electron velocities to the ion velocity as done previously, but by comparing them to the Fermi velocity of the target. Implantation energies are generally $<$ 25 keV/amu and at these low velocities the ion's outer electrons will not be stripped away. The complex interactions between the ion's electrons and the target electrons mean that pure theory is only accurate to within a factor of two. This accuracy has been improved by Ziegler, Biersack, and Littmark to about 10% for a universal low-energy electronic stopping calculation using a judicious combination of theory and empirical results.

Both experiment and theory show that S_e for low velocity heavy ions is velocity proportional (*i.e.* proportional to the root of energy, $S_e = kE^{1/2}$), with some important exceptions. Stopping is anomalously low for the semiconductors Si and Ge. It is suggested that this is due to the presence of a bandgap since there are fewer low-energy excitation levels available than in a free electron gas. Experimental evidence suggests that S_e goes as $v^{0.7}$ in such narrow band-gap materials for ions with $Z_1 < 19$ [3.5], but little

data exist for heavier ions in these materials. It would seem reasonable to expect a similar effect in MCT since it is also semiconductor.

Another question concerns the proportionality constant, k. Experiments have revealed a periodic dependence of this parameter on the atomic number of the ion. The LSS expression for k is still the most commonly used, but it monotonically increases with energy because it is based on statistical atoms with smoothed charge distributions. It is also empirically inaccurate by factors of 2 or more. Recent theories treating the atoms in terms of their more precise radial electron density wave functions have led to qualitative agreement with experimental data, but the LSS formulation is considered adequate as a first order approximation.

3.2.2.D Total Energy Loss

Though it is not as accurate as some of the newer models of energy loss, the LSS model is still the most widely used and gives a qualitative understanding of the partitioning of nuclear versus electronic stopping for different ion-target combinations. The calculations involve a system of dimensionless range and energy parameters [3.10]:

$$\rho = R\pi a^2 N \frac{M_1 M_2}{(M_1 + M_2)^2} \tag{3.4}$$

and

$$\varepsilon = E \frac{a}{e^2} \frac{M_2}{Z_1 Z_2 (M_1 + M_2)} \tag{3.5}$$

a is the screening parameter defined in equation (3.3), N is the number of atoms per unit volume, and M is the atomic mass of the ion and target atoms. When calculated in terms of the above dimensionless parameters, energy loss due to nuclear stopping versus $\varepsilon^{1/2}$ is independent of ion-target pair, yielding the universal curve shown in Fig. 3.2. A value of ε ≈ 0.35 corresponds to the energy at which nuclear stopping has a maximum (ε_m in the
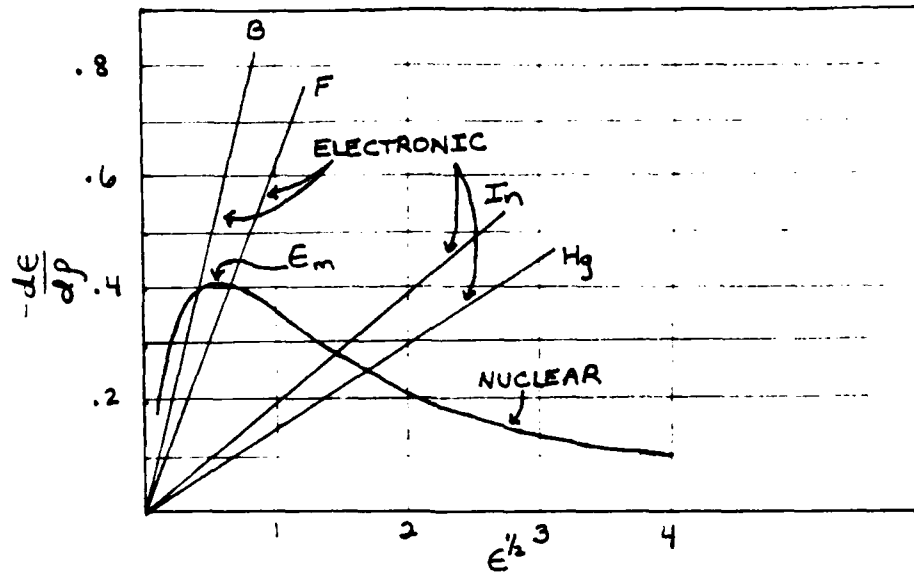
Fig. 3.2 LSS values for nuclear and electronic stopping in MCT (x = 0.3), expressed in terms of the reduced variables ε and ρ. (adapted from [3.10]) A single universal curve is obtained for nuclear stopping while a family of lines is obtained for electronic stopping, depending on the mass of the ion. Electronic stopping curves for several different ions implanted into MCT are included. Values of k_{LSS} and the characteristic energies ε_m and E_c are given in Table 3.1.

figure) and for $\varepsilon > 5.0$, the nuclear scattering is well approximated by unscreened Rutherford scattering.

For electronic stopping the LSS value for the proportionality constant k_{LSS} is

$$k_{LSS} = Z_1^{1/6} 0.0793 \left[\frac{Z_1 Z_2 (M_1 + M_2)^3}{(Z_1^{2/3} + Z_2^{2/3})^{3/2} M_1^3 M_2} \right]^{1/2} \qquad (3.6)$$

Thus energy loss due to electronic stopping depends on the ion-target combination and yields a family of curves when plotted versus dimensionless energy as shown in Fig. 3.2. The energy at which the universal curve for nuclear energy loss crosses the electronic energy loss curve is known as the critical energy, E_c. For implant energies greater than E_c electronic stopping is the dominant energy loss mechanism and for energies smaller than E_c nuclear stopping dominates. As can be seen in Fig. 3.2, E_c is higher for heavier ions

which means that heavy ions lose a greater fraction of their energy to nuclear stopping than do light ions. Table 3.1 shows ε_m, E_c and k_{LSS} for several different ions implanted into MCT.

Table 3.1 ε_m, E_c AND k_{LSS} FOR DIFFERENT IONS IMPLANTED INTO MCT

Ion	ε_m (keV)	E_c (keV)	k_{LSS} (unitless)
B	14	10	0.94
F	28	34	0.62
In	300	1750	0.19
Hg	700	5900	0.15

3.2.3 Damage

Because large energy transfers occur only for nuclear stopping, it is this process, and not electronic stopping, that is considered to be responsible for radiation damage in the target. These energy transfers can range from fractions of an eV to tens of keV whereas the energy necessary to knock a target atom off of its lattice site, known as the displacement energy, E_d, is only about 25 eV for almost all materials [3.11]. This means that many atoms are displaced from their lattice sites, usually with enough kinetic energy to create recoils themselves. The result is a collision cascade consisting of many displaced atoms. These displaced atoms may remain as an accumulation of vacancies and interstitial atoms or they may coalesce into more complex defects such as clusters, dislocations, or dislocation loops, depending upon the nature of the target and experimental parameters such as the implantation temperature and the density of the collision cascade.

The damage track left by a light ion differs qualitatively from that left by a heavy ion. Light ions generally have energy well above E_c and thus they lose energy primarily to

electronic processes near the surface. As they travel into the target and lose energy, nuclear stopping becomes dominant and the ions displace lattice atoms, resulting in a damage layer deeper in the target. Recoiled atoms receive a fairly small amount of energy and do not travel far. Heavier ions, however, are likely to have an energy below E_c so nuclear stopping dominates near the surface. Large numbers of recoils are created which carry deposited energy deeper in the sample and cause a dense collision cascade.

3.3 Models for Implantation Profiles

3.3.1 Early Methods

Early implant models used LSS theory to calculate the moments of the total path length and first two moments of the projected range, R_p and ΔR_p, assuming that the distribution could be described by a symmetrical Gaussian about those moments. Though this approximation is generally good near the peak of the distribution, experimental profiles show considerable skewness for concentration levels a factor of 10 or more below the peak value. In addition, even when misaligned to the ion beam by the typical 6° tilt, single crystals will always exhibit some slight amount of channeling deep in the sample because the critical angle for channeling increases with decreasing ion energy. To account for the skewness and channeling tails, the theory was extended to give an arbitrary number of moments of the projected path.

A three-moment approach demonstrated by Gibbons and Mylroie [3.12] uses two half-Gaussians with straggle ΔR_{p1} and ΔR_{p2} joined at their modal range R_M and accurately fits moderately asymmetrical profiles. For extremely asymmetrical profiles, four moments (R_p, ΔR_p, skewness γ_1, and kurtosis β) are calculated and the ion profile is fit with either the Edgeworth or Pearson type distributions.

A basic assumption of LSS theory is that the target is homogeneous and infinite in extent. This renders the theory and the above models, all based on LSS-type calculations,

invalid for predicting implantation ranges in multilayer targets. In response to this problem, more sophisticated models have been developed in which the predicted distribution is calculated directly rather than inferred from moments and an assumed distribution. An additional advantage of these methods is that they can provide distributions of recoil atoms and deposited energy, thus giving an indication of the damage caused by the implant. The first of these methods to be described is a numerical solution of the Boltzmann transport equation and the other is a Monte Carlo solution. Both of these methods were used extensively in this thesis and will thus be discussed in more detail below.

3.3.2 Boltzmann Transport Equation Method

Implant calculations for this thesis using the Boltzmann transport equation method (BTE) were done with the BDIFF program developed by Christel, Giles, and Gibbons [3.13, 3.14] at Stanford University. This method provides a comprehensive treatment of the general ion implantation problem. All targets are assumed amorphous or aligned in a random direction and ions are assumed to be stopped by two independent mechanisms, electronic and nuclear stopping as described in §3.2.2. For quick calculation, nuclear stopping is usually modeled using an early form of the universal interatomic potential called the Magic Formula, based on the Moliere potential. Occasionally LSS calculations are used instead. LSS calculations of electronic stopping were found to be completely inadequate for light ions when ion range predictions were compared with SIMS data, so empirical values were determined as will be discussed in §3.4.1.C.

The BTE for an ion moving through the target is:

$$\frac{\partial F(p)}{\partial z} = N \int \left(\frac{F(p')d\sigma(p' \rightarrow p)}{\cos \theta_{p'}} - \frac{F(p)d\sigma(p \rightarrow p')}{\cos \theta_p} \right) + Q(p) \qquad (3.7)$$

F is the time-integrated momentum distribution as a function of depth z, normal to the target surface. N is the number density of each kind of atom in the target so that the right side of the equation contains a term for each species of target atom. The total differential scattering cross section, $d\sigma(p{\rightarrow}p')$, represents a differential area presented to an incident ion by each target atom. The cosine terms appear because a particle moving at an angle θ to the z axis travels a distance $dz / \cos\theta$ as the entire distribution moves a distance dz. The quantity Q is a generation term which accounts for recoils by allowing particles to be created from rest.

The transport equation is numerically integrated stepwise along z, determining the momentum distribution at all depths. Concentration profiles are computed by assuming that all particles with energy less than some cutoff value are stopped. Recoil particles are generated by nuclear collisions and have their own distributions which are followed in the same way.

This stepwise approach assumes that ions are always moving further into the target, but if an ion or a recoil is scattered by more than 90° it will be moving back towards the target surface where the profile has already been calculated. The probability for such events is high for light ions moving in heavy targets, so a multiple pass approach has been developed to account for them. The energy angle distribution of the backscattered ions or recoils is saved for each step into the target and their motion towards the surface is followed by making a second pass, integrating the transport equation again, this time from deep inside the target to the surface. Further passes can be made to follow recoils or ions backscattered multiple times until all movement has stopped.

Implantation damage is modeled both by recoil and energy deposition distributions. BTE calculations give the number of recoils that stop in each step and the number of vacancies generated as target atoms are knocked out of the lattice. Two cases can then be considered. In case 1, we assume that none of the interstitials are reincorporated into the

lattice and no vacancies are annihilated so that the recoiled atom and vacancy distributions most closely approximate cold implants where little dynamic annealing occurs and damage is "frozen" in. The opposite extreme is to try and take dynamic annealing into account by assuming that stopped interstitials and vacancies annihilate each other whenever possible. This is also how the stoichiometry imbalance that results from an implant into a compound target is computed, as described below.

To find the stoichiometry imbalance, first the net concentration of each kind of target atom in each step is calculated by subtracting the number of vacancies created in each step from the number of recoils that stopped in that step. This results in a profile that has a net concentration of vacancies in the near surface region and a net interstitial concentration deeper in the target. The region dominated by vacancies will be larger for a light recoiled atom than for a heavy one because the heavier recoils will not move as far. The stoichiometry imbalance is then calculated by comparing the net concentration profiles of the different kinds of target atoms. This comparison is simpler for a binary compound than for a ternary since the net concentration of atom A can simply be subtracted from the net concentration of atom B to get the excess concentration profiles. For a ternary compound the relative ratios of each atom must be taken into account to see where the excesses and deficiencies of each type of atom appear. Ion implants into MCT result in a slight excess of mercury near the surface and a corresponding excess of cadmium and tellurium slightly deeper in the target.

Another form of damage is due to deposited energy from low-energy-transfer nuclear events and is calculated in units of eV cm-1 ion-1. If T, the energy transferred in a nuclear event, is less than the displacement energy then this energy is considered to contribute to local damage in the form of phonons or partial displacements. Higher energy events create recoils with an energy $T - E_d$, some of which is gradually dissipated in

electronic stopping and the creation of additional recoils. The remaining energy appears as local damage only when the recoils are later involved in low-energy-transfer events.

3.3.3 Monte Carlo Method

The other implant simulator used in this thesis is a Monte Carlo type program called TRIM developed by J. P. Biersack [3.15, 3.16]. In this program, range profiles are obtained by following a large number of individual ion histories in a target, each history beginning with known initial conditions of energy, position, and direction. Particles are assumed to move in straight paths between binary nuclear collisions which change the direction of motion. Energy loss is due to independent nuclear and electronic processes and an ion is terminated either when its energy drops below a certain cutoff value or it exits from the front or rear of the sample. Nuclear stopping in the most recent version of TRIM is modeled on the universal interatomic potential as discussed in §3.2.2.B, and is an improvement over that used in the BTE calculations above. The analytical scheme it uses reproduces scattering integral results within better than two percent [3.16]. Electronic stopping is considered to be velocity proportional and is calculated using the ZBL formulation discussed in §3.2.2.C. Though Monte Carlo calculations are capable of taking the directional properties of a crystalline lattice into account, such calculations are extremely time consuming, so TRIM assumes an amorphous target.

The program gives information on the ion profile, total damage due to nuclear events, energy deposited in electronic stopping due to the primary ion, energy deposited in electronic stopping due to recoils, and vacancies and interstitials of each component of the target. Profiles are generated by plotting histograms of the number of ions stopped, target atom vacancies created, etc., within each depth interval. As with the BTE calculations, the final vacancy and interstitial distributions are given as if they are frozen in, with no attempt made to model dynamic annealing.

3.4 Ion Profile Calculations and Comparison with Experiment

3.4.1 Ion Ranges

3.4.1.A Energy Dependence

An early goal of this work was simply to calculate ion ranges in MCT and compare the results to experimental data when it was available. To this end, ion ranges and straggling as a function of ion energy were computed for ^{4}He, ^{9}Be, ^{11}B, ^{19}F, ^{20}Ne, ^{27}Al, ^{35}Cl, ^{114}Cd, ^{115}In, ^{127}I, and ^{130}Te using the BTE method and/or TRIM. All calculations were done for $Hg_{0.7}Cd_{0.3}Te$ ($\rho = 7.408$ g / cm^3) unless otherwise noted. Selected results of these calculations are shown in Fig. 3.3a for light elements and 3b for heavier elements and complete statistics are included in the Appendix. We see that the agreement between calculation and the small amount of experimental data that we found is quite good for R_p, though ΔR_p is often overestimated.

3.4.1.B Mass Dependence

Following Wilson [3.17], we plotted the calculated values of projected range vs. ion mass for different energies and obtained the simple curves shown in Fig. 3.4. Expressions can be developed from these curves to give the range for all ions in MCT at each energy by fitting the data to the expression $R_p = cM_2^{-n}$, where M_2 is the ion mass and R_p is in microns. The calculated values for each energy are given in Table 3.2.

Table 3.2 PARAMETERS FOR RANGE VS. ION MASS EXPRESSION

Energy (keV)	c (μm)	n
100	1.311	0.758
200	2.20	0.744
300	3.68	0.787
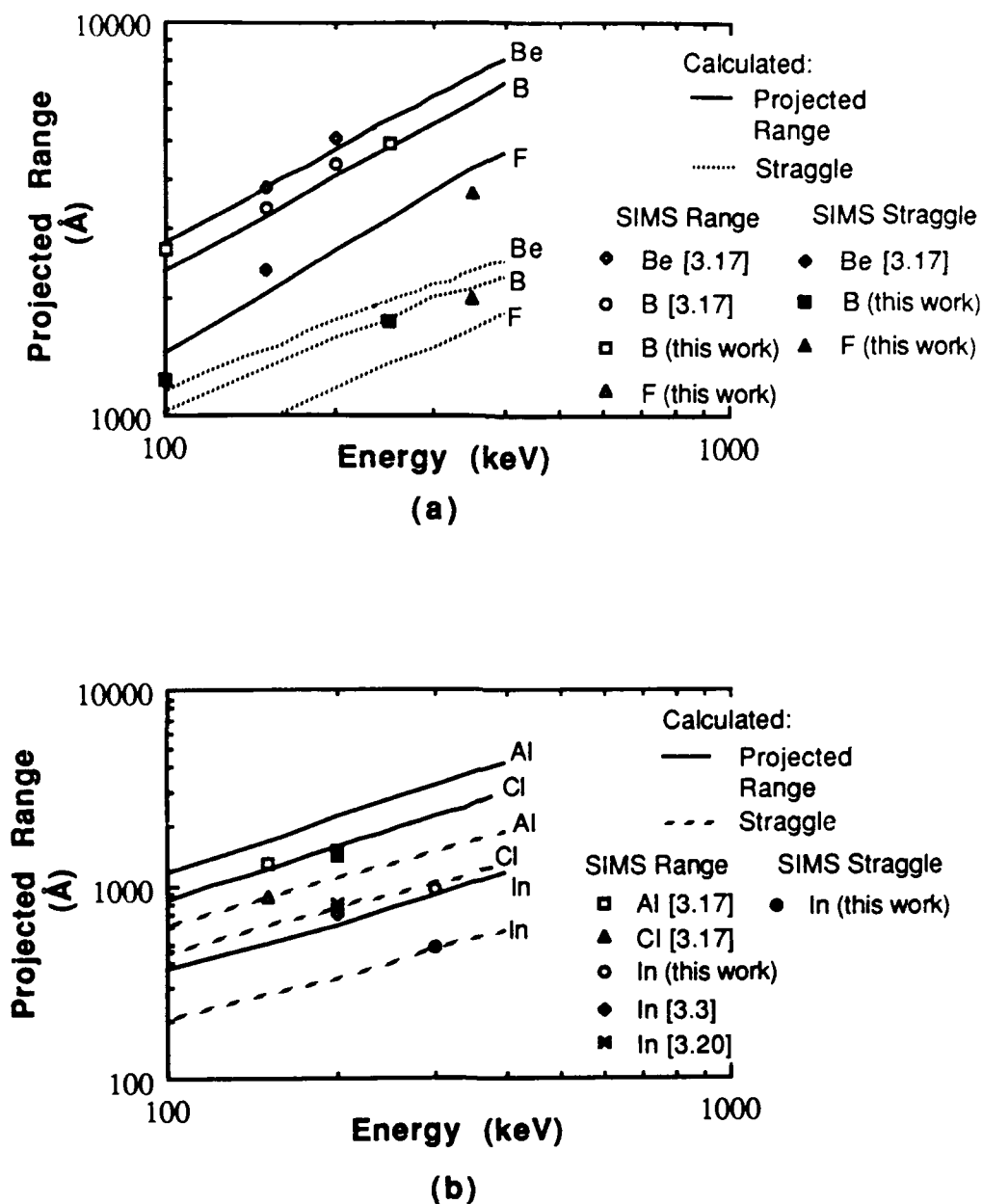
Fig. 3.3 Calculated and empirical range and range straggle for (a) light ions and (b) heavy ions implanted into MCT (x = 0.3). The solid lines are ranges calculated using either TRIM or the BTE method, the dashed or dotted lines are calculated straggle, and the points are from SIMS data either taken for this work or found in the literature. Agreement between calculation and experiment is good for a large regime of ion mass-energy combinations.
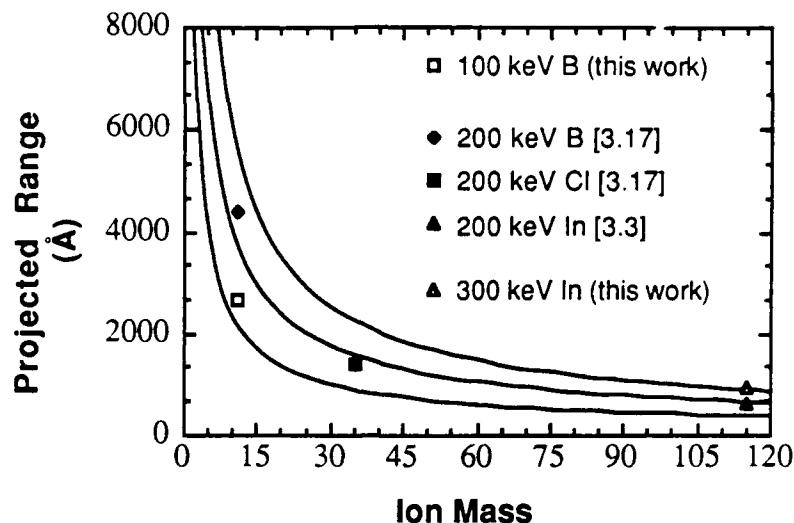
Fig. 3.4 Projected range vs. ion mass for 100, 200, and 300 keV ions implanted into MCT (x = 0.3). The solid lines are calculated from the expression given in the text using the parameters c and n in Table 3.2. The points are from SIMS data either taken for this work or found in the literature.

3.4.1.C Empirical Electronic Stopping

All initial calculations were done using the BTE method with LSS electronic stopping. Though the calculated R_p's for heavy elements were close to experiment, the results for light elements were significantly deeper than SIMS data indicate. This is shown in Fig. 3.5 which compares SIMS data from several sources to calculations of the projected range as a function of energy for a light ion, B, and for In, an ion of about the same mass as the target atoms. The solid lines are from TRIM calculations, the dotted lines are from BTE calculations using LSS electronic stopping, and the dashed lines are from BTE calculations using empirical electronic stopping. Though using LSS values for electronic stopping for BTE calculations accurately predicts In ranges, the B ranges are clearly too deep when compared to SIMS data. The reason for this can be seen by referring to Fig. 3.2. The critical energy for boron implanted into MCT is about 10 keV so that electronic stopping dominates for all our calculations and, as discussed in §3.2.2.C, theoretical LSS electronic stopping can be inaccurate by a factor of 2. Since we did not have the TRIM code at the time and we needed to get accurate calculations with the BTE method, we
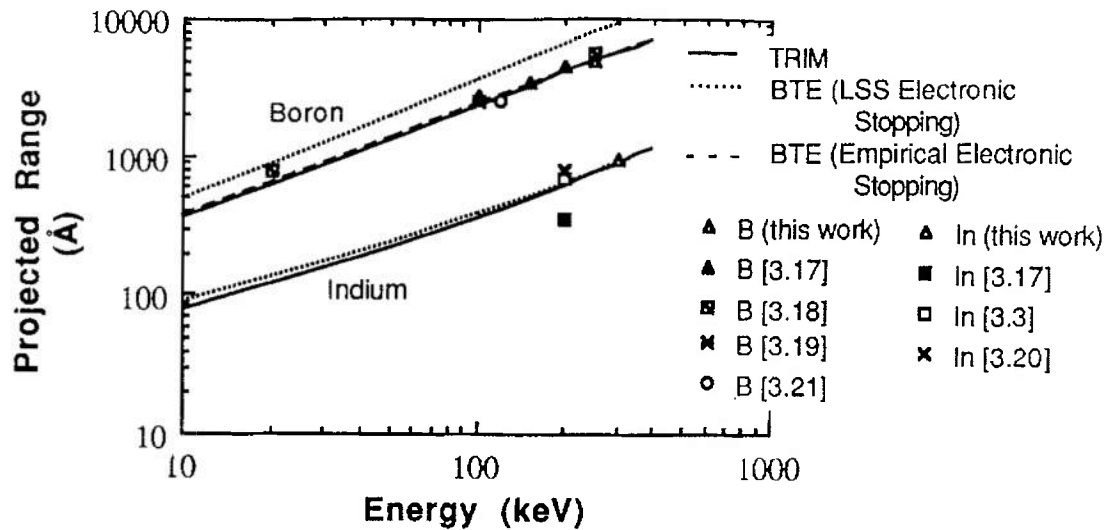
Fig. 3.5 Illustration of the inadequacy of LSS electronic stopping for the calculation of light-ion ranges in MCT. The solid lines are from TRIM, the dotted lines are from BTE calculations using LSS electronic stopping, and the dashed lines are from BTE calculations with empirical electronic stopping. The points are from SIMS data taken for this work or found in the literature. The BTE calculations for boron using LSS electronic stopping are significantly deeper than the SIMS data, while TRIM is in good agreement with the SIMS measurements.

extracted an empirical value for electronic stopping by fitting calculated profiles to SIMS results for two different implant energies (100 and 250 keV). We retained the basic form of the LSS expression, $S_e = k_{LSS}E^{1/2}$, but varied k and p from their theoretical values. For the case of ^{11}B implanted into $Hg_{0.7}Cd_{0.3}Te$ the best fit was found for $k = 2.20 \, k_{LSS}$ and $p = 0.48$. This yields the dashed line in Fig. 3.5 which agrees quite well with SIMS data and the TRIM calculations that we did later. TRIM calculations do not need empirical corrections because they use a more accurate approximation for electronic stopping as discussed in §3.2.2.C. Because of the lack of experimental data on the ranges of different ions in MCT, we could not extract empirical electronic stopping values for most light ions so that all of the calculations for light ions (except B) were done using TRIM. For heavy ions nuclear stopping is dominant, so the inaccuracies introduced by using LSS electronic stopping in BTE calculations are less important and, as shown in Fig. 3.5, the results approach those for TRIM calculations. In fact, it is best to use the BTE method for heavy

ions since the following the individual histories of the many recoils created makes TRIM calculations quite slow. On the other hand, for light ions TRIM is the faster of the two methods because light ions penetrate deep into the sample and the BTE method integrates the momentum distributions along z.

3.4.2 Ion Profiles

SIMS profiles of a 250 keV boron implant and a 300 keV indium implant are shown in Figs. 3.6a and 3.6b along with profiles calculated using TRIM and the BTE. In the light ion case, TRIM fits the data quite well, but the BTE method underestimates ΔR_p and shows a greater skew away from the surface than the SIMS profile. Both TRIM and the BTE method fit SIMS data in the heavy ion case. The problem in Fig. 3.6a does not stem from the form of the electronic stopping since we are already using empirical values in the BTE calculations, rather it is caused by inaccuracies in the nuclear scattering cross sections. As we stated earlier, the form of the nuclear stopping in the BTE method is based on the Moliere potential while that used in TRIM is slightly more sophisticated. The approximations made in calculating the nuclear scattering cross sections for the BTE method are less accurate for wide angle collisions and many such collisions occur when boron is implanted into MCT – almost 75% of the boron ions are scattered by more than 90° for this particular case. Thus though it is clearly possible to get reasonable values for light ion ranges using the BTE, TRIM should be used if accurate light ion profiles are desired. Since only a few incident ions are backscattered for heavy ion implants, the BTE method can still accurately calculate heavy ion profiles.

The SIMS profile extends deeper into the target in both cases because of channeling in the single crystal material. A certain amount of channeling is unavoidable because statistically some ions will gradually be steered into open crystal directions. These ions undergo fewer collisions with the target ions and therefore travel farther, resulting in a channeling tail. Channeling tails can often be fit to an exponential function of position
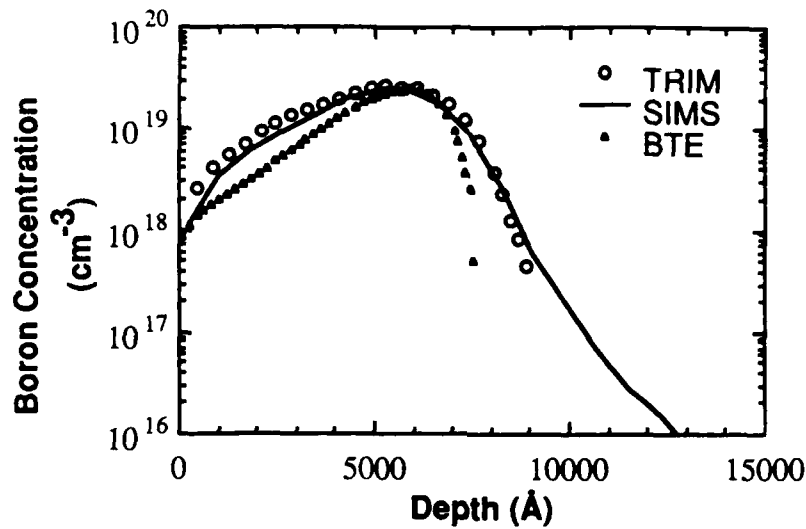
Fig. 3.6 (a) Comparison of a boron profile calculated using the BTE method and TRIM with SIMS data. Implant conditions: T = 77 K, dose = 10^{14} cm^{-2}, energy = 250 keV. The solid line is from the SIMS data, the open circles are from TRIM, and the closed triangles are from BTE calculations (empirical electronic stopping: k = 2.20k$_{LSS}$, p = 0.48). Though TRIM fits the SIMS data well, because of the scheme the BTE method uses to calculate nuclear stopping the BTE calculation significantly underestimates the straggle.
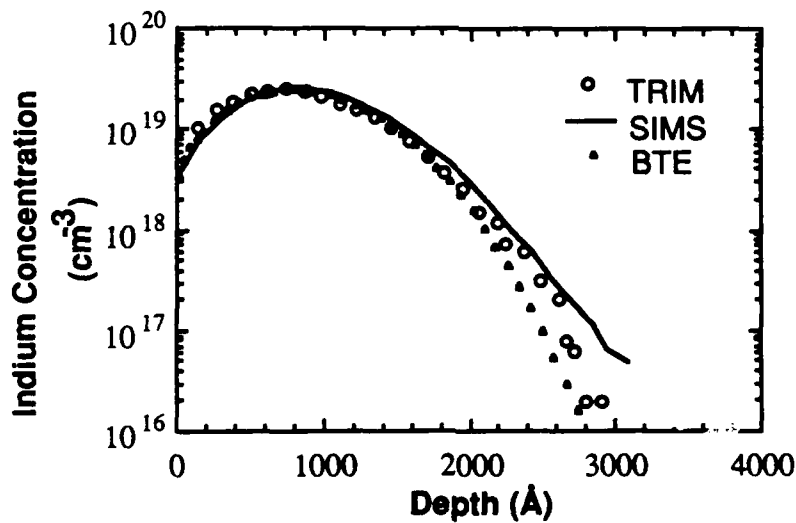
Fig. 3.6 (b) Comparison of an indium profile calculated using the BTE method and TRIM with SIMS data. Implant conditions: T = 77 K, dose = 3 x 10^{14} cm^{-2}, energy = 300 keV. The solid line is from the SIMS data, the open circles are from TRIM, and the closed triangles are from BTE calculations (using LSS electronic stopping). Both calculations fit the SIMS measurement very well.

[3.1], but since both the BTE and TRIM assume an amorphous target they cannot model this effect.

The opposite asymmetry or skewness (γ) of the boron implant when compared to the indium implant is due to the different ratios between the masses of the implanted ions and the average target atom mass. When light ions collide with heavier atoms, there is a large probability that they will be scattered by more than 90° and move back toward the surface. A greater number will then stop in the region between the surface and R_p, resulting in the profile being "filled in" near the surface and decreasing steeply for depths greater than R_p. This is termed a negatively skewed profile. For the same mass target atom, heavier ions tend to be scattered by smaller angles and more come to rest deeper than R_p, making the concentration higher deeper in the target and resulting in a positively skewed profile.

Upon closer examination of the data in the Appendix, it will be noted that for a given mass ion, γ always decreases as the implant energy increases. In fact, for all of the lowest energy implants γ is positive – even for the lightest ions which, according to the discussion above, should have $\gamma < 0$. Rather than being the result of some complicated ion-target atom interaction, this is merely due to the close proximity of R_p and the surface of the sample. More than 25% of the ions in a 10 keV B implant and 5.4 % for 10 keV In implant are backscattered right out of the target. If this part of the profile were not "cut off" by the surface, most of these ions would eventually come to rest between R_p and the surface and the skewness would be more negative. For a given ion, as R_p increases fewer ions are backscattered out the the target and γ decreases.

3.5 Damage Calculations and Comparison with Experiment

3.5.1 Discussion

Implantation damage can be modeled in several different ways as discussed above in the sections describing TRIM and the BTE. These include the profile of energy lost to nuclear events or vacancy and interstitial (stopped recoil atoms) profiles. Some caution should be exercised, however, in directly comparing these calculations with experimental results as these calculations only depict damage as it is created – as if each vacancy and stopped recoil were frozen in position. Of course at typical ion implantation temperatures (*i.e.* room temperature) considerable dynamic annealing is going on during the implant, the extent of which depends on the target. The vacancy and interstitial concentration will be reduced and vacancy-impurity complexes and dislocations may be formed. Even when implants are done at low temperatures where the damage is often considered "frozen in" during the implant, some annealing may occur during an implant and more occurs as the samples are brought back up to room temperature. Nonetheless, implant damage models give at least a qualitative idea of the damage distribution, and can be quantitative under conditions where the damage is stable. BTE calculations, for instance, have been shown to be a reliable indicator of the amorphization depth in silicon for implantations at both 77 K and room temperature [3.13]. Calculations of vacancy and interstitial profiles can also be of use in explaining dopant redistribution during post-implant annealing.

3.5.2 Calculations

3.5.2.A Energy Loss Profiles

Since damage results from nuclear stopping events only, we can get an idea of the residual damage distribution by looking at the profile of energy deposited into nuclear stopping. Figs. 3.7a and b show TRIM calculations of the total energy lost to nuclear stopping and the energy going just into atomic displacements for a 250 keV boron implant and a 300 keV indium implant. Also shown is the energy lost to electronic stopping by the
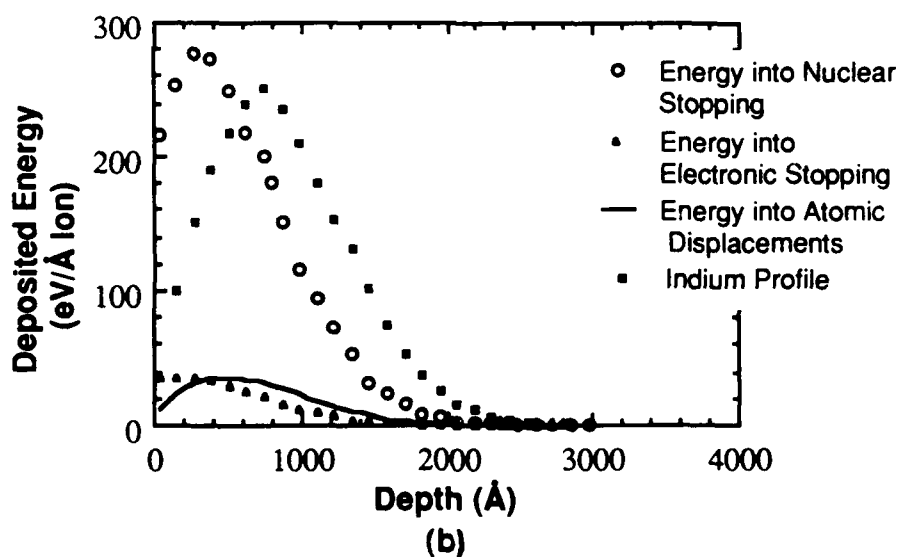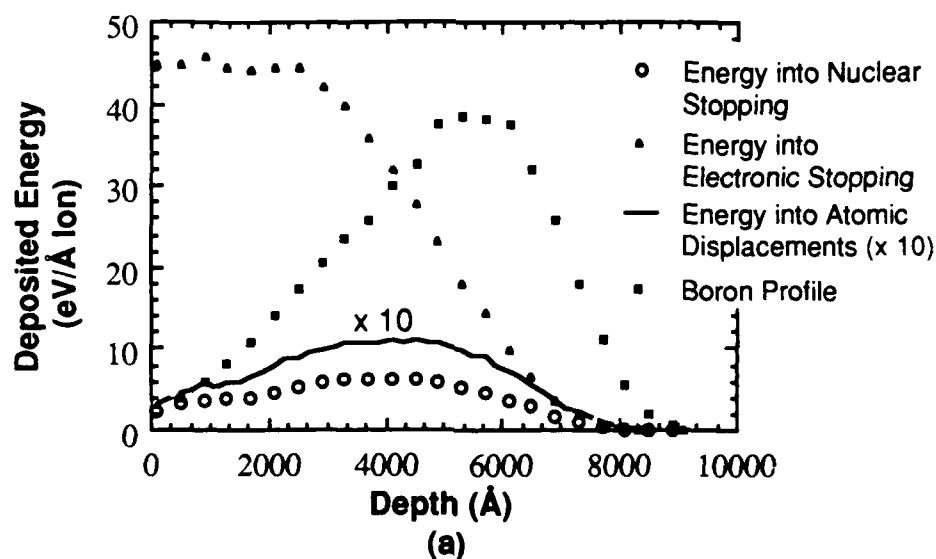
Fig. 3.7 Energy loss profiles calculated using TRIM for (a) a 250 keV boron implant and (b) a 300 keV indium implant. Included are the energy into nuclear stopping, the energy into electronic stopping, and the energy into atomic displacements, all in eV/(Å ion). The corresponding ion profiles are also shown for comparison. Note that the energy into atomic displacements in (a) has been multiplied by a factor of 10 for clarity.

implanted ion. For comparison, the SIMS profile for each implant is included. The energy going into atomic displacements is calculated from the total vacancy profile assuming a displacement energy of 10 eV. Note that for both light and heavy ions the peak in nuclear stopping is shallower than the peak of the implanted ion distribution.

As expected, the energy loss for boron is primarily electronic, accounting for 87% of the implant energy, with the maximum for nuclear stopping not occurring until the ions have reached a depth of about 4000 Å. This will result in relatively light damage near the surface with a buried damage layer near the peak in nuclear stopping. The opposite holds true for the indium ions which immediately begin to lose most of their energy to nuclear stopping as soon as they enter the surface. Nuclear stopping peaks at about 300 Å and accounts for almost 90% of the energy loss. The resulting damage in the near surface region will be quite heavy.

A comparison of the curves for nuclear stopping and for the energy going into atomic displacements illustrates the importance of the low-energy-transfer (LET) nuclear events discussed at the end of §3.3.2. So many of these events occur in the dense collision cascades near the end of ion and recoil ranges that they, rather than atomic displacements, account for the bulk of the nuclear energy loss. For boron fully 82% of the total nuclear stopping is due to LET events, increasing to almost 86% for indium because of the denser cascade caused by the heavier ions.

The shapes of the electronic and nuclear stopping curves can be explained as follows: For boron, ε_m, the maximum in universal nuclear stopping curve, occurs at about 14 keV (see Fig. 3.2). Our implant energy of 250 keV is well above this, so as the ions lose energy the portion lost to nuclear stopping will increase until the ion energy falls below ε_m, at which point the nuclear stopping power decreases. This will result in a nuclear stopping profile that rises gradually to a maximum as shown in Fig. 3.7a. The electronic

stopping profile for boron would decrease smoothly from a maximum at the surface, but energy transport by backscattered ions causes it to flatten out near the surface. For indium, ε_m is roughly equal to the implant energy, 300 keV. This would result in the nuclear energy loss curve having its maximum at the sample surface, but backscattered ions transport some of the implant energy right out of the sample, resulting in a nuclear energy loss peak slightly inside the sample. The explanation for the electronic energy loss profile is analogous to that for boron.

3.5.2.B Vacancy and Recoil Profiles

One common measure of radiation damage is the number of vacancies produced. BTE calculations of the vacancy profiles for each kind of target atom for the same implants as above are shown in Figs. 3.8a and b. Note that the integrals of the recoil and vacancy profiles for each type of lattice atom are equal since for every stopped recoil there exists a corresponding vacancy. We can estimate the average number of lattice displacements caused by each implanted ion from this integral and the implanted dose. Table 3.3 shows this information for some ions of interest implanted into MCT at different energies.

Table 3.3 DISPLACED ATOMS PER INCIDENT ION ($E_d = 10$ eV)

Ion	10 keV	300 keV
B	140	570
F	210	1180
In	340	3800

The vacancy concentration is higher than the stopped recoil concentration near the sample surface and vice versa deeper in the sample. This, in conjunction with the fact that the Cd and Te recoils have a greater range than the more massive Hg recoils will result in stoichiometric disturbances which may affect damage re$_{\!\!\!\!\!}$..'r and dopant activation. Stoichiometry imbalances will be discussed in the next section. Vacancy-rich and

interstitial-rich regions may also have an effect on dopant diffusion during the post-implant anneal. Such mechanisms are currently being suggested, for instance, to account for uphill diffusion of the implanted atoms during annealing of Be- or Mg-implanted GaAs [3.22].
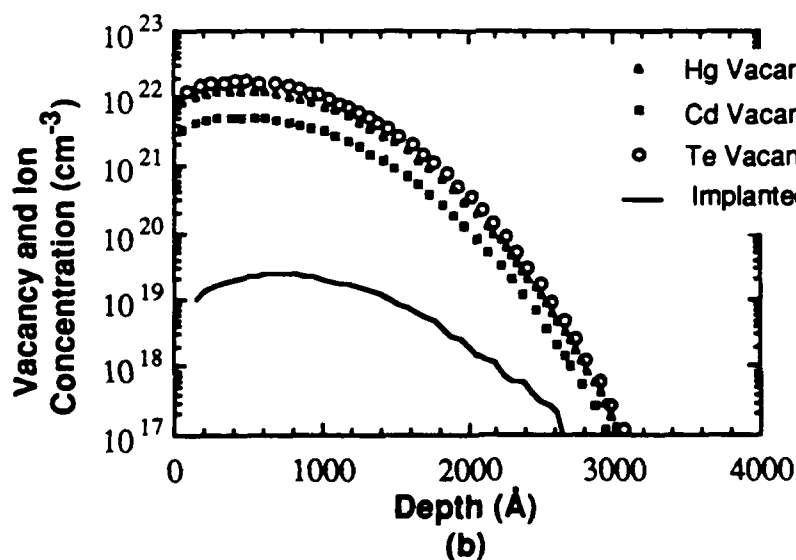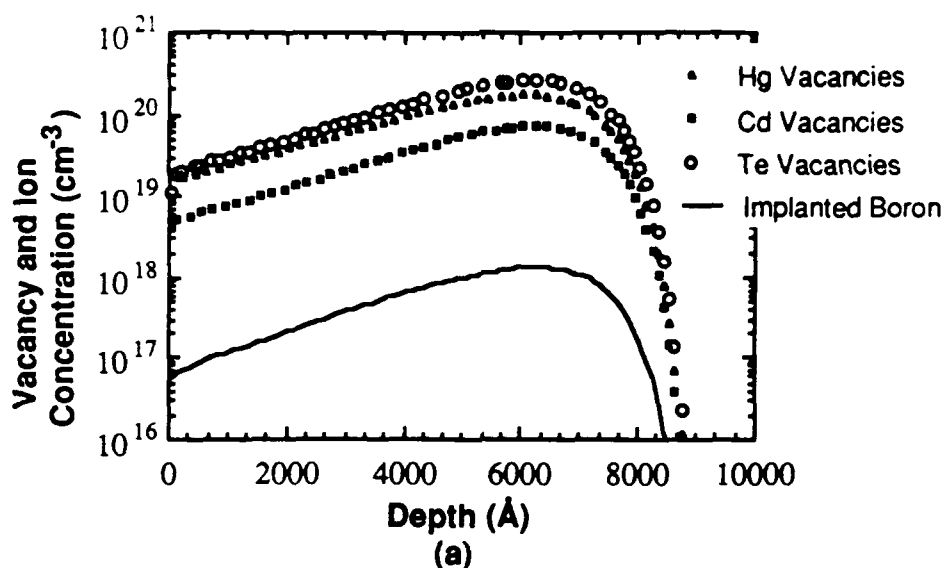
Fig. 3.8 Vacancy profiles calculated using the BTE method for (a) a 250 keV boron implant and (b) a 300 keV indium implant. Comparison with the corresponding ion profiles shows that the shapes of the implanted ion and vacancy profiles are quite similar.

3.5.2.C Stoichiometry Imbalances

Implantation into a compound semiconductor will cause stoichiometry disturbances within the implanted ion range because of the different collision cross sections and recoil ranges of the target constituents. This information can be found from BTE calculations using two steps. First the net concentration of each kind of target atom is calculated by subtracting the vacancy distributions from the stopped recoil distributions. As stated above, this results in a profile that has a net concentration of vacancies in the near surface region and a net interstitial concentration deeper in the target. This is shown in Figs. 3.9a and b which also shows how the vacancy-dominated region for Hg is slightly smaller because Hg recoils have a smaller range than Cd and Te recoils. The actual stoichiometry imbalance is then calculated by comparing the net concentration profiles of the different kinds of target atoms. For a ternary compound the relative ratios of each atom must be taken into account to see where the excesses and deficiencies of each type of atom appear.

Since MCT is generally considered to have Hg and Cd randomly distributed on metal sites, a simpler way of looking at the stoichiometry imbalance is through the ratio of metal atoms to Te atoms. In this case, we can just add the net concentrations of Hg and Cd together to obtain the net metal concentration and then subtract the net Te concentration. Breaking the problem up in this way makes sense in terms of diffusion, at least for substitutional species, because a Hg vancancy and a Cd vacancy should look the same to a dopant that is trying to substitute onto a metal site. Note that since Cd and Te have very similar ranges and will cancel each other out, the main contribution to the profiles is due to Hg recoils. Figs. 3.10a and b show such profiles for the same implants that we have been discussing above. The major feature to notice in both cases is that we get excess metal atoms slightly behind R_p and excess Te slightly beyond R_p. The figure is an especially good illustration of why the damage due to light ions like boron is referred to as a buried damage layer.
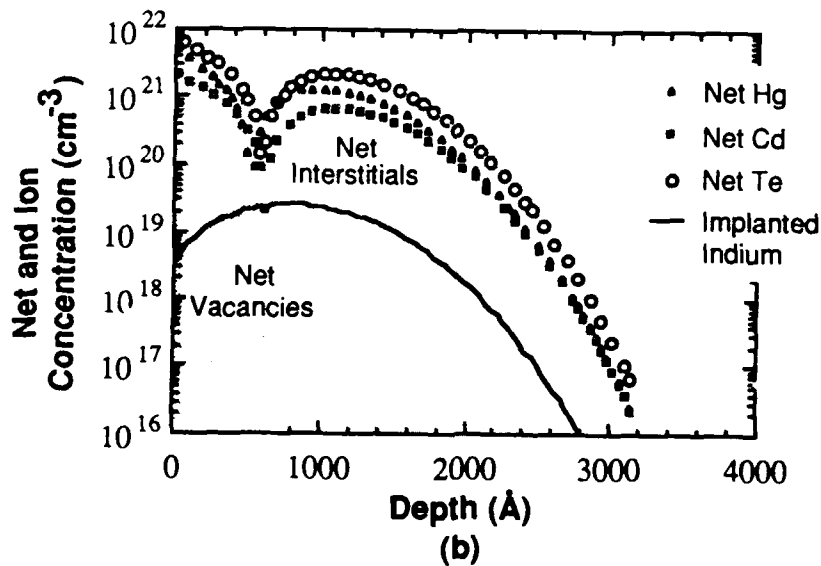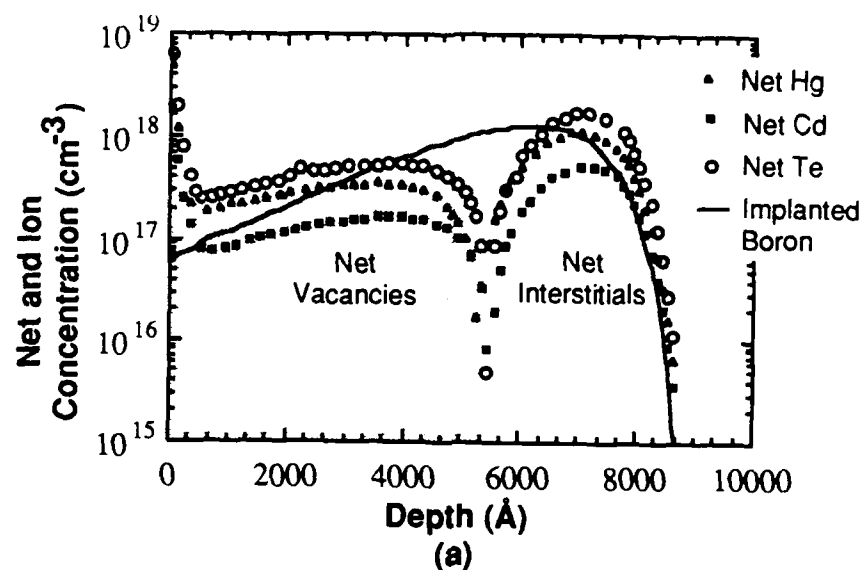
Fig. 3.9 Net concentration profiles of the constituents of the target calculated using the BTE method for (a) a 250 keV boron implant and (b) a 300 keV indium implant. Implants result in a net vacancy concentration near the surface, indicated by the shaded region, and a net interstitial concentration deeper in the sample. The corresponding ion profiles are again shown for comparison.
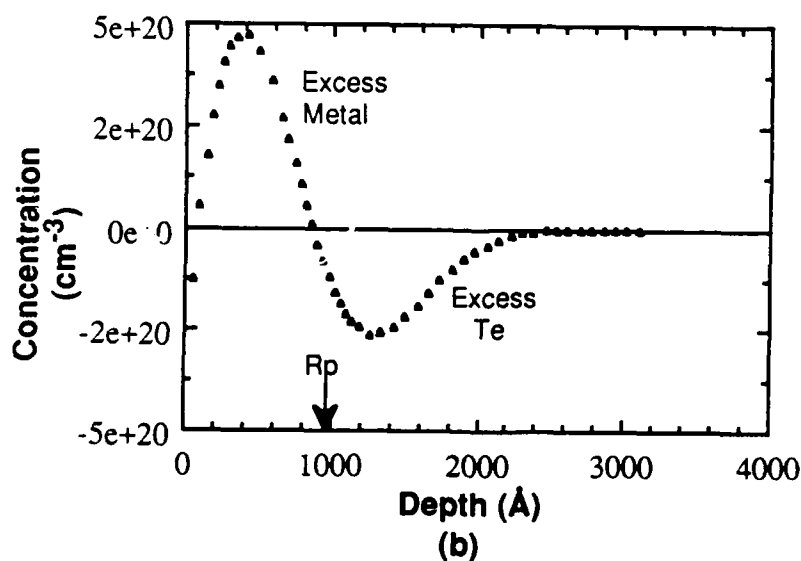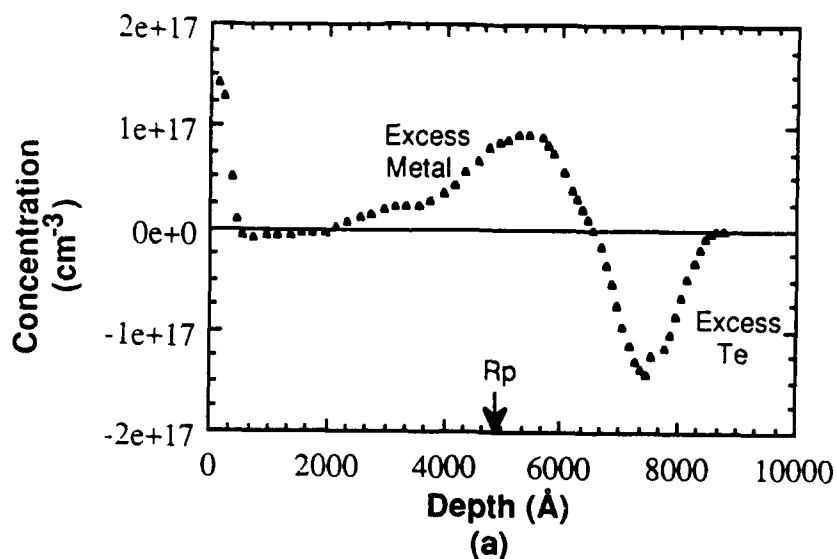
Fig. 3.10 Calculated stoichiometry imbalances caused by the implantation of (a) 250 keV boron and (b) 300 keV indium. Light ion implantation (a) results in excess metal atoms at the same depth as R_p and excess tellurium somewhat deeper than R_p. Heavy ion implantation causes a larger stoichiometry imbalance and results in excess metal atoms more shallow than R_p and excess tellurium atoms again beyond R_p.

3.5.3 Damage as Measured by Ion Channeling

3.5.3.A Mass Dependence

MeV channeling measurements show that, as expected, the character of the residual damage caused by a light ion is quite different from that due to a heavy ion. This is shown in Fig. 3.11 for 100 and 250 keV boron and 300 keV indium, all implanted to a dose of 10^{14} cm^{-2} at 77 K. Note that in this figure the data is plotted with a depth scale so the plot looks backwards when compared to the examples in Chapter 2. For convenience, most of the depth scales for channeled spectra in this chapter are calculated assuming a low level of damage (remember $dE/dx)_{ch} \approx 30\%$ lower than $dE/dx)_R$ from Chapter 2), though this is obviously less accurate for the heavily damaged indium-implanted sample in Fig. 3.11. The depth scale for such a heavily damaged sample is actually intermediate between that for a lightly damaged crystal and that for the random configuration.
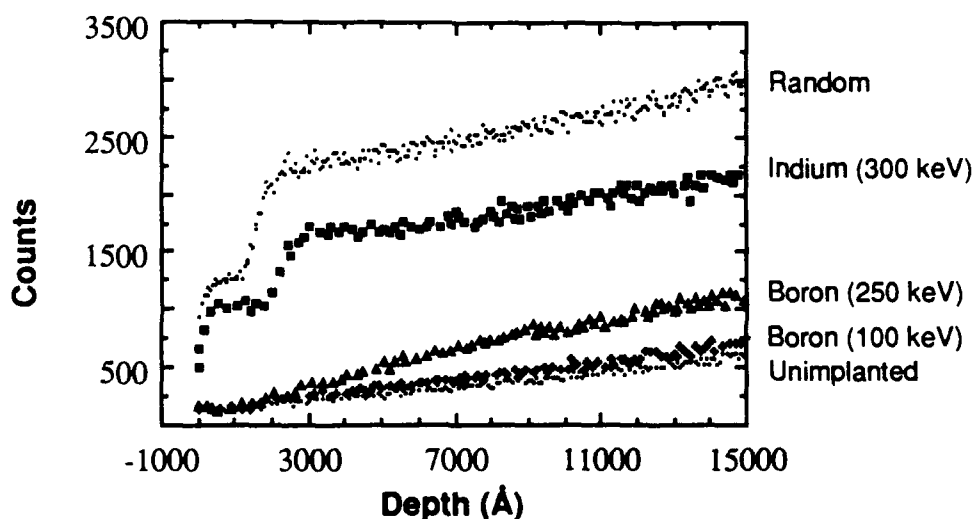
Fig. 3.11 Comparison of the damage measured by ion channeling caused by boron implanted at 100 and 250 keV to that caused by indium implanted at 300 keV. (All implants done at 77 K to a dose of 10^{14} cm^{-2}). The channeling spectra indicate that the damage due to the boron implants consists of extended defects whereas that caused by the indium implant consists of point defects.

As discussed in §2.3.2.C, a region containing a high density of point defects will cause a sharp peak to appear in the channeling spectrum since the incident ions are directly backscattered off of the displaced atoms. Extended defects, such as dislocations, gradually dechannel the ions moving through them causing the spectrum height to increase slowly for regions deeper in the target. From the above description, Fig. 3.11 indicates that the damage due to light ions consists primarily of extended defects, while heavy ions create a high density of point defects in the near surface region. Because the channeling spectrum for indium does not decrease much after the point defect peak, dislocations or loops are probably also contributing to the dechanneling at that depth.

Though both samples were implanted with the same dose of ions, the backscattered yields indicate that the damage from the indium implant is much higher than that caused by the boron implant, consistent with damage calculations in the previous section. The heavier damage caused by the indium implant means that channeling can easily detect damage from indium doses as low as 10^{12} cm^{-2} while boron doses must be at least an order of magnitude larger to get a significant difference between the unimplanted and damaged channeling spectra (see Fig. 3.12).

A closer look at the 250 keV boron channeling spectrum reveals that the damage level is very low for roughly the first 1000 Å, has an increasing slope for the next several thousand Ångstroms, and then becomes flatter at slightly less than 5000 Å (at about R_p). For lightly damaged samples dominated by extended defects the slope is proportional to the defect concentration. This suggests that there are few defects near the surface and that the defect density begins to increase at $\approx$ 1000 Å, and then decreases, or at least remains constant for depths beyond $\approx$ 5000 Å. This is exactly the sort of behavior predicted by the energy deposition profiles in Fig. 3.7a.

The damage profile from the indium channeling spectrum is more difficult to pick out because of interference from the Cd and Te edges. It is a uniform 87% of the random level for the entire region of the Hg sublattice resolved from Cd and Te, or for about the first 1000 - 1500 Å. At lower energies, where Cd and Te are also contributing, we see a small peak that could be due to either a) damage in the Hg sublattice extending to ≈ 3000 Å and very few Cd or Te point defects or b) damage in the Hg sublattice ending at ≈ 1500 Å and a moderate number of Cd and Te point defects in the first 1500 Å. Since a damage profile centered between 1000 and 1500 Å is in excellent agreement with the results of Bahir *et al.* for 300 keV In implants [3.23], we choose option (b). Note that for both indium and boron the damage profile is significantly deeper than nuclear damage peak. This effect is due to the loosely bound nature of MCT, similar to that of a metal, in which damage cascades are carried far into the crystal.

Assuming the Hg damage level decreases beyond ≈ 1500 Å, we calculate the damage level for the Cd/Te peak to be $\leq 76\%$. Compared with the 87% damage level for the Hg sublattice, this indicates that relatively more Hg atoms are displaced than Cd or Te atoms. This is consistent with a lower binding energy for Hg in the lattice and has been noted by other workers [3.24].

3.5.3.B Dose Dependence

Damage as a function of dose is shown in Fig. 3.12a for boron (spectra taken by T.-M. Kao) and Fig. 3.12b for indium, both implanted at 77 K. The character of the damage remains the same for boron as the dose is increased, though there is a large increase in the damage density between a dose of 10^{14} cm^{-2} and 10^{15} cm^{-2}. The spectra are consistent with Schaake's TEM results [3.25] in which he reports seeing dislocation loops only in samples implanted with boron at doses $> 10^{14}$ cm^{-2}. He was looking at the top 1000 Å and we can see from the figure that there is little or no damage in that region visible
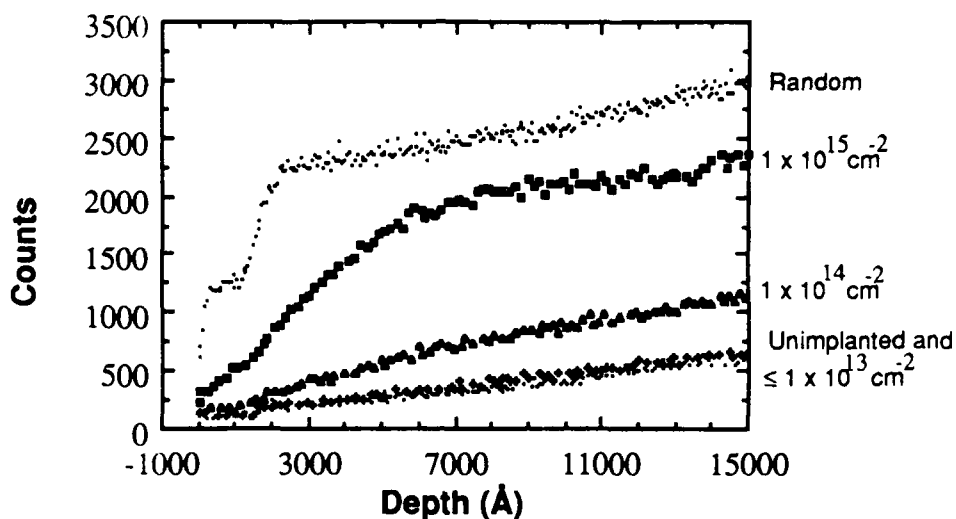
Fig. 3.12 (a) Damage, as measured by ion channeling, as a function of dose for 250 keV boron implanted at 77 K. The implanted and unimplanted channeling yields are equal for doses $\leq 10^{13}$ cm^{-2} and the damage has not saturated for doses as high as 10^{15} cm^{-2}. Other workers do see damage saturation for light ions implanted to doses $> 10^{15}$ cm^{-2}[3.22].
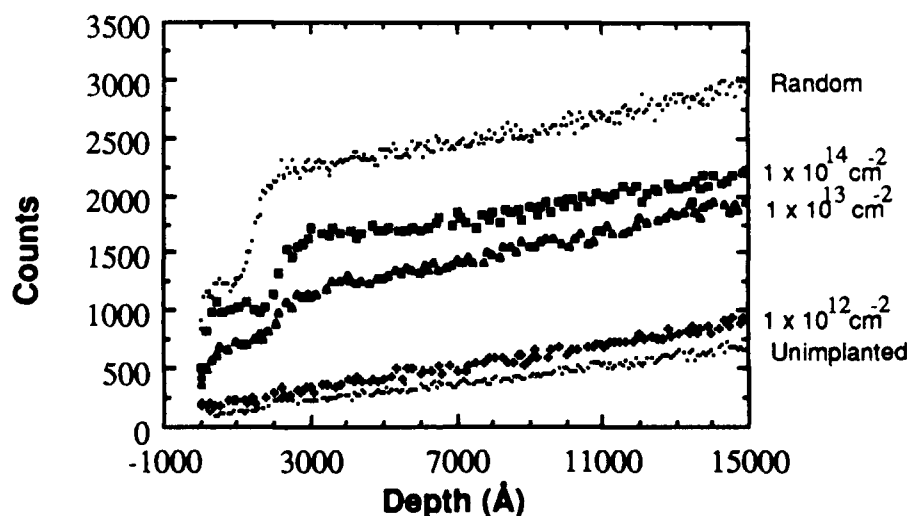
Fig. 3.12 (b) Damage, as measured by ion channeling, as a function of dose for 300 keV indium implanted at 77 K. There is a clear difference in backscattered yield between the implanted and unimplanted samples for doses as low as 10^{12} cm^{-2}, indicating that the density of the indium collision cascade is much greater than that due to boron. Damage saturation occurs for doses $\geq 10^{14}$ cm^{-2}.

to channeling for doses $\leq 10^{14}$ cm^{-2}. The break in slope in the dechanneling occurs at roughly the same depth for all of the doses, indicating that the damage profile does not shift as dose is increased.

The spectrum for the lowest indium dose differs very little from the lower dose boron spectra, though the indium damage does extend all the way to the surface. For this small dose the damage level is too low to decide whether it is due to point defects or extended defects. By the time the dose is increased to 10^{13} cm^{-2}, however, the damage is clearly dominated by point defects near the surface. At this dose we can clearly see the backscattered yield increasing with depth until the Cd and Te edges begin to interfere. At higher doses the damage is at its maximum at the surface of the sample and is flat for the first 1200 Å, indicating that the damage peak broadens and shifts toward the surface as the dose increases from 10^{13} cm^{-2} to 10^{14} cm^{-2}.

We can compare the damage near the surface for different doses using the expression:

$$\% \text{ defects} = \frac{\chi_{min}(\text{implanted}) - \chi_{min}(\text{unimplanted})}{1 - \chi_{min}(\text{unimplanted})} \times 100 \tag{3.8}$$

χ_{min} is the minimum yield, defined by the ratio $H_{aligned}/H_{random}$ of the heights of the channeling and random spectra taken just behind the Hg surface peak (corresponding to a depth of ≈ 300 Å in a highly damaged sample or ≈ 500 Å in slightly damaged material). Note that the portion of the spectrum from which χ_{min} is calculated is free of interference from Cd and Te and reflects only the state of the Hg sublattice. The % defects for all implants performed are shown in Table 3.4 and Fig. 3.13 shows % defects for the 77 K boron and indium implants. We see that samples are never amorphous after any of the implants, though saturation of the backscattered yield does occur for indium at doses $\geq$ 10^{14} cm^{-2}. No signs of saturation are evident for even the highest boron dose (10^{15} cm^{-2}). These observations are consistent with [3.23, 3.26] in which saturation was reached for
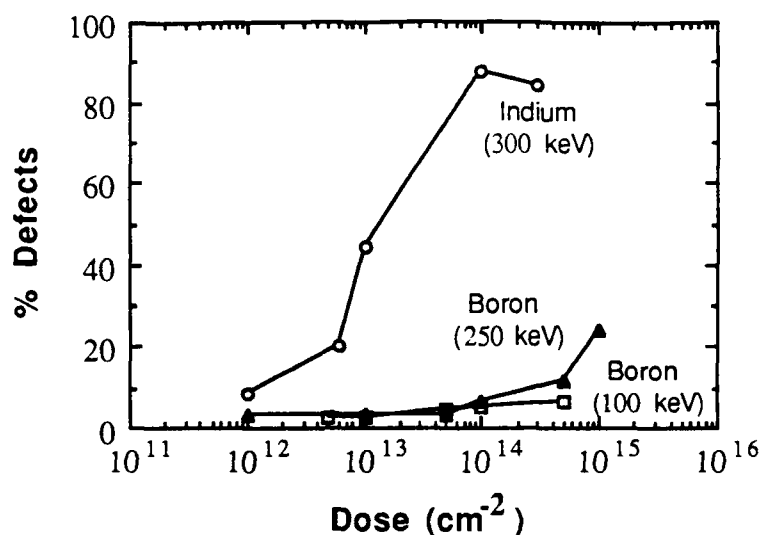
Fig. 3.13 Damaged fraction as a function of dose for 100 and 250 keV boron and 300 keV indium implanted at 77 K. % defects is calculated using (3.8) and the % defects for all implants done in this work is shown in Table 3.4.

Table 3.4 % DEFECTS FOR ALL IMPLANTS

Ion, Temperature, Energy (keV)	B, 77 K 100	B, 77 K 250	B, RT 250	In, 77 K 300	In, RT 300	F, 77 K 350	Ne, 77 K 180
Dose (cm^{-2})							
1 x 10^{12}				8.67			
5 x 10^{12}	2.9						
6 x 10^{12}				20.55			
1 x 10^{13}	2.9			44.67	15.33		
3.8 x 10^{13}						9.14	
5 x 10^{13}	4.63	2.96					15.13
1 x 10^{14}	5.39	6.33	2.93	87.34			
3 x 10^{14}				84.62			
5 x 10^{14}	6.73	11.82					
1 x 10^{15}		24.48					

heavy ion doses $\approx 10^{14}$ cm^{-2} and for boron doses $> 10^{15}$ cm^{-2}. TRIM calculations show good agreement between the deposited energy density to reach saturation for these two implants, $\approx 4.3 \times 10^{25}$ eV cm^{-3} for our 10^{14} cm^{-2} indium implant and ≥ 1.6 10^{25} eV cm^{-3} for a $\geq 10^{15}$ cm^{-2} 250 keV boron implant.

3.5.3.C Energy Dependence

Increasing the energy of the incident ions increases both the depth of the damage profile and its magnitude as illustrated in Figs. 3.11 and 3.13. Note that at lower doses in Fig. 3.13 the % defects for the 250 keV boron implant is actually lower than that for the 100 keV implant. Since % defects is calculated at the same depth for all of the samples and does not take into account the fact that the damage peak from a higher energy implant is "buried", it is is better to use it to compare different dose implants rather than implants done at different energies. This effect of implant energy on the damage depth is more obvious using grazing angle geometry as shown in Figs. 3.14a and b. For the 250 keV implant the figure shows no increase in backscattered yield over the unimplanted sample for at least the first 1000 Å. In contrast, the 100 keV implant, though it shows less total damage in Fig. 3.11 shows damage all the way to the surface in Fig. 3.14.

3.5.3.D Temperature Dependence

In Fig. 3.15 we compare channeling spectra for 250 keV, 10^{14} cm^{-2} boron implants at room temperature and 77 K. Similar spectra for 300 keV, 3×10^{14} cm^{-2} indium implants at 77 K, room temperature, and intermediate temperatures are shown in Figs. 3.16a and b. For both boron and indium, the room temperature and 77 K implants were carried out with good thermal bonding of the target to the sample holder. The intermediate temperature indium implants (subsequently referred to as 77+ and RT+) were carried out nominally at 77 K and room temperature, but with the target lightly clipped onto the sample holder
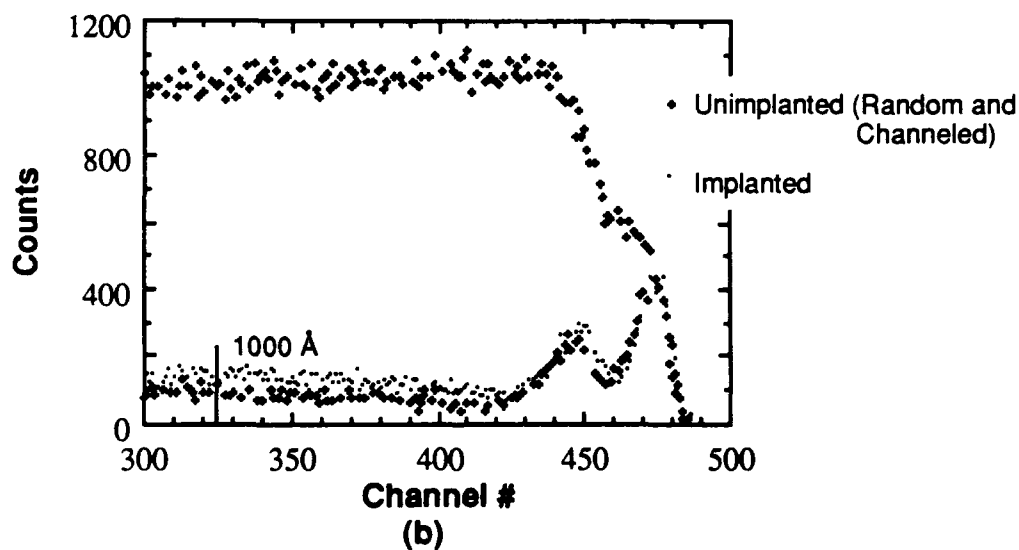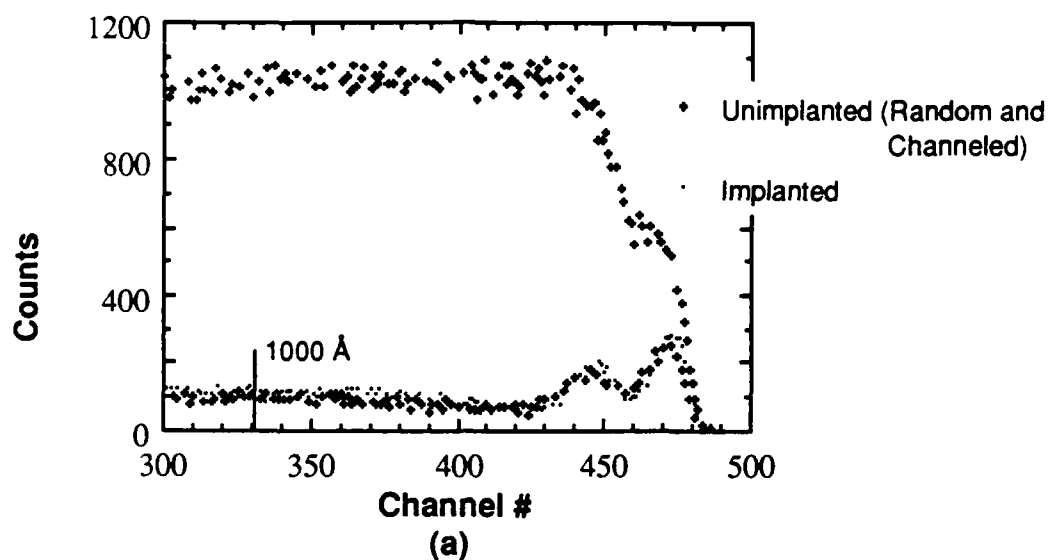
Fig. 3.14 The effect of implant energy on the depth of damage as measured by ion channeling in the grazing angle configuration for (a) 250 keV and (b) 100 keV boron. In (a) the backscattered spectrum from 250 keV boron implanted to a dose of 10^{14} cm^{-2} at 77 K shows no increase over the unimplanted spectrum to a depth of 1000 Å. In contrast, in (b) the backscattered spectrum from boron implanted at the same dose and temperature, but lower energy, shows damage all the way to the surface.
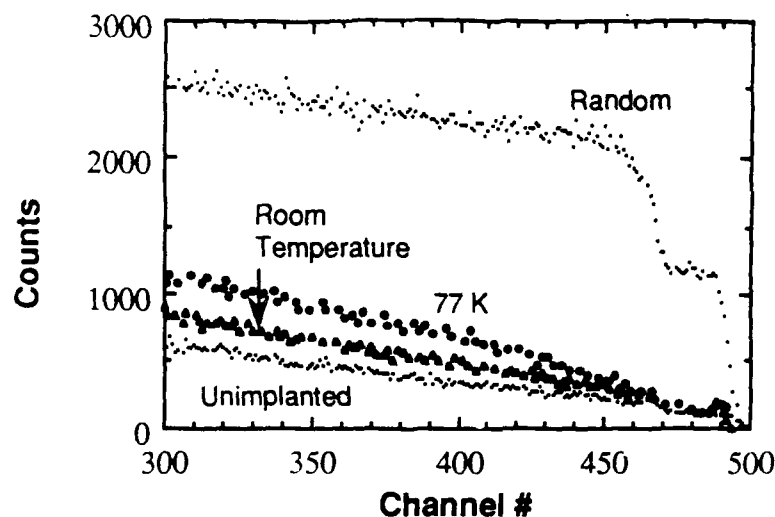
Fig. 3.15 The effect of implant temperature on damage caused by a boron implant as measured by ion channeling. Implant conditions: temperature = 77 K and room temperature, dose = 10^{14} cm^{-2}, energy = 250 keV. Increasing the temperature increases both the thermal and dynamic annealing rates, resulting in less residual damage.

(beam heating is discussed in Chapter 4). It is clear from the figures that much more dynamic annealing occurs during implantation at room temperature than at 77 K for both light and heavy ions. The most dramatic differences occur for the indium implants, where the character of the damage at the surface changes from point defects for the 77 K implant to extended defects for the room temperature implant. The 77+ case still exhibits point defects very near the surface with a height equal to the 77 K case (87% of the random level), but the defect profile begins to decrease at a depth of 500-600 Å, reaching a minimum of 58% of the random level at ≈ 1000 Å. Any further reduction of the yield in the Hg sublattice deeper than 1000-1200 Å is masked by the appearance of the Te edge, but a peak due to Cd and Te point defects can be seen at point (2) on the figure. Assuming that the damage in the Hg sublattice remains near the 60% level, we can subtract out that contribution to the height at point (2), which gives us a damage level of ≈ 43% due to Cd and Te at the surface and a damage level of ≈ 35% at point (3). Not only is the Hg sublattice more heavily damaged than the Cd or Te sublattices during an implant (see §A
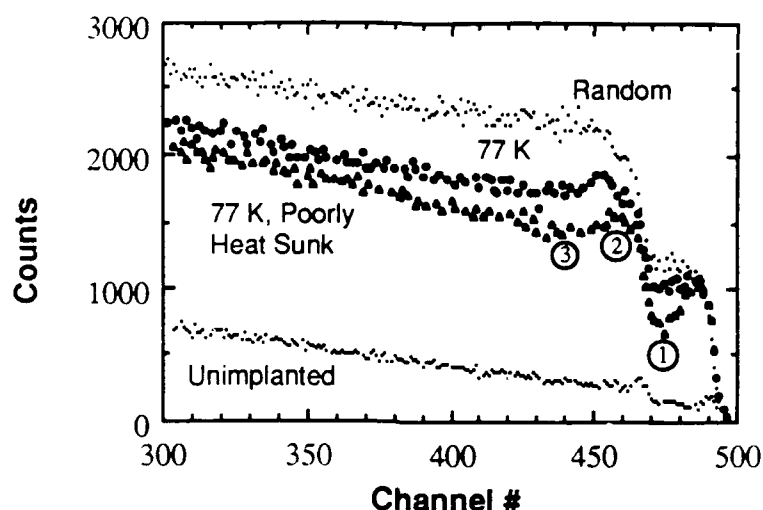
Fig. 3.16 (a) Damage as measured by ion channeling due to indium implanted at 77 K with good and poor thermal contact between the sample and the sample holder. The moderate (60-80 C°) temperature rise in the poorly heat sunk sample, in combination with beam induced effects, increases the defect mobility enough to cause partial epitaxial regrowth beneath the sample surface. The numbered regions are discussed in the text.
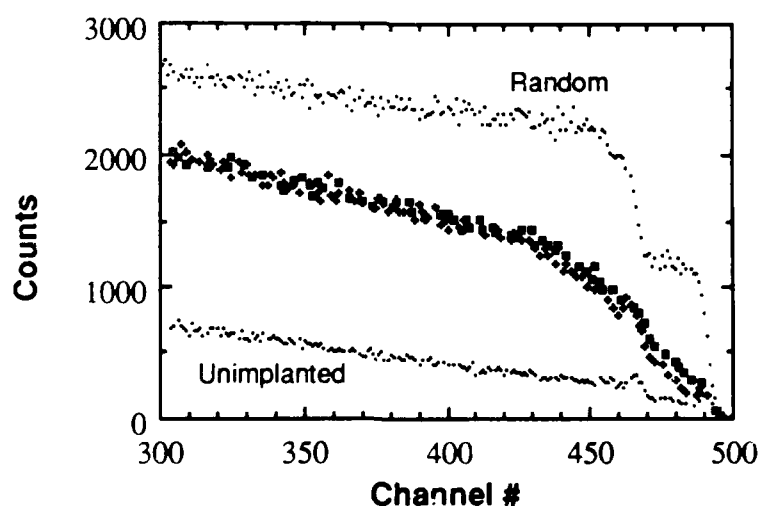
Fig. 3.16 (b) Damage as measured by ion channeling due to indium implanted at room temperature with good and poor thermal contact between the sample and the sample holder. In contrast to the cold implant shown in figure 3.16 a, at room temperature and above, almost all of the point defects are able to dynamically anneal to form extended defects. Defect mobilities are already so high at room temperature that the mobility increase caused by beam heating or other beam-induced effects has little effect and the backscattering spectra coincide.

above), but it is more difficult to get Hg atoms back on their lattice sites during annealing.

Though the 77 K+ implant has a distinctly different damage profile than the 77 K implant, the channeling spectrum for the RT+ implant is virtually identical to that for the RT implant. Clearly residual implantation damage is much more sensitive to implant parameters at low temperatures than near room temperature.

3.5.3.E Discussion

The final configuration of damage resulting from implantation depends on the balance between damage production and annealing. Two types of annealing can take place during implantation 1) dynamic annealing of a single ion track and 2) bulk annealing of damaged layers.

Dynamic annealing can be described as follows: An implanted ion creates a heavily damaged region about its track, the initial size of which is determined primarily by the ion mass. The volume of the damaged region is quickly reduced as atoms on the outer edges reform bonds and change their positions and as vacancies diffuse out from the vacancy-rich core to the interstitial-rich periphery. The extent of this process, which depends on the temperature and the density of the collision cascade, determines how much, if any, of the damaged zone survives. In contrast, bulk annealing occurs because of the movement of defects in already damaged layers. If defects are sufficiently mobile, annealing can proceed via solid phase epitaxy from undamaged crystal beneath the damaged region. Simple thermal annealing may be enhanced by mobile defects produced by the ion beam [3.27 – 3.29] and it will certainly be increased if any beam heating (discussed in Chapter 4) occurs.

These concepts can account for the dose and temperature dependences exhibited by the channeling spectra above. For boron, the collision cascades are not very dense and the point defect mobility is high enough even at 77 K for the most heavily damaged regions to regrow better crystal. Thus as the dose builds up, most of the point defects created by the

implant dynamically anneal and agglomerate into dislocation loops [3.25]. Increasing the dose increases the density of these loops until they interact to form complicated dislocation entanglements. Once a dislocation network forms, further irradiation acts not to increase the total number of defects, but only rearranges the entanglement, resulting in damage saturation. Collision cascades are much more dense for indium, causing the formation of defect complexes in addition to dislocation loops during the implant. The point defect concentration thus increases with dose, as shown by RBS.

Increasing the temperature of the implant increases the mobility of point defects which increases both the dynamic and the bulk annealing rate. The defect complexes formed during 77 K indium implants thus do not form at higher temperatures which is why the channeling spectra for room temperature indium implants are dominated by extended rather than point defects. For both heavy and light implants the room temperature defect mobility is high enough for bulk annealing to occur all the way to the surface, reducing the number of residual defects.

The 77+ K indium implant is an interesting case. Here the annealing rate has increased only enough to allow partial regrowth from the undamaged crystal towards the surface. The regrown crystal is still highly defective, as demonstrated by the height of the channeled spectrum, but the point defect concentration below the surface is reduced significantly. Temperature calculations (see Chapter 4) suggest a beam-induced temperature rise on the order 60 - 80 C°. It is conceivable that the defect mobility is high enough at this temperature to allow significant thermal annealing, but there is probably an additional mechanism at work. Several workers have reported ion beam-induced epitaxy in silicon at temperatures well below those required to induce epitaxy thermally [3.27 – 3.29]. Their results are inconsistent with simple beam heating and are attributed to the generation of mobile point defects by the ion beam. This explanation is supported by some oddities in the SIMS profiles of these indium implants, shown in Fig. 3.17. We see that the RT and

RT+ implants have significantly deeper tails than the 77 K implants. Also, the tail of the 77+ K implant is as deep as those of the RT implants. Since these temperatures are far too low to permit thermally activated indium diffusion [3.3], a more likely explanation is that the combination of a substrate temperature somewhat higher than 77 K and the presence of highly mobile ion beam-induced defects causes enhanced indium diffusion.
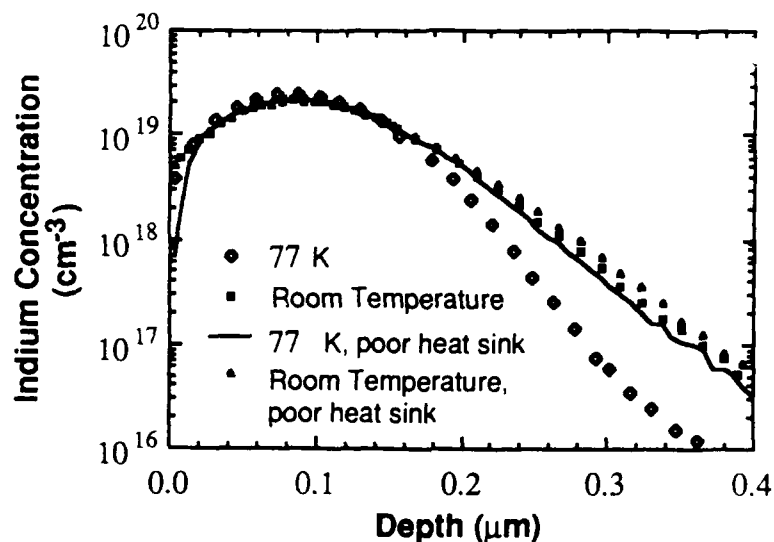
Fig. 3.17 SIMS profiles of the indium implants discussed in Fig. 3.16. Since it is known that post-implant annealed indium profiles do not move for temperatures < 250° C [3.3], the deep indium tails on the room temperature and 77 K poorly heat sunk implant must be due to beam-enhanced diffusion.

In no case do we observe the formation of an amorphous layer in MCT as we do with high dose implants into Si and GaAs. However, there is some evidence that higher dose implants of heavy ions at 77 K may amorphize the MCT at the implantation temperature and that the amorphous layer anneals as the sample is warmed up to room temperature. K.C. Dimiduk implanted 120 keV boron dichloride to a dose of 10^{15} cm^{-2} at 77 K [3.30] with a piece of foil covering part of the MCT to provide an unimplanted control sample. Following implantation the samples were brought back to room temperature as quickly as possible ($\approx$ 15 minutes). She reports that at first the unimplanted surface was clearly distinguishable from the implanted surface, but that the distinction

began to fade with time. By the time RBS measurements were performed the samples were not amorphous. She suggests that the implanted surface had been amorphized, but that it annealed at room temperature.

The behavior of the 77 K indium damage profile as the dose is increased can be interpreted to support this argument. As the dose is increased from 10^{13} cm^{-2} to 10^{14} cm^{-2} we see that the damage profile changes from having a peak well inside the sample to being uniform from the surface to the Te/Cd edge. This broadening of the damaged region toward the surface is very similar to the amorphization of Si and GaAs except that the portion is not as high as the random level. We suggest that the sample actually is being amorphized when it is implanted with indium doses $\geq 10^{14}$ cm^{-2} at low temperatures, but that the concentration of point defects frozen in at 77 K is too high to be in equilibrium at room temperature. These excess point defects anneal down to their equilibrium concentration as the sample is brought to room temperature, forming the flat damage profile seen in the channeling spectra for doses $\geq$ the saturation dose. In samples implanted at room temperature stable point defects never form because of beam enhanced dynamic annealing, but if they are already there, as with the 77 K implants, a high enough concentration is stable to dominate the channeling spectrum.

3.5.4 Electrical Characteristics of As-implanted Samples

3.5.4.A Background

Implantation of "anything" into p-type MCT always forms an n$^+$ layer with a maximum carrier concentration of about 2-3 x 10^{18} cm^{-3}. The doping effect is considered to be due to radiation damage though the identity of the electronically active defects is as yet unknown. Sheet and differential van der Pauw measurements were carried out on various as-implanted samples in conjunction with the RBS measurements above in an effort to better understand this doping effect.

3.5.4.B Dose Dependence

A plot of the average sheet carrier concentration versus dose is shown in Fig. 3.18 for 300 keV indium implants and 100 and 250 keV boron implants. For the boron implants the sheet carrier concentation increases with increasing dose until it saturates at about 10^{14} cm^{-2} (μ_{Hall} = 4000-5000 cm^2 V^{-1} s^{-1}) for doses $\geq 10^{13}$ cm^{-2}. The sheet carrier concentration for the indium implants appears to have already saturated at 3-4 x 10^{13} cm^{-2} (μ_{Hall} ≈ 2000 cm^2 V^{-1} s^{-1}) at the lowest dose of that implant series, 10^{12} cm^{-2}. By referring to §3.5.3.B we see that for both light and heavy ions electrical saturation occurs at much lower doses than damage saturation as measured by channeling in agreement with other workers' results [3.23, 3.31].
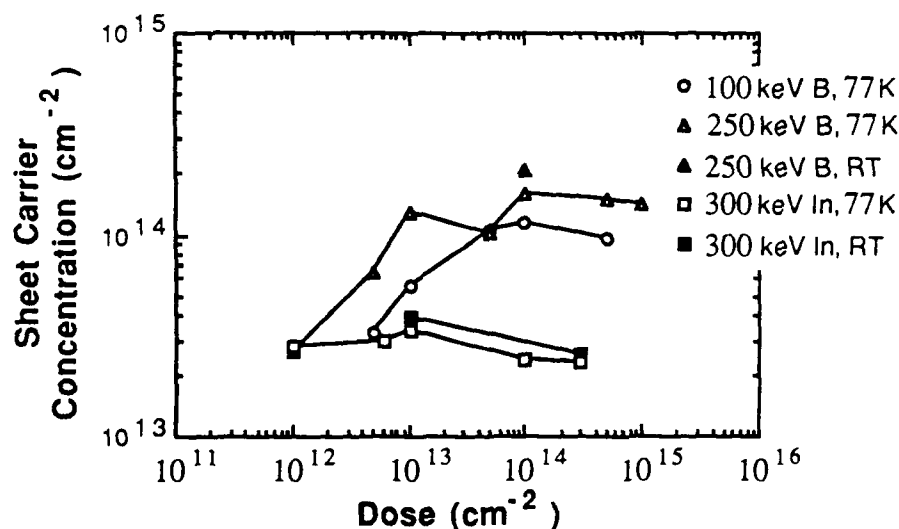
Fig. 3.18 Sheet carrier concentration as a function of dose for boron and indium implanted at 77 K and room temperature. Sheet carrier concentrations are consistently higher for the lower mass implants, implants done at higher temperatures, and implants done at higher beam energies.

For doses below that required for saturation the sheet carrier concentration is frequently an order of magnitude higher than the implanted dose and increases sublinearly with increasing dose. It is thus quite obvious that the electrical activity in as-implanted material is not directly due to the implanted atoms but rather to electrically active damage

caused by the implant. Unfortunately the defect doping mechanism is more complicated than models involving simple, charged point defects because if that were the case the concentration of donor-like defects would increase linearly with dose. Channeling measurements show that many of the point defects coalesce into dislocation loops and probably other, more complicated defect complexes, some of which must be responsible for the electrical activity.

3.5.4.C Ion mass

Fig. 3.19 shows as-implanted sheet carrier concentrations for several different ions implanted at 77 K. The most obvious feature of the plot is that carrier concentration decreases with increasing ion mass. This can also be seen in Fig. 3.18 where we see that the sheet carrier concentration obtained for the indium implants is significantly lower than that for boron at all except the lowest boron doses. We suspect that this effect is related to the density of the collision cascade produced by each ion. The basic idea is that the dynamic annealing of the dense collision cascades produced by heavy ions is reduced compared to the dynamic annealing of damage due to light ions and that less dynamic
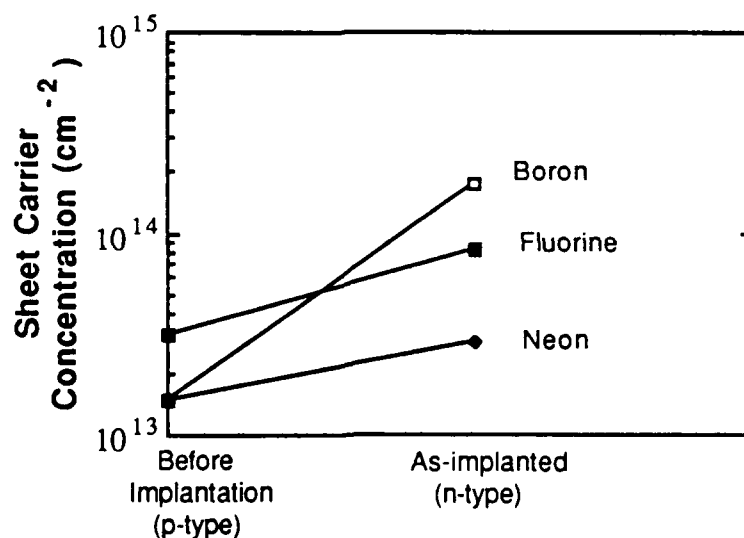
Fig. 3.19 Sheet carrier concentration for implants with different collision cascade densities. Carrier concentration decreases as the calculated density of the collision cascade increases.

annealing reduces the net n-type doping. Channeling spectra show (see Fig. 4.6) that the more heavily damaged samples are indeed the ones with the lower carrier concentrations. Possible mechanisms by which inefficient annealing could decrease the carrier concentration include: 1) It is the defect complexes formed by dynamic annealing that are electrically active or 2) Different types of defect complexes are formed by dynamic annealing. Most are electrically active (n-type), but some inhibit activation. Denser collision cascades increase formation of the latter. Saturation of carrier concentration with increasing dose could be explained using (2) if the overlapping of collision cascades also favors formation of the activation-inhibiting defect complexes.

3.5.4.D Implant Temperature and Energy

Implant temperature and energy have a slight effect on the carrier concentration as shown in Fig. 3.18. Increasing the implanted boron energy from 100 keV to 250 keV results in a small increase in carrier density, though it should be noted that implant energy is reported to be unimportant for boron energies $\geq$ 150 keV [3.31]. In addition, we observe that doping efficiency is consistently higher for room temperature implants than for cold implants, in agreement with [3.31]. An increase in carrier concentration with increasing energy is consistent with the discussion in the prevous section. Nuclear stopping decreases with increasing energy for boron energies > 14 keV (see Table 3.1), so collision cascades created by 250 keV B ions will anneal more efficiently than those created by 100 keV B ions, resulting in a higher carrier concentration. The increase in carrier concentration with increasing temperature is also consistent, since we know that thermal and dynamic annealing rates increase with increasing temperature.

3.5.4.E Differential Hall Measurements

Differential Hall measurements were performed on samples implanted with different ions to determine the carrier distributions. The details of the carrier profiles depend on the mass, energy, and implant dose, but we do observe several general trends. For the same

dose, as the ion mass increases the maximum in the carrier profile decreases, consistent with the discussion above. For all the cases we studied the electrical junction was deeper than the metallurgical junction because of the enhanced diffusion of n-type defects from the implanted region discussed in §3.5.3.E. Diffusion of the n-type defects is also responsible for the p- region that we frequently observe extending several thousand Å deeper than the junction (beyond which we obtain the original substrate parameters). Such a region was also noted by Kao [3.26] in his studies of carrier profiles as a function of boron dose. Whether the p- region appears, and its extent depend on the original background doping and defect structure of the unimplanted MCT.

3.6 Summary

In this chapter we presented the calculations from two implantation simulators of atom and damage profiles for several ions implanted into MCT and compared them to experimental results. Predicted ion ranges are in good agreement with our SIMS results and published data. We are also able to get excellent fits to SIMS atomic profiles for boron and indium. Damage in as-implanted samples is measured using MeV ion channeling and is found to follow the general trends expected from the simulations, though it is somewhat deeper than the calculations predict. This is in agreement with data in the literature and is attributed to the loosely bound nature of MCT, similar to that of a metal, in which damage cascades are carried far into the crystal. We find that the relatively more Hg atoms are displaced from their lattice sites than Cd or Te during implants at least with heavy ions and see evidence that it is also more difficult to repair the Hg sublattice. This is consistent with the weak binding of Hg in MCT. Defect doping mechanisms and defect mobility have been discussed and it is suggested that electrical properties of as-implanted samples are determined by the balance between different types of defect complexes produced by dynamic and bulk annealing during the implant. Dynamic annealing of denser collision

cascades and at low implantation temperatures produces relatively fewer of the n-type

defect complexes responsible for the n+ doping of as-implanted MCT.

3.7 References

[3.1] T.E. Seidel, "Ion Implantation," in *VLSI Technology*, Ed. S.M. Sze, McGraw-Hill Book Company, San Francisco, 1983.

[3.2] J. Narayan and O.W. Holland, J. Electrochem. Soc.: Solid-State Sci. and Technol., **131**(11), 2651 (1984).

[3.3] G.L. Destefanis, J. Vac. Sci. Technol. A, **3**(1), 171 (1985).

[3.4] R. Kalish, R. Fastow, V. Richter, and M. Shaanan, Appl Phys. Lett. **51**(15) 1158 (1987).

[3.5] J.F. Ziegler, J.P. Biersack, and U. Littmark, *The Stopping and Range of Ions in Solids*, Pergamon Press, New York, 1985.

[3.6] G. Carter and W.A. Grant, *Ion Implantation of Semiconductors*, Halsted Press, New York, 1976.

[3.7] J.P. Biersack and J.F. Ziegler, "The Stopping and Range of Ions in Solids," in *Ion Implantation Techniques*, Springer-Verlag, New York, 1982.

[3.8] S. Kreussler, C. Varelas, and W. Brandt, Phys. Rev. B, **23**, 82 (1982).

[3.9] W. Brandt and M. Kitagawa, Phys. Rev. B, **25**, 5631 (1982).

[3.10] J.W. Mayer, L. Eriksson, and J.A. Davies, *Ion Implantation in Semiconductors*, Academic Press, Inc., New York, 1970.

[3.11] G. Dearnaley, J.H. Freeman, R.S. Nelson, and J. Stephen, *Ion Implantation*, North-Holland, Amsterdam, p. 174, 1973.

[3.12] J.F. Gibbons and S. Mylroie, Appl. Phys. Lett. **22**, 568, (1973).

[3.13] L.A. Christel, An Application of the Boltzmann Transport Equation to Ion Implantation in Multilayered Targets, Ph.D. Thesis, Stanford University, August 1981.

[3.14] M.D. Giles, Multiple Pass Application of the Boltzmann Transport Equation to Ion Implantation Calculation in Multilayer Targets, Ph.D. Thesis, Stanford University, March 1984.

[3.15] J.P. Biersack, Nucl. Inst. and Meth. **174**, 257 (1980).

[3.16] H. Ryssel, and J.P. Biersack, Ion Implantation Models for Process Simulation, in *Process and Device Modeling*, W.L. Engl, ed. Elsevier Science Publishers B.V. (North-Holland), 1986.

[3.17] R.G. Wilson, J. Crystal Growth, **86**, 735 (1988).

[3.18] K.J. Riley, J.M. Myrosznyk, P.R. Bratt, and A.H. Lockwood, IEEE Trans. Elec. Dev., **ED-26**(11), 1840 (1979).

[3.19] S.Y. Wu, W.J. Choyke, W.J. Takei, A.J. Noreika, M.H. Francombe, and R.B. Irwin, J. Vac. Sci. Technol., **21**(1), 255 (1982).

[3.20] L.O. Bubulac, D.S. Lo, W.E. Tennant, D.D. Edwall, and J.C. Robinson, J. Vac. Sci. Technol. A, **4**(4), 2169 (1986).

[3.21] J. Baars, A. Hurrle, W. Rothemund, C.R. Fritzsche, and T. Jakobus, J. Appl. Phys. **53**(3), 1461 (1982).

[3.22] private communication from H.G. Robinson.

[3.23] G. Bahir and R Kalish, J. Appl Phys., **54**(6), 3129 (1983).

[3.24] G. Bahir, T. Bernstein, and R. Kalish, Rad. Eff. **48**, 247 (1980).

[3.25] H.F. Schaake, J. Vac. Sci. Tech., A **4**(4), 2174 (1986).

[3.26] T.-M. Kao, Development of Direct Ion Implantation Processes and Characterization Techniques for Mercury Cadmium Telluride Epilayers, Ph.D. Thesis, Stanford University, May 1987, p. 67.

[3.27] R.G. Elliman, S.T. Johnson, A.P. Pogany, and J.S. Williams, Nucl. Inst. and Meth. Phys. Res. B7/8, 310 (1985).

[3.28] S. Cannavo, M.G. Grimaldi, E. Rimini, G. Ferla, and L. Gandolfi, Appl. Phys. Lett., **47**(2), 138 (1985).

[3.29] B. Svensson, J. Linnros, and G. Holmen, Nuc. Inst. and Meth. **209/210**, 755 (1983).

[3.30] K.C. Dimiduk, Mercury Loss, Annealing and Ion Implantation in Mercury Cadmium Telluride, Ph.D. Thesis, Stanford University, July 1983.

[3.31] G.L. Destefanis, Nucl. Inst. and Meth. **209/210**, 567 (1983).

Chapter 4
Rate Effects

4.1 Introduction

The importance of implant variables such as ion mass, ion energy, target temperature, and ion dose in determining the residual damage after ion implantation was discussed in Chapter 3. An additional factor, the dose rate (ion flux), was mentioned in the context of beam heating, but was not examined in detail. This chapter addresses ion flux and other rate effects on residual damage in MCT and compares calculations with experiment.

Like the other implant variables, the ion flux influences residual damage because it affects the balance between damage production and annealing during ion implantation. The different mechanisms include simple beam heating and true dose or damage rate effects. High flux implantation conditions cause a bulk temperature rise in the sample (beam heating). As discussed in §3.5.3.E, this increases the bulk annealing rate and will result in reduced residual damage. If, however, the target temperature is kept constant and the flux is increased, collision cascades will begin to interfere with each other before the dynamic annealing of their outer regions is complete. This results in increased residual damage for the same implanted dose; that is, a dose-rate effect.

Even in silicon, which has a relatively high thermal conductivity, beam heating is a problem for high current implanters and also in medium current implanters configured so that only one wafer is implanted at a time [4.1]. Since the temperature of the implanted material can be raised by hundreds of degrees the need for effective wafer cooling is obvious. Measures taken include batch processing to spread the power over a larger area and improving the thermal conduction through the back surfaces of the wafers by tightly clamping the wafer to the sample holder or by filling the space between wafer and holder

with a gas [4.2]. Though these methods have proven to be adequate for silicon, the situation is more critical for MCT which has an extremely low thermal conductivity (about 1% that of silicon) and will lose Hg if heated to more than about 100° C. Any attempts at improving thermal conduction involving stress to the wafers are highly undesirable for MCT because of its poor mechanical properties, though processing in batch mode might be feasible. In any case, no calculations of actual temperature rises during implants have been reported for MCT. We have calculated the temperature versus time for the dwell time of an ion beam on a spot on the surface of a sample and in some cases have extended our calculation to find the equilibrium temperature as well. The method and sample calculations for silicon and MCT are presented in §4.2.

Though dose-rate effects have been reported for implantation in both silicon [4.3] and gallium arsenide [4.4] they have little technological importance in these materials and are studied primarily to improve our understanding of damage production during ion implantation. Academic interest alone is sufficient reason to look for a flux effect in MCT, of course, but our primary motivation was to find out if the extreme delicacy of the material renders it particularly sensitive to dose rate. Knowledge and control of such effects would be important in obtaining reproducible annealing and dopant activation. Effects of the dose rate where the sample temperature is not allowed to rise during the implant are discussed in §4.3 along with experimental results. §4.3 also discusses the effects of damage rate and presents some experimental results on this topic. §4.4 summarizes this chapter.

4.2 Beam Heating

4.2.1 Background

During ion implantation a large amount of power may be delivered to the wafer, depending on the beam energy and dose rate. This results in a bulk temperature rise, the magnitude of which depends on the energy, the dose rate, the thermal conductivity of the wafer, and the thermal contact between the wafer and the holder. Very good thermal

contact between wafer and holder can be achieved with thermal bonding in which case only

two variables control the temperature rise for a given energy implant, dose rate and the

thermal conductivity of the wafer. Unfortunately, a practical method of thermal bonding

has not been developed for the high wafer throughput needed in a production situation

meaning that the case of imperfect thermal contact should also be considered. Note that for

poor thermal contact, not only will ΔT be greater, but it is also likely that the thermal

contact between wafer and holder will vary from spot to spot, resulting in different

temperature rises for each wafer or for regions of the same wafer. Such variations in ΔT

during the implant obviously lead to non-uniform residual damage and therefore non-

uniform electrical activity and post-implant annealing. This underlines the importance of

careful heat sinking which will be discussed more thoroughly below.

It has been assumed that MCT is very susceptible to beam heating because of its

low thermal conductivity, so implants have always been done at low current densities.

Though Destefanis [4.5] reports no variation in sheet carrier concentrations for boron

implant current densities ranging from 50 nA cm^{-2} to 3.5 μA cm^{-2}, Baars et al. found that

boron current densities higher than 1 μA cm^{-2} reduced the SEM electron current change

considerably and attributed the change to sample heating [4.6]. No doubt most of the

efforts to minimize the bulk temperature rise have been successful, or the material would

have been rendered useless from Hg loss, but the extremely low thermal conductivity of

MCT means that the transient temperature rise during the dwell time of the beam is a strong

function of the current density. Thus, even if the integrated temperature rise of the entire

wafer is not too great, the temperature at the surface directly under the beam might rise to

large values before the heat can diffuse away. This would increase the dynamic annealing

rate at that location, resulting in reduced residual damage. Previous calculations of ion

beam heating effects for other semiconductors as a function of current density have dealt

only with the bulk heating effect, [4.7] and have neglected the transient rise in temperature

that occurs directly under the beam. For this reason we have calculated the temperature under the beam versus time for MCT (x = 0.3) for various heat sink conditions to see if commonly used combinations of implant energy and current density lead to large transient temperature rises that could affect the final damage profile.

4.2.2 Beam Heating Model

4.2.2.A Assumptions and Equations

The geometry of the situation is shown in Fig. 4.1. Since the size of the ion beam is large compared to the sample thickness, a one-dimensional approach is used. We also consider the beam diameter to be comparable to the wafer size so that we can neglect lateral heat diffusion. This is accurate for our samples which are typically 5 x 5 mm^2 and implanted with a beam diameter of $\approx$ 1 cm. The equation to solve for the heat flow due to the ion beam is then the one-dimensional diffusion equation:

$$C_p = \frac{\partial T}{\partial t} = \nabla(\kappa \nabla T) + Q(z) \qquad (4\ 1)$$

where C_p is the heat capacity and κ the thermal conductivity of the semiconductor. $Q(z)$ describes the energy deposited as heat in the solid by the ion beam, taken to be electronic energy loss as a function of depth in the wafer. As discussed in Chapter 3, light ions give up a greater proportion of their energy to electronic stopping than heavy ions and thus have a greater heating effect. For example, BTE calculations show that for indium implanted into MCT, about 10% of the total implantation energy goes into electronic processes, whereas for boron about 90% of the total energy goes to electronic energy loss. For simplicity, the energy deposition profile for implanted particles is modeled by a Gaussian distribution with R_p and ΔR_p equal to that for the implanted ion profile. Note that this analysis can easily be extended to laser beams by calculating $Q(z)$ using the absorption coefficient as a function of depth. Because of the temperature dependencies of C_p and κ,

equation (1) is nonlinear. It is solved numerically using the three-time-level implicit

method [4.8] because of its suitability for nonlinear problems.
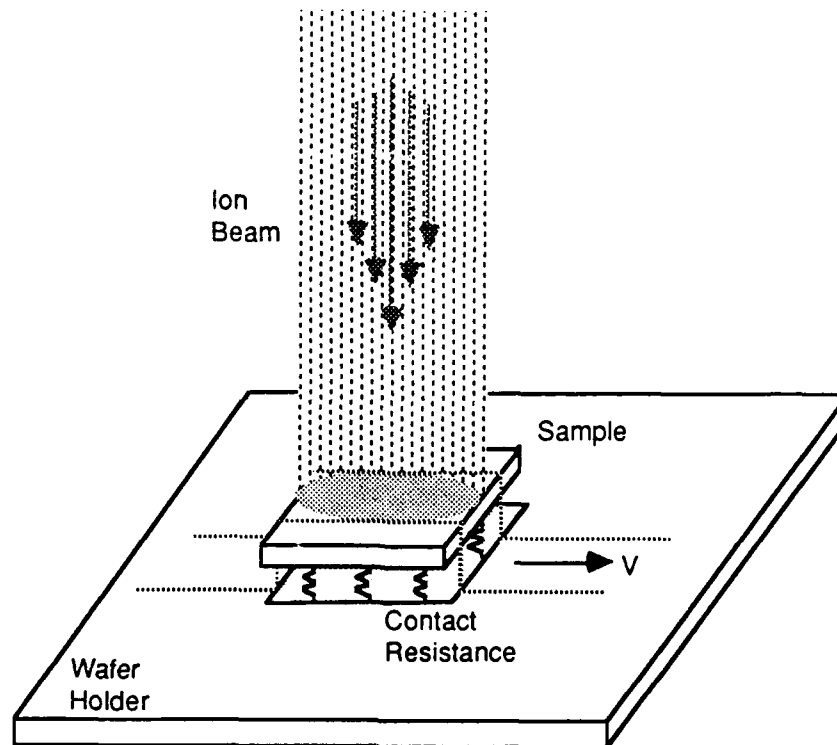
Fig. 4.1 Beam heating model geometry. A one-dimensional approach is used since the radius of the ion beam is large compared to the thickness of the wafer. We also assume that the sample is about the same size as the beam diameter so we can neglect lateral heat diffusion. The dwell time of the beam is on the order of 0.1 ms for typical scanning rates.

4.2.2.B Boundary Conditions

The boundary conditions for several cases are as follows:

a) Radiative Cooling

In this case the wafer is isolated from its surroundings except that it radiates

from both sides into a black body at ambient temperature. This is actually a good

approximation to reality unless some care is taken in heat sinking the sample. In a vacuum

the heat transfer out the front will be solely through radiation, and if the wafer is just

clipped to the holder, most of the heat transfer from the back surface will also be through

radiation because of the small number of points where the wafer end the holder actually touch. In such a case the power per unit area transferred between the wafer and the surroundings (P_r/A) from each side is given by:

$$\frac{P_r}{A} = \frac{\varepsilon_w \varepsilon_s}{\varepsilon_s + \varepsilon_w (1-\varepsilon_s)} \sigma (T_w^4 - T_s^4) \tag{4.2}$$

where ε_w and ε_s are the emissivities of the wafer and the surroundings, T_w and T_s are the temperatures of the wafer and the surroundings, and σ = Stefan-Boltzmann constant = $5.6703 \times 10^{-12} \frac{W}{cm^2 K^4}$. For illustrative purposes we take $\varepsilon_w = \varepsilon_s = 1$ making the boundary conditions:

$$\frac{\sigma}{\kappa(T)} [T_w^4 - T_s^4] = \frac{\partial T}{\partial z} (z = 0, t) \tag{4.3}$$

$$\frac{\sigma}{\kappa(T)} [T_w^4 - T_s^4] = - \frac{\partial T}{\partial z} (z = L, t) \tag{4.4}$$

Calculations show that the amount of power radiated is only significant when the sample temperature is several hundred degrees hotter than the ambient and steady state is not reached until the sample is quite hot. This means that the beam current/energy regime where radiative loss is dominant is unsuitable for MCT (since it must not be heated above 100° C) and these boundary conditions are not of interest for this material. We did use these boundary conditions for silicon, however, to compare our calculations with results in the literature. Those results will be discussed below.

b) <u>Perfect Heat Sinking</u>

Here we assume that the wafer is in perfect thermal contact with the holder. The back of the wafer is "clamped" at the holder temperature (T_{wh}) and the holder is a large thermal mass so its temperature is not affected by the heat coming from the sample. There are no losses out of the front surface. We could allow the front to radiate, but as we saw

above, the heat loss would be insignificant for the temperature regime we are interested in for MCT. The boundary conditions are thus:

$$\frac{\partial T}{\partial z}(z = 0, t) = 0 \tag{4.5}$$

$$T(z = L, t) = T_{wh} \tag{4.6}$$

c) Linear Heat Transfer

This case is the closest to reality when some effort at heat sinking has been made. As noted in case (a), unless special care is taken to heat sink the wafer, the heat conduction through the back side will be primarily through radiation. This is because the back of the wafer is microscopically rough so that the area of the wafer that is in actual physical contact with the wafer holder will only be a small fraction of the total wafer area. To improve heat conduction it is thus necessary to increase the contact area by methods such as using thermally conducting grease or by pressing the wafer into an elastic pad on the wafer holder.

We again assume that there are no radiation losses from the front surface, for the same reasons as in (b), but the heat transfer to the wafer holder, which is being maintained at the implantation temperature, is linear. The power lost through the back side of the wafer is thus proportional to the difference in temperature between the back of the wafer and the wafer holder making the boundary conditions:

$$\frac{\partial T}{\partial z}(z = 0, t) = 0 \tag{4.7}$$

$$H(T_w - T_{wh}) = \frac{\partial T}{\partial z}(z = L, t) \tag{4.8}$$

where H is the heat transfer coefficient in units of $\frac{W}{K}$. The value of H depends on the effective fractional contact area to the wafer (which will vary from run to run) and the thermal conductivity and thickness of the grease or pad. Only the thermal conductivity can

be known with any certainty which makes quantitative calculations very difficult. We can estimate typical values for H from searching the literature. Parry [4.7] fit experimental data on the ion beam induced temperature rise of silicon wafers to a model including linear heat transfer and found values for H of 0 to 8 mW/K for no thermal grease and 10 to 20 mW/K using grease. On closer examination, we see that (a) and (b) are merely limiting cases of (c) — for (a) H = 0 and for (b) H is large.

4.2.2.C Parameters for Silicon and MCT

a) Density and Specific Heat

For silicon we use constant values for the density, $\rho = 2.3 \frac{g}{cm^3}$, and the specific heat, $C_p' = 0.7 \frac{J}{gK}$ to obtain a volume specific heat $C_p = 0.91 \frac{J}{Kcm^3}$. For MCT (x = 0.3) we take values of the volume specific heat calculated by Holland [4.9]: $C_p = 1.187 + 0.3987T$ where T is in °C/1000. The density of MCT of this composition is $7.408 \frac{g}{cm^3}$.

b) Thermal Conductivity

The thermal conductivity of several semiconductors can be given by an expression of the form:

$$\kappa = \frac{A}{T-B} \frac{W}{cmK} \qquad (4.9)$$

where A and B can be fitted to experimental data. For silicon A = 299 and B = 99 [4.10]. Values calculated from this formula deviate from actual data less than 5% for temperatures greater than 300 K. Since calculations in this thesis for silicon are only done for implants at and above room temperature this expression is quite adequate for our purposes.

For MCT we combine diffusivity data from Holland [4.9] with the above values for the specific heat to obtain the thermal conductivity for a composition of x = 0.3:

$$\kappa_{MCT} = 0.01224 - 0.05112T + 0.1191T^2 - 0.05984T^3 - 0.03561T^4 \; \frac{W}{cmK} \quad (4.10)$$

where T is given in °C/1000. Though the diffusivity data was obtained over a temperature range of 150 to 900°C, extrapolating down to 77 K gives values for the thermal conductivity that agree well with low temperature measurements as shown in Fig. 4.2a. The solid lines are calculated from (4.10) and the points are values from the literature [4.11, 4.12]. For comparison, a plot of equation (4.9) for silicon is shown in Fig. 4.2b along with tabulated values [4.12].

4.2.3 Calculations

4.2.3.A Silicon - Comparison with Experiment

As a general check, we wanted to compare calculations of the implantation-induced temperature rise in silicon to experimental results in the literature. It was difficult, however, to find an experimental configuration that corresponded exactly to our case, since most reported results concern the temperature rise of the entire wafer due to a rapidly scanned beam. Even if the temperature rise as a function of implant time is reported, the fact that the scanned beam is much smaller than the wafer means those results can not be meaningfully compared to our calculations because the heat will diffuse laterally, causing the measured temperature under the beam to be lower. We thus chose the next best option and compared Parry's values for the measured equilibrium temperature as a function of incident power density [4.7] to our calculations of the equilibrium temperature that would be reached under a stationary beam. The current density in our calculations is the actual current density of the beam and we assume the sample is comparable in size to the beam. The current (power) density quoted by Parry is the beam current (power) divided by the total scanned area, so the two cases are equivalent in equilibrium. We find that with the boundary conditions for case (a) above, we can fit Parry's results for H=0 (radiation losses only) using reasonable values for wafer temperature and emissivity. The parameters that correspond to the best fit for our calculations are slightly different than those that Parry calculates to fit his model, but that is not surprising considering that he assumes a constant
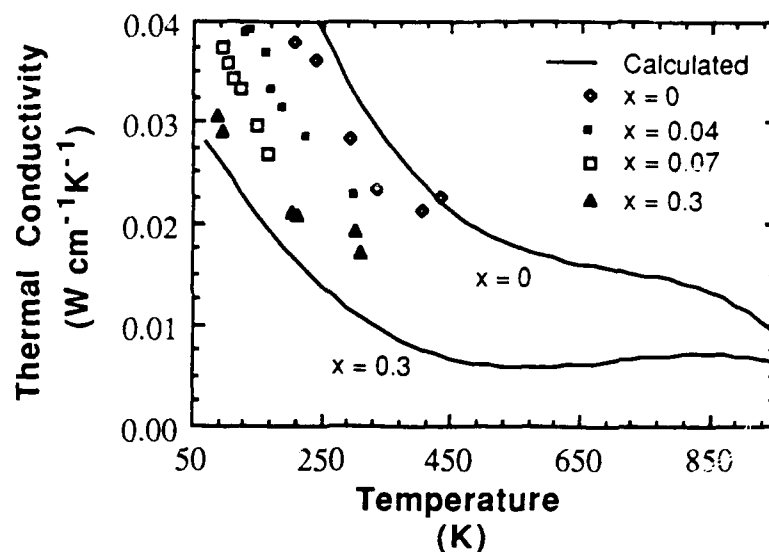
Fig. 4.2 (a) Thermal conductivity as a function of temperature for MCT compositions ranging from x = 0 to x = 0.3. The solid lines are calculated from (4.10), the solid triangles are from [4.11] and the remaining points come from [4.12].
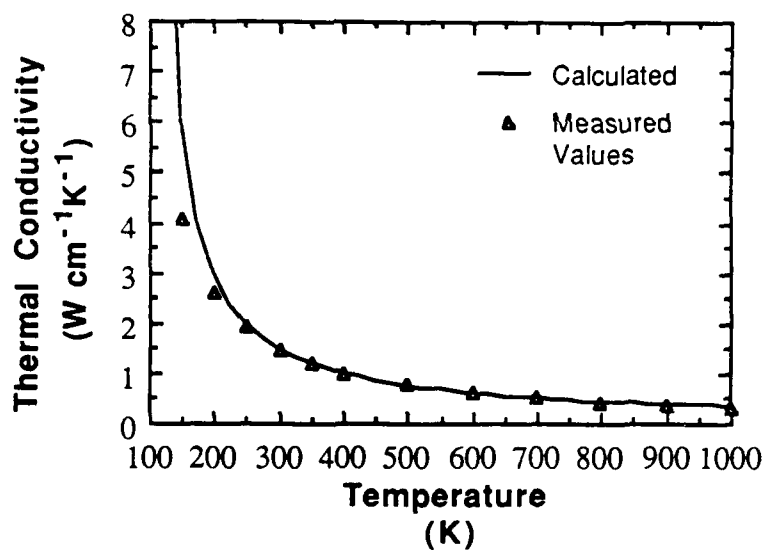
Fig. 4.2 (b) Thermal conductivity as a function of temperature for silicon. The solid line is calculated from (4.9) and the points are from [4.12].

heat capacity and that the temperature the wafer "sees" from its surroundings is a parameter

in both models. Since our calculations for silicon agree reasonably well with experiment,

we can proceed to calculate beam heating in MCT.

4.2.3.B MCT

a) Transient Temperature Rise Calculations

Calculations of the temperature rise versus time under the beam are shown in Fig.

4.3 for case (b), a perfectly heat-sunk sample, for 300 keV ions implanted at 77 K and

room temperature at two different current densities, $0.1~\mu A~cm^{-2}$ and a $1~\mu A~cm^{-2}$. These

values for current density correspond to the conventional definition in which the beam

current is divided by the entire area scanned by the beam. If we assume an overscan of

about three beam diameters [4.1] in an implanter designed for 2 inch wafers and a beam

diameter of 1 cm, we find that the scanned area is $122.8~cm^2$ and the actual beam current

densities are 15.63 and $156.3~\mu A~cm^{-2}$. For typical scan rates, the dwell time of the beam

is on the order of 0.1 ms, leading to a transient temperature rise for the higher current of

less than 5 C° for a room temperature implant and, since thermal conductivity increases

with decreasing temperature, only 3 C° for a 77 K implant. The temperature rise for the
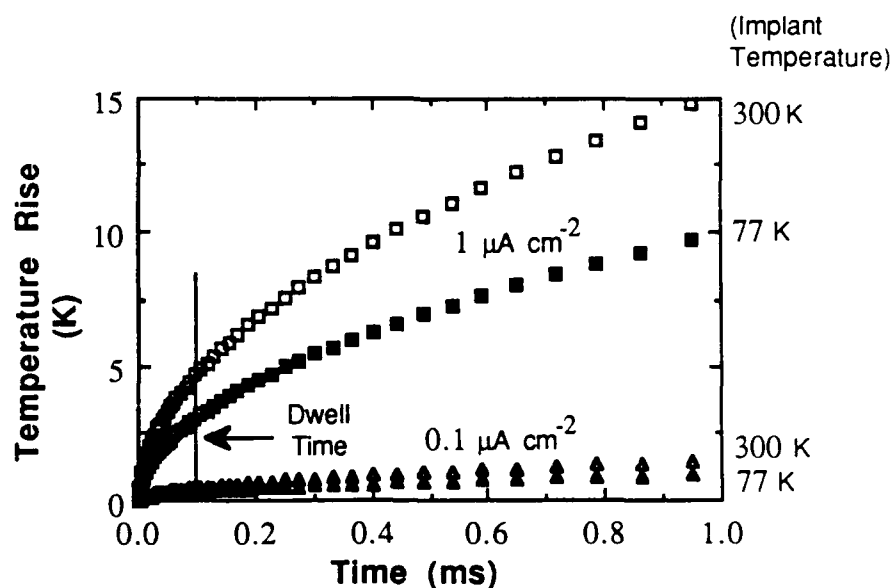
Fig. 4.3 Calculated transient temperature rise during the dwell time of the beam for a perfectly heat sunk sample. Implant conditions: energy = 300 keV, temperature = 77 K and room temperature, beam current = $1~\mu A~cm^{-2}$ and $0.1~\mu A~cm^{-2}$, and sample thickness = 1 mm. The transient temperature rise is small for even the highest beam current, indicating that the temperature rise should not be a problem for conservative implant conditions.

lower beam current is less than 1 C° for both implant temperatures. The corresponding temperature rise in silicon would be less than 0.4 C° for all of the conditions considered.

Our calculations show that the main effect of imperfect heat sinking (small H) is to increase the equilibrium temperature and the time needed to reach the steady state, but that the magnitude of the temperature rise under the beam during its dwell time is not affected. This is fortunate as the value for the heat transfer coefficient depends on exactly how the irregularities in the surfaces of the wafer and the holder juxtapose and is very difficult to predict. Thus we show no calculations for the boundary conditions of case (c). The equilibrium temperature mentioned above is the steady state temperature reached under a stationary beam and takes neither the "off time" of the beam (typically 100 x the dwell time over each spot) nor lateral heat diffusion into account. In addition, unlike the calculations for silicon in §4.2.3.A, we assume no radiation losses, so the calculated steady state temperature is far higher than the temperature that would be reached in an actual implant.

It is clear that the efforts to keep the equilibrium temperature rise due to implantation low have been successful. since otherwise Hg loss would render the samples unusable. We can thus assume that the maximum equilibrium temperature during room temperature implants is on the order of 375 - 400 K for which we calculate a maximum transient temperature rise of just over 5 C° with a 1 μA cm^{-2} beam. Since a current density of 1 μA cm^{-2} is on the high end of the values quoted in the literature [4.5, 4.6, 4.13, 4.14] we can see that the transient temperature rise should not be a problem for conservative implant conditions.

b) Highest Allowable Beam Current

We will now calculate the current that leads to the maximum allowable transient temperature rise. As a worst case estimate, we assume that the sample has already been heated by the beam to its maximum permissible equilibrium temperature of 400 K. If we

take the maximum allowable transient temperature rise to be an additional 10 C°, we get a maximum beam current of 225 μA in our calculations which translates to a current density of 1.8 μA cm^{-2} in conventional terminology. Thus, even though beam currents $\geq$ 1.8 μA cm^{-2} may not cause an obvious bulk temperature rise (as measured by sample deterioration) [4.5], unless one is prepared to accept an additional transient temperature rise of $\geq$ 10 C°, this current should not be exceeded. There is evidence that such a transient temperature rise may cause measureable effects since Baars *et al.* found that boron current densities higher than 1 μA cm^{-2} reduced the SEM electron current change considerably and attributed the change to sample heating [4.6].

c) Effects of Poor Heat Sinking

To check for a bulk (equilibrium) temperature rise due to beam heating we implanted some samples at both 77 K and room temperature (300 keV In, 3 x 10^{14} cm^{-2}) with deliberately poor thermal contact between the MCT and the wafer holder. As described in §3.5.3.D, rather than being carefully heat sunk with thermal grease, these two implants were carried out with the sample lightly clipped onto the sample holder. The beam current was quite low, $\leq$ 0.05 μA cm^{-2}, in conventional units. The differences in the channeling spectra for the well heat sunk and the poorly heat sunk samples can be seen by referring to Figs. 3.16a and b. Obviously, some beam heating occurs for the cold implants since the residual damage profile for the poorly heat sunk sample is significantly reduced from that of the well heat sunk sample. We might expect a similar temperature rise for the sample implanted at room temperature, but the channeling spectra show no difference in residual damage between well and poorly heat sunk samples. This indicates that residual damage from room temperature implants is much less sensitive to moderate, beam-induced temperature rises, probably because the defect mobility is already so high that the additional mobility increase is negligible in comparison.

It is difficult to calculate the actual beam-induced temperature rise because the heat transfer coefficient can only be estimated. Parry's values for the heat transfer coefficient for implants using no thermal grease ranged from 0 to 8 mW/K. Using the intermediate values of 4 mW/K and 3 mW/K, we calculate an equilibrium temperature rise of $\approx$ 60 K and $\approx$ 80 K, respectively for both temperature implants. In this case we need not worry about lateral heat diffusion since the 5 x 5 mm^2 samples were smaller than the beam diameter of $\approx$ 1 cm. This magnitude of temperature rise is consistent with channeling results from both cold and room temperature implants, from which maximum and minimum values of ΔT can be deduced. For the room temperature implant, if the actual temperature rise were much greater than 80 K we might expect enhanced *in situ* annealing or some Hg loss, neither of which are observed in the RBS spectra. For the cold implant it would be difficult to explain the reduced damage level with a temperature rise much less than 60 K because such a moderate temperature rise should not cause that large an increase in defect mobility, even with the beam-enhanced regrowth discussed in Chapter 3. A comparison of the channeling spectrum for the poorly heat sunk 77 K implant with channeling spectra from 100 keV In implanted to a dose of 5 x 10^{14} cm^{-2} at 170 K (well heat sunk) [4.15] provides additional evidence that the beam induced temperature rise is probably nearer 80 K (or equivalently that the implantation temperature is $\approx$ 150-160 K). A channeling spectrum from the latter implant is shown in Fig. 4.4, where we see that the damage profile in the Hg sublattice for the 170 K implant is very similar to that of the poorly heat sunk 77 K implant. Both have a sharp damage peak at the surface and then decrease in height until the energy of the Te edge is reached. We attribute the slightly narrower surface peak and lower damage level deep in the sample for the 170 K implant to the combination of a slightly higher implant temperature (more *in situ* annealing) and a lower energy implant (less damage in the first place).
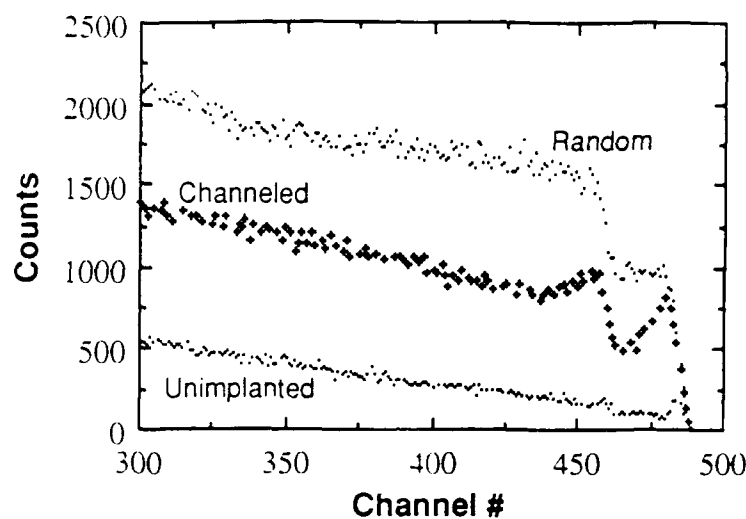
Fig. 4.4 Random and channeling RBS spectra for 100 keV indium implanted to a dose of 5×10^{14} cm^{-2} at 170 K. The damage profile in the Hg sublattice is very similar to that for the poorly heat sunk 77 K implant shown in Fig. 3.16a. This is strong evidence that the beam induced temperature rise in the poorly heat sunk sample increases the actual implant temperature from 77 K to 150 - 160 K.

d) Temperature Rise During RBS

As a further test of the model, we calculated the temperature rise experienced by a sample during RBS or channeling analysis. Again we want to calculate the steady state temperature rise, since analysis typically takes 30-45 minutes. For MCT we use a 2 nA beam with an area of approximately 1 mm^2 which gives us a current density of ≈ 0.2 µA cm^{-2}. At our beam energy of 2.2 MeV, we calculate the equilibrium temperature with perfect heat sinking to be ≈ 304 K. Samples mounted for RBS analysis are typically not in good thermal contact with the goniometer, however, so we calculated the equilibrium temperature using linear heat transfer boundary conditions as well. For an intermediate value of H = 4 mW/K we then calculate the steady state temperature to be ≈ 327 K. Since the He$^+$ beam in RBS is significantly smaller than the sample area, heat will also diffuse away laterally and reduce the steady state temperature. This is not taken into account in the model, so the equilibrium temperature that we calculate is a maximum value. A temperature

rise of ≈ 25 K during RBS is not unreasonable and it is further evidence that our model gives plausible results.

4.3 Rate Effects

4.3.1 Introduction

In the model of Morehead and Crowder [4.16] an incident ion creates a highly disordered zone consisting of a vacancy-rich core surrounded by an interstitial-rich periphery. During a time τ on the order of 10^{-9} s after the passage of the ion, the displaced atoms reform bonds and change their positions while vacancies diffuse thermally out of the core into the periphery. The outer sheath thus dynamically anneals to form less damaged material, and the part of the core that still has "excess" vacancies forms a stable amorphous phase. Of course the regrown outer sheath, though it is crystalline, will have a higher defect density than the unimplanted crystal. The final size of the amorphous region depends both on the original volume of the collision cascade and on how many vacancies are able to escape during the time τ. The important parameters for a given ion/target combination are thus the rate at which energy is lost to nuclear stopping, the target temperature, and the dose rate. Nuclear stopping determines the initial size and density of the collision cascade and the temperature determines the vacancy mobility. Dose rate is important because if it is high enough collision cascades will begin to approach each other during the period of time in which vacancies are still escaping from the core. This increase in the steady state concentration of vacancies will retard the outdiffusion of vacancies from within zones, causing the final size of the amorphous region to be larger. In addition, the impingement of collision cascades during the time τ may interfere with the rearrangement of the displaced target atoms in the outer sheath so that the regrown crystal has a higher damage density than it would for a lower dose rate.

4.3.2 Dose Rate Experiment

To see if we could find any variation in residual damage due to dose rate we implanted 300 keV [115]In into MCT (x = 0.3) at 77 K and room temperature to a dose of 3 x 10^{14} cm^{-2} at two current densities. We chose to implant a heavy ion since the larger, higher density collision cascades are expected to cause dose rate effects at lower current levels than would those due to a light ion. Our low level current was 0.2 μA, but unfortunately the highest current we could get out of the implanter was only 5 μA. For an estimated beam diameter of 1 cm, these currents correspond to 0.25 μA cm^{-2} and 6.4 μA cm^{-2}. The samples were carefully heat sunk with thermal compound to minimize beam heating effects. Calculations done for a perfectly heat sunk sample show a maximum equilibrium temperature rise of 18 C° for the higher current implant. Since the calculation is for a stationary rather than a scanned beam, this is an absolute maximum estimate. It is unlikely that a temperature rise of only 18 C° would have appreciable effects on damage annealing, so we can be confident that beam heating has not affected our results.

RBS spectra taken on the samples are shown in Fig. 4.5. We observe no difference in the 170° spectra for the different current implants, indicating no difference in damage for the currents used at either room temperature or 77 K. This is really not all that surprising considering that the highest current we could get out of our implanter was only 5 μA. This current corresponds to ≈ 4 x $10^{19} \frac{ions}{s\ cm^2}$. Assuming the region around the disordered core forms a stable phase in a time τ on the order of 10^{-9} s [4.16], the distance between ions impinging within τ is ≈ 500 Å. This is a fairly large separation between cascades to expect them to interfere with each other, but if we could have increased the current by a factor of 10, the distance between cascades would have been ≈ 150 Å which is much closer to the size of the fairly large collision cascades that implanted indium should cause. Such a dose rate would correspond to a beam current of ≈ 0.5 μA cm^{-2} or just half

the current that we used in our beam heating calculations in §4.2.3.B. Thus we should be able to perform such an experiment without interference from beam heating, assuming we heat sink the sample carefully.
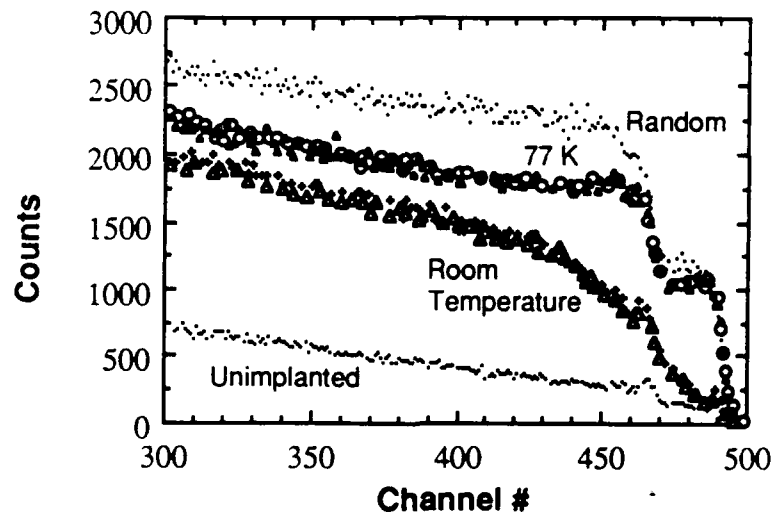
Fig. 4.5 Random and channeling RBS spectra for indium implants at "low" and "high" beam currents. Implant conditions: energy = 300 keV, temperature = 77 K and room temperature, beam current = 0.2 µA and 5 µA. The distance between the centers of the collision cascades in a 1 ns time period is calculated to be 500 Å for the highest current obtainable from the implanter. This is too great a separation to expect to expect much overlapping and indeed, there is no difference in the channeling spectra from the low and high current implants at either implant temperature.

4.3.3 Damage Rate Experiment

We did another experiment that very clearly illustrates the importance of the damage rate in determining the residual implant damage. What we mean by damage rate is the amount of energy a single ion deposits into nuclear processes divided by the path length of the ion *ie*. the energy density deposited into nuclear stopping. Obviously this depends on both nuclear stopping and ion range and consequently is a function of the ion mass and the energy of implantation. It has been shown experimentally that disorder production is proportional to the energy density deposited into nuclear events in other materials [4.17]. To look for this effect in MCT, we implanted ^{11}B, ^{19}F, and ^{20}Ne into MCT samples at 77 K, choosing the energy and dose of each ion so that the total nuclear damage as calculated

by TRIM was about the same. Table 4.1 shows the parameters and calculated nuclear damage for each implant. Since the integrated nuclear damage is the same, the same number of target atoms are displaced by each implant. It would thus seem logical that the height of the backscattering yield from channeling measurements would be about the same for all the implants, but is clear from the RBS data shown in Fig. 4.6 that the heights of the spectra differ significantly. This means that for some reason the amount of dynamic

Table 4.1 CALCULATED NUCLEAR DAMAGE AND DEPOSITED ENERGY DENSITY FOR FIG. 4.6

Ion	Energy (keV)	Nuclear Damage (keV ion^{-1})	Dose (ions cm^{-2})	Total Nuclear Damage (keV cm^{-2})	Deposited Energy Density (keV ion^{-1} cm^{-1})
B	250	32.9	1×10^{14}	3.3×10^{15}	6.9×10^{5}
Ne	180	70.8	5×10^{13}	3.5×10^{15}	3.1×10^{6}
F	350	85.8	3.8×10^{13}	3.3×10^{15}	2.0×10^{6}
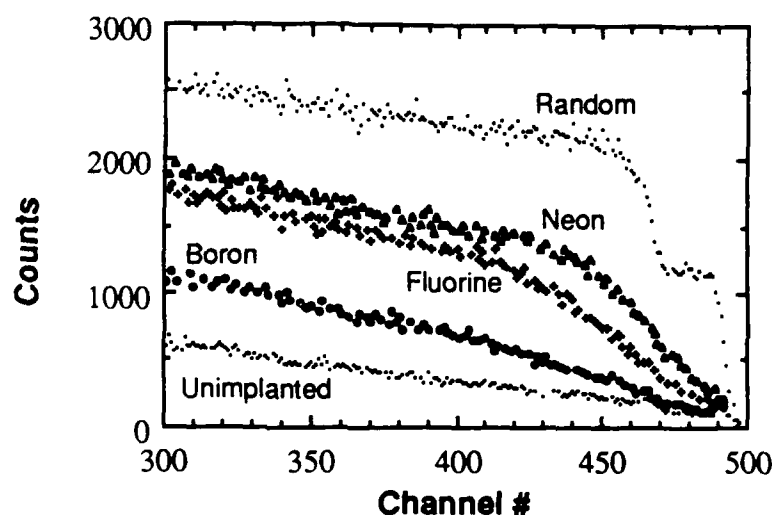
Fig. 4.6 Illustration of the sensitivity of the residual damage in MCT to the density of the collision cascade. The energy and dose of each ion was chosen so that the total energy deposited into nuclear stopping as calculated by TRIM would be the same for each implant (shown in Table 4.1) and thus the same number of lattice displacements would occur in each sample. The channeling spectra, however, do not show identical levels of residual damage in the samples, indicating that the density of the collision cascades produced by each ion affect the extent to which the MCT is able to self-anneal during an implant.

annealing varies between the different implants. We can see what is happening by referring again to Table 4.1. Though the total nuclear damage is about the same for each implant, when we divide the nuclear damage per ion by the projected range to get the deposited energy densities, they vary considerably. The long range of the boron ions, combined with a fairly low amount of nuclear damage per ion give it the lowest damage rate. Fluorine has a slightly shorter range and displaces more target atoms per ion, giving it a damage rate more than twice that for boron. The low energy of the neon implant gives it the shortest range, but it also displaces fewer atoms per ion than fluorine. The net result is that the calculated damage rate is only slightly greater than that for fluorine. As the density of each collision cascade increases, the crystalline perfection of the material that is able to regrow around the highly disordered core is reduced, increasing the residual damage. The residual damage should thus be the least for boron with the damage for fluorine being significantly higher and the damage for neon being just slightly greater than that for fluorine. These predictions are reflected exactly in Fig. 4.6. These results show that a damage rate effect is easily observable in MCT.

4.4 Summary

In this chapter we have investigated the effects of beam current and damage rate on residual damage in MCT and compared calculations with experiment. Calculations for implants into MCT ($x = 0.3$) indicate that for conservative implant conditions (beam currents < 1 μA cm^{-2}, well heat sunk sample) the transient temperature rise under the beam is not large enough to affect the residual damage profile. Experimental results do indicate, however, that a beam-induced temperature rise does occur in samples in poor thermal contact with the wafer holder even for low beam currents. For samples nominally implanted at 77 K the resulting increase in defect mobility, in combination with beam-enhanced effects, is enough to significantly reduce the residual damage. For samples implanted at room temperature, however, the defect mobility is already so high that the

residual damage is not affected. Ion channeling results also indicate that, as in other materials, residual damage in MCT is highly dependent on the energy density deposited into nuclear stopping, and thus on the density of the collision cascade.

4.5 References

[4.1]   H. Ryssel and I. Ruge, *Ion Implantation*, Wiley, New York, 1986.

[4.2]   M. King, P.H. Rose, Nucl. Inst. Meth. **189**, 169 (1981).

[4.3]   F.H. Eisen and B. Welch, Rad. Effects **7**, 143 (1971).

[4.4]   N.A.G. Ahmed, C.E. Christodoulides, G. Carter, M.J. Nobes, and A.I. Titov, Nuc. Inst. and Method. **168**, 283 (1980).

[4.5]   G.L. Destefanis, Nucl. Inst. and Meth. **209/210**, 567 (1983).

[4.6]   J. Baars, A. Hurrle, W. Rothemund, C.R. Fritzsche, and T. Jakobus, J. Appl. Phys. **53**(3), 1461 (1982).

[4.7]   P.D. Parry, J. Vac. Sci. Technol., **13**(2), 622 (1976).

[4.8]   A.R. Mitchell, *Computational Methods in Partial Differential Equations*, Wiley, New York, 1969.

[4.9]   L.R. Holland and R.E. Taylor, J. Vac. Sci. Technol. A **1**, 1615 (1983).

[4.10] A. Lietoila, Laser Processing of High Dose Ion Implanted Si: The Solid Phase Regime, Ph.D. Thesis, Stanford University, August 1981.

[4.11] S.A. Aliev, T.G. Gadzhiev, E.M. Aliev, D.G. Arasly, and M.I. Aliev, Sov. Phys. Semi., **5**(12), 2044 (1972).

[4.12] Y.S. Touloukian, R.W. Powell, C.Y. Ho, and P.G. Klemens, *Thermophysical Properties of Matter* Vol. 1, *Thermal Conductivity: Metallic Elements and Alloys*, 1407, IFI/Plenum, New York, 1970.

[4.13] P.G. Pitcher, P.L.F. Hemment, Q.V. Davis, Elec. Lett., **18**(25), 1090 (1982).

[4.14] R. Kalish, R. Fastow, V. Richter, and M. Shaanan, Appl. Phys. Lett. **51**(15), 1158 (1987).

[4.15] H.L. Dunlap, K.V. Vaidyanathan, L.K. Magel, T.W. Sigmon, and C.Y. Huang, presented at EMC, Boulder, Colorado (1985).

[4.16] F.F. Morehead, Jr. and B.L. Crowder, Rad. Eff. **6**, 27 (1970).

[4.17] S.T. Picraux and F.L. Vook, Rad. Eff. **11**, 179 (1971).

Chapter 5

Implantation and Annealing

5.1 Introduction

Ion implantation is a promising method of forming n^+-p junctions in MCT [5.1], but it is still a poorly understood process in this material. As-implanted samples always exhibit n-type conductivity independent of the implanted ion or the carrier type of the substrate and the junction is located deeper than the atomic profile of the implanted impurity. Type conversion is thus attributed to damage from the implant rather than activation of the dopant. Devices with excellent characteristics have been made by intentionally not annealing this radiation damage, but a true activated dopant would have several advantages over defect doping, including precise control of doping concentration profiles and accurate prediction of junction position. In addition, repair of the radiation damage should increase stability to temperature cycling and reduce noise sources.

The primary reason workers resorted to using as-implanted junctions in the first place is the difficulty of annealing MCT without losing Hg. Because of the weakness of the Hg-Te bond, uncapped MCT held at only 200° C will lose a monolayer of Hg in less than two minutes [5.2]. Longer times and higher temperatures are required to repair lattice damage and activate the implanted dopant so it is clear that some method of preventing Hg loss during annealing must be developed. Encapsulation prevents As loss in post-implant annealing of GaAs so workers have applied this approach to MCT. One particularly promising encapsulant is a photochemical native oxide. A multiple step anneal using this oxide as a cap has recently been reported to both repair implant damage and partially activate implanted boron without Hg loss [5.3, 5.4]. Another common method of reducing Hg loss is to anneal the implanted material in a Hg overpressure.

It is generally accepted that implanted indium can be at least partially activated using either encapsulation or an Hg atmosphere, but the results for boron remian controversial. Some groups report partial activation of implanted boron after annealing [5.3 – 5.5], as mentioned just above, but others find no activation of boron in samples annealed under vacuum or Hg overpressure at temperatures up to 500° C [5.6, 5.7]. The activation of indium atoms was established by comparison with the behavior of xenon-implanted samples where the electrical activity is solely due to implant damage and disappears when the samples are annealed between 200 and 250° C, presumably as the damage is repaired. In this work we performed a similar experiment to finally resolve the controversy about boron activation.

In this chapter we study the changes in crystal quality and electrical parameters of layers implanted with different ions as they go through a multiple step annealing sequence. The ions studied and implant conditions are: ^{11}B (250 keV, 1 x 10^{14} cm^{-2}, implanted at 77 K and room temperature), ^{19}F (350 keV, 3.8 x 10^{13} cm^{-2}, 77 K), ^{20}Ne (180 keV, 5 x 10^{13} cm^{-2}, 77 K) and ^{115}In (300 keV, 6 x 10^{12} cm^{-2}, 77 K). From their positions on the periodic table, shown in Fig. 5.1, or from previous experimental results, boron and indium are expected to be donors, substituting on the metal sublattice, neon is expected to be inert, and fluorine is expected to be a donor substituting on the Te sublattice. To make the annealing studies easier to compare, the energies and doses of the B, F, and Ne implants are chosen to create similar amounts of damage in the as-implanted samples. Comparing the results of the annealed neon- and boron-implanted samples will then reveal whether boron is being activated or if the observed n-type activity is merely due to incompletely annealed damage.

In §5.2 we briefly discuss the oxide growth and annealing process for the implanted samples which is the same as that in [5.3, 5.4]. Studies of the repair of implant

damage as a function of annealing step, done using RBS and MeV ion channeling, are presented in §5.3. In this section we also relate these structural results to electrical properties of the samples measured using the van der Pauw technique and discuss the activation of the four types of implanted ions. The effects of implantation and annealing on near band gap states and radiative transitions between these states, studied using photoluminescence spectroscopy, is discussed in §5.4. Finally, the movement of the implanted ions in response to annealing was measured using SIMS and the results are discussed in §5.5. The chapter is summarized in §5.6.

Donors on Metal Sites		Acceptors on Te Sites		Donors on Te Sites		
5 B	6 C	7 N	8 O	9 F	10 Ne	
13 Al	14 Si	15 P	16 S	17 Cl	18 Ar	

Acceptors on Metal Sites

29 Cu	30 Zn	31 Ga	32 Ge	33 As	34 Se	35 Br	36 Kr
47 Ag	48 Cd	49 In	50 Sn	51 Sb	52 Te	53 I	54 Xe
79 Au	80 Hg	81 Ti	82 Pb	83 Bi			

Fig. 5.1 A portion of the periodic table illustrating the expected doping behavior of various impurities in MCT. Boron and indium are expected to substitute on the metal sublattice and be donors, neon should be inert, and fluorine should substitute on the tellurium sublattice and be a donor.

5.2 Oxide Growth

5.2.1 Description of Growth Mechanism

More detailed discussions of oxide growth mechanisms are available in [5.4, 5.8, 5.9]. Since this thesis is only concerned with using the native oxide as an encapsulant rather than with studying the oxide itself, only the highlights will be given here. Samples are prepared and implanted as described in §2.1 and a thin native oxide layer is photochemically grown on each sample to serve as an encapsulant. This oxide layer is grown by illuminating the MCT in either an O_2 ("ozone oxide") or an N_2O ("nitrous oxide") ambient with a low-pressure Hg lamp. Such lamps emit light at wavelengths extending from 185 to over 600 nm and the 185 and 254 nm lines are efficient at producing electronically excited oxygen, a strong oxidizing agent. It is believed that the oxidation process includes both oxygen in-diffusion and substrate element out-diffusion in both ambients though the migration mechanisms for the two ambients could differ. During the oxidation the sample temperature reaches $\approx$ 40-50° C because of its proximity to the lamp.

The growth rate for the nitrous oxide is at least an order of magnitude faster than for the ozone oxide, but the result is a more porous oxide with more defects. These defects can work as pipes for Hg loss, making this oxide less suitable as a cap for higher temperature annealing steps. As with previous studies of photochemical [5.10] and anodic oxides [5.11], both types of oxide are unstable with MCT at elevated temperatures, resulting in oxide stoichiometry changes during annealing. Several reactions occur at the surface with the net result being excess Cd (or $CdTeO_3$) in the oxide. The empty Cd sites in the MCT are filled by Hg atoms either released from the oxide or out-diffusing from deeper in the MCT and the resulting Hg gradient at the surface presents a barrier to further Hg movement. Thus though the interface instability presents problems to workers wishing to use a native oxide as a passivation layer in devices, it can be used to advantage when the

oxide is used as an encapsulant. After annealing the oxide layer can be removed with a dilute HCl or lactic acid etch.

5.2.2 Growth and Annealing Sequence

The sequence of oxide growths and annealing steps following implantation is as follows: Immediately before being placed into the growth chamber the sample is dipped into a Br_2-methanol solution to remove any already existing surface oxide and rinsed thoroughly in methanol. The sample is then placed into the growth chamber and the chamber is purged with oxygen for a few minutes before the Hg lamp is turned on. After five to seven days in the chamber the oxide is ≈ 200 Å thick and the samples are ready for the first annealing step, a 200° C furnace anneal in flowing N_2. Following this anneal, which lasts between four and ten hours, the oxide is a darker golden color than immediately following oxide growth, indicating reactions between the oxide and MCT have occurred. We feel that, as well as partially repairing implant damage, this anneal is important in stabilizing the oxide/MCT interface in preparation for the higher temperature thermal pulse anneal. The samples next undergo a four to five minute thermal pulse anneal at 320° C in an argon ambient of just below one atmosphere. No visible change in the samples is evident after this step. Typically the oxide is removed at this point and the sample is etched back by about 100 Å. A nitrous oxide is then grown in preparation for the third annealing step, another 200° C furnace anneal in flowing N_2. The oxide is regrown for several reasons. The high temperature anneal might degrade the original oxide which would permit Hg or dopant loss during the final anneal. Also, the ozone oxide growth (but not nitrous oxide growth) results in a Hg-rich layer just inside the MCT. This Hg-rich layer has been shown to reduce boron activation unless it is removed [5.4]. Finally, since it is possible that Hg interstitials are donors, we felt it best to remove the Hg-rich layer to reduce confusion about the source of any n-type doping in annealed samples.

5.3 Structural and Electrical Properties as a Function of Annealing Step

5.3.1 Anneal 1

To study the repair of implantation damage we examined samples implanted under different conditions following each annealing step. Fig. 5.2 shows the spectra resulting from channeling studies of samples implanted with 300 keV, 10^{13} cm^{-2} indium at 77 K and annealed at 200° C for five, nine, and thirty hours. The five hour anneal removes the point defects and completely repairs the damage for roughly the first 900 Å since the backscattering yield is the same as that for the unimplanted sample. The yield starts to rise, however, beyond a depth of 900-1000 Å in the manner characteristic of extended defects. Either the point defects anneal to form extended defects or they anneal away completely to reveal dislocations and loops that were also formed during the implant. Annealing for nine hours continues to decrease the backscattered yield, but is still not sufficient to return the crystal to its original defect density. Since a sample annealed for thirty hours shows no
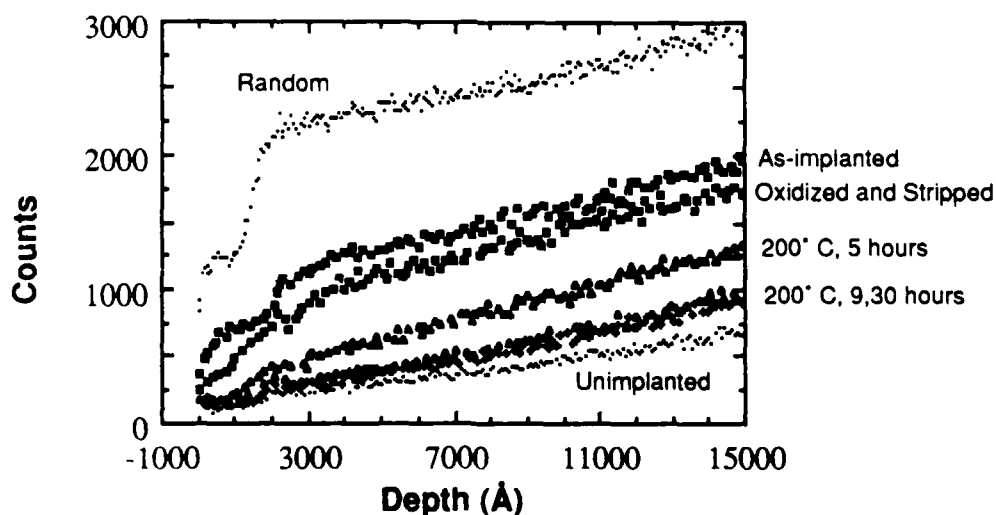
Fig. 5.2 Channeling study of the repair of damage due to an indium implant as a function of time during Anneal 1. Implant conditions: energy = 300 keV, temperature = 77 K, dose = 10^{13} cm^{-2}. Annealing conditions: temperature = 200° C for 5, 9, or 30 hours. A five hour anneal repairs the damage near the surface, but leaves many extended defects beyond a depth of ≈ 1000 Å. A nine hour anneal is sufficient to "fully" anneal the material at 200° C. Channeling measurements on a sample that was oxidized but not annealed show that the complete repair of the near surface damage is indeed due to annealing.

improvement over the nine hour anneal, nine hours at 200° C is sufficient to repair everything that can be repaired at that temperature. The slopes of both the nine and the thirty hour anneals are constant throughout the sampled region, indicating a fairly uniform distribution of extended defects that is only slightly greater than in the unimplanted crystal. The low damage level at the surface is consistent with TEM results for 100 keV 10^{14} cm^{-2} Hg annealed at 200° C in which the near surface is free of visible defects and the remaining damage has reorganized into loops [5.12].

It occurred to us that since the indium implant is so shallow, we might be removing a significant portion of the damaged region during the oxidation step. This would cause us to overestimate the degree of annealing. To see just how large an effect this is we oxidized one sample and stripped off the oxide without annealing. The resulting channeling spectrum is also displayed in Fig. 5.2. Obviously, removing the top 150-200 Å does reduce the damage level, but the sample still shows the heavy surface damage characteristic of point defects. The effect on the damage level for lighter ions would be even less since the damage in those cases is deeper.

It is interesting to compare isothermal annealing results for indium to those for 250 keV, 10^{15} cm^{-2} boron implanted at 77 K which are shown in Fig. 5.3 (data taken by T.-M. Kao). For this boron implant a five hour anneal is sufficient for "complete" annealing at 200° C whereas nine hours is required for indium. Though the indium implants appear to have annealed more fully, we feel this is due to beginning substrate quality rather than a difference in implant damage structure, as discussed below.

Additional annealing results for fluorine, neon, and boron are shown in Fig. 5.4. The as-implanted damage levels vary considerably for the different implants (see Fig. 4.7), but after annealing, the channeling yields are quite similar and only slightly higher than the unimplanted crystal. Comparison of this figure to Fig. 5.2 show that these same spectra

Depth from Hg Edge (μm)
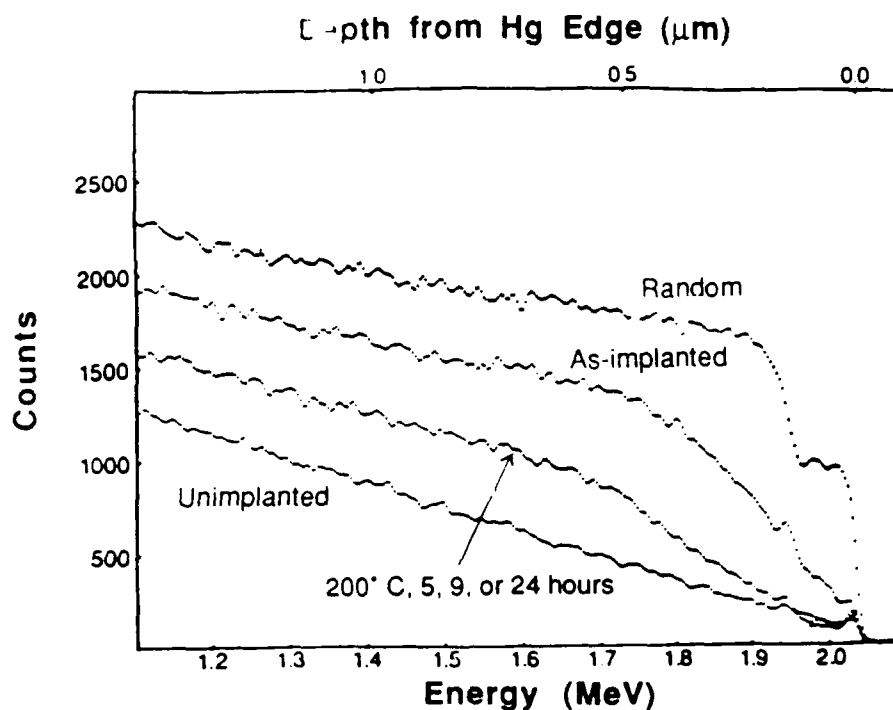
Fig. 5.3 Channeling study of the repair of damage due to a boron implant as a function of time during Anneal 1. (adapted from [5.4]) Implant conditions: energy = 250 keV, temperature = 77 K, dose = 10^{15} cm^{-2}. Annealing conditions: 200° C for 5, 9, or 24 hours. As compared to Fig. 5.1, "complete" annealing takes less time for the lower mass implant. The higher level of damage in the "fully" annealed boron-implanted sample is probably due to poorer substrate quality rather than a difference in annealing as discussed in the text.
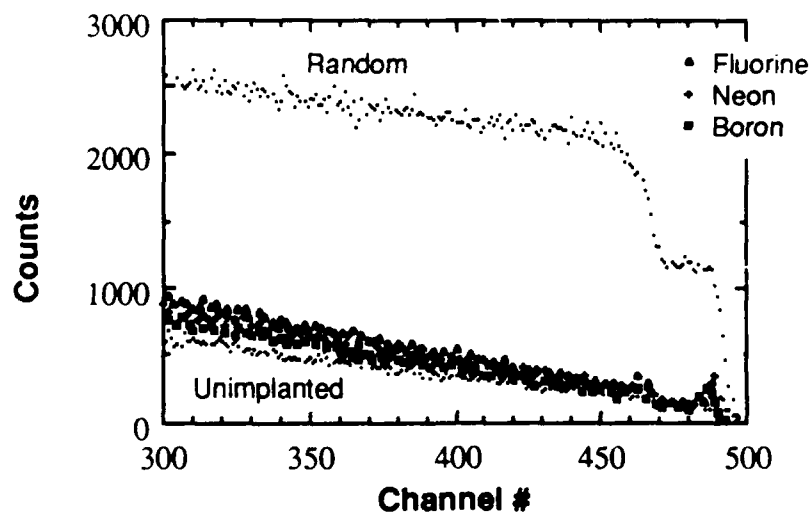
Fig. 5.4 Channeling measurements of the damage remaining in fluorine-, neon-, and boron-implanted samples following Anneal 1. The level of remaining damage is about the same in these three implanted samples and is also similar to that in the indium-implanted sample annealed for nine hours in Fig. 5.1. This indicates that the structure of as-implanted damage does not have a major effect on how much damage is repaired during Anneal 1.

also coincide with the spectra from the indium implants annealed for nine and thirty hours. This indicates that a 200° C anneal is sufficient to repair most, but not quite all, of the implant damage visible with channeling. Also, the amount of damage after annealing is almost independent of the ion species or dose for the range of conditions tried here. Comparison of boron and indium annealing spectra in Figs. 5.2 and 5.3 suggest that more heavily damaged samples do take more time to fully anneal, but we did not have enough samples to explore this possibility. The fact that such a wide variety of implant conditions result in such similar damage levels after annealing leads us to believe that the poor annealing of the boron implant in Fig. 5.3 may be due to the quality of the epilayer rather than implant parameters or damage structure. Comparison of the unimplanted spectra in Figs. 5.2, 5.3, and 5.4 shows that the backscattered yield from the unimplanted layers used for the boron implants is indeed higher than the yield for the layers used for the other implants. This is not surprising since the boron implants were done several years ago when material quality was not as good as it is now.

Though the damage as measured by channeling after the 200° C anneal is reduced to the same level independent of the implanted ion, the electrical results depend on the identity of the impurity. All as-implanted samples are n-type and after Anneal 1, boron and indium implanted samples remain n-type with a decreased carrier concentration and an increased mobility. In contrast, fluorine and neon implanted samples both become p-type with a carrier concentration similar to that of the unimplanted material. It seems that for the latter two cases, the electrically active damage is repaired during the first anneal, though some non-active damage remains visible to channeling. The boron and indium implanted samples remain n-type because they form stable, electrically active complexes during the 200° C anneal. The increased mobility is due to the partial repair of the implantation damage.

5.3.2 Anneal 2 and 3

A 4-5 minute thermal pulse anneal at 320° C is performed to further repair the remaining implantation damage which consists primarily of extended defects [5.12]. After this step the carrier concentration and mobility of fluorine and neon implanted samples do not change very much from Anneal 1, but boron and indium implanted samples become p-type. The electrical properties of all samples are now very similar to what they were before implantation, consistent with the removal of lattice damage, but no activation of the implanted impurities. In other words, additional implantation damage anneals at this temperature, but movement of the implanted atoms onto electrically active sites requires additional time.

Ideally we would just lengthen the time of the 320° C anneal step to activate the impurities, but unfortunately, even the "stabilized " ozone oxide begins to degrade for times longer than five minutes. We are thus forced to return to a long, low temperature anneal for activation (200° C, 12-18 hours). Channeling spectra taken after this step sometimes show that the post-implant annealed sample is of better crystal quality than the unimplanted material as shown in Fig. 5.3, but this depends on the starting quality of the epilayer. Since the starting material for our later experiments was of higher quality, it is sometimes not possible to anneal the implanted material to the original low damage level. Channeling spectra following the third annealing stage for some of the implants we have been discussing above are shown in Fig. 5.5. Note that the annealed indium implant spectrum shown in Fig. 5.5 cannot be directly compared with the implant spectra in Fig. 5.2 since it is from a different set of samples and was implanted with a different dose.
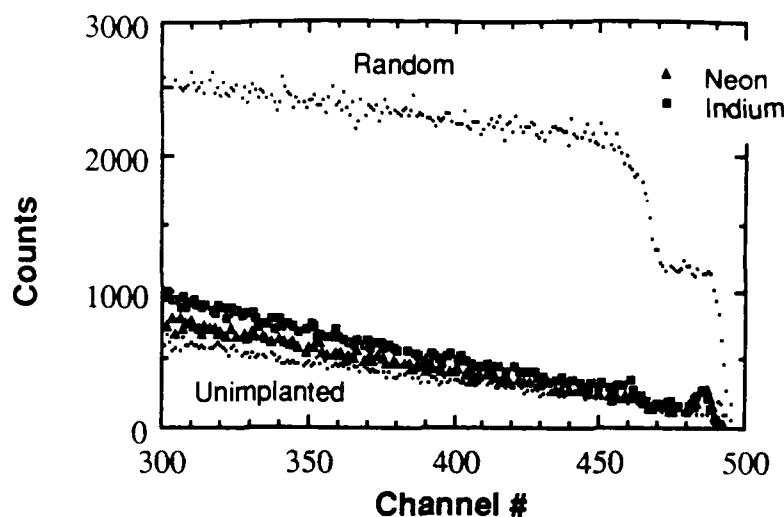
Fig. 5.5 Channeling spectra for neon- and indium-implanted MCT following Anneal 3. Almost all of the as-implanted damage has been repaired in both samples, though a low level of defects remains deep in the sample.

Van der Pauw measurements show that the carrier type of boron implanted samples has indeed changed from p- to n-type following the third annealing step. Electical results for samples implanted at either 77 K or room temperature are very similar. Indium implanted samples also change to n-type with a low carrier concentration and fairly high mobility, but fluorine and neon implanted samples remain p-type. As mentioned in §5.2.2, the growth of the ozone oxide forms a Hg accumulation region in the MCT that could result in n-type layer formation. Since the annealed fluorine and neon implanted samples are not n-type, however, the n-type doping of the annealed boron and indium implanted samples cannot be due to incomplete removal of this Hg-rich region. Also, though it was annealed under similar conditions to the boron implanted samples, the neon implanted sample remained p-type. This is strong evidence that the n-type activity in the boron implanted samples is due to boron and not to incomplete annealing of radiation damage.

One argument against the direct comparison of the neon and boron implants is that the neon implant was shallower, causing a higher concentration of defects which might

have affected the electrical results after annealing. The indium implants, however, created even more damage and the changes in carrier type and concentration tracked those of the boron implants. Thus, higher damage cannot explain the differences between the neon and the boron implants. In addition, the damage resulting from the fluorine implants was similar in structure to that from boron (extended defects to a depth of 4000-5000 Å), but the samples behaved differently under very similar annealing conditions. These observations lead us to believe that the electrical activity that we see in the boron and indium post-implant annealed samples is true chemical activation and not related to damage. This is an important result and finally shows that implanted boron can be successfully activated to form n-p junctions in MCT.

Differential van der Pauw results for annealed boron implanted samples [5.4] show that the n-type carrier profile closely follows the SIMS atomic profile in the tail region, though the peak carrier concentration is considerably less that the boron concentration. We tried to do similar measurements on annealed indium implanted material, but ran into some difficulties that we suspect are due to etching the epi layer back too far before implantation. Measurements proceed normally at first, with the sheet carrier concentration decreasing and the sheet resistivity increasing as each layer is removed, but after several measurements we encounter a high resistivity region. In this region, which is still n-type, the sheet resistivity and carrier concentration remain almost constant as successive layers are removed. SIMS data (discussed in more detail in a later section) indicate that at this depth the indium concentration is down to its background level – far too low to account for this carrier concentration even if the indium were 100% active. Another possibility is that Hg has diffused into this region, filling the p-type Hg vacancies and uncovering residual donors. The problem with this explanation is that we have no Hg source. We do not anneal in a Hg atmosphere (we use nitrogen or argon) and we etch away the Hg accumulation region before Anneal 3. The explanation that best fits the facts is that, for this set of samples, the

implanted region was too close to the region of misfit dislocations between the substrate and the MCT layer. We come to this conclusion because after the pre-implant etch we had to discard some samples that had darker regions around the edges where the substrate was showing through. The samples that we used for implantation did not show the substrate, but it is possible that the MCT layer was thin enough for the misfit dislocations near the interface to trap some of the n-type defects as they diffused in from the implanted region. The misfit dislocations themselves could also be contributing to the n-type activity since it is known that they play a role in n-type behavior [5.13].

5.4 Photoluminescence Measurements

5.4.1 Introduction

Photoluminescence (PL) experiments were performed to monitor how ion implantation and annealing affects the near band gap states and radiative transitions between these states. The implanted ions are the same as have been discussed above. The boron and neon implants were done using samples cut from the same piece of material and the fluorine and indium implants were done using samples cut from a second piece. Neither of the epilayers was intentionally doped. The details of the experimental setup used in this thesis and the fundamental optical processes studied are discussed in §2.2.4. Previous experimental work involving PL in MCT is summarized below.

5.4.2 Previous Results in MCT

Only a limited number of papers have been published dealing with photoluminescence in MCT and we will further restrict this brief review to studies of material with x values near $x = 0.3$, since that is the composition studied in this thesis. Papers studying both bulk and epitaxial material have been published on this composition and report finding up to three peaks in the near bandgap region with two of the peaks, A and B, observed in all of the studies [5.14 – 5.20].

Peak A is the highest energy peak and, as such, has been attributed to band to band recombination or possibly to a bound exciton. Additional evidence supporting the identification of band to band transitions includes a shift to higher energies as temperature is increased and a superlinear increase in intensity as pump power is increased.

Peak B, also seen in all studies, is lower in energy and is attributed to donor to acceptor level transitions at low temperatures. Above ≈ 10 K the donors become ionized and the peak is due to band to acceptor transitions. The fact that it appears in both p-type and n-type material suggests that it is due to a native crystal defects. Hg vacancies [5.15] or an anion-site impurity [5.19] are good candidates for the acceptor level and residual impurities probably account for the donor level. The peak is generally separated from peak A by 15 to 16 meV leading to the conclusion that the acceptor ionization energy is ≈ 16 meV. The donor ionization energy was calculated to be 1 meV [5.17].

Three peaks were reported by two authors, but the third peak in each case arises from different causes. Gelmont, et. al. [5.16] report a peak 7-9 meV below peak A that only appears at high excitation levels and attribute it to an acceptor-exciton complex, whereas peak C found by Myles, et. al. [5.19] is 28 meV below peak A and is tentatively identified as being associated with a (vacancy, anion impurity) complex.

5.4.3 Results and Discussion

5.4.3.A Before Implantation

We observe three peaks in PL spectra taken at liquid He temperature on unimplanted samples. The first two are near band gap peaks and correspond to peaks A and B discussed above. Assuming that peak A is due to band-to-band recombination, we measure the energy difference between A and B, and thus the acceptor ionization energy, to be 16-17 meV in agreement the results cited above. The third peak, C, appears at considerably lower energy and, to the best of our knowledge, has not previously been seen

in material of this composition using photoluminescence. Though our measurements indicate that the peak energy is closer to $\frac{2Eg}{3}$, uncertainties in the composition-band gap relation and peak location make it possible that this peak can be identified with the $\frac{3Eg}{4}$ peak observed by Jones *et al.* using DLTS [5.21, 5.22].

Increasing the temperature leads to a broadening and deterioration of peaks A and B until at 77 K we observe only one peak in the near band gap region. An appreciable fraction of the acceptors will be ionized at this temperature, reducing the concentration of neutral acceptors. Since the band-to-acceptor transition probability is proportional to N_A, this will cause a decrease in the relative intensities of peak B to A. Thus the dominant contribution to the single near band gap peak visible at 77 K is due to band-to-band recombination, overlapping with a smaller contribution from band-to-acceptor transitions. Peak A shifts to higher photon energy as the temperature is increased, but by more than the band gap alone increases (note that, unlike most semiconductors, Eg increases with increasing temperature for MCT with $x \le 0.5$). The shape of this peak and its dependence on temperature has been explained by Hunter *et al.* as being due to interband transitions without k-conservation [5.17]. Werner et al. also got a better fit to their data assuming k is not conserved [5.23]. Apparently, random fluctuations in composition in the alloy act as scattering centers for electrons and lead to relaxation of the wave-vector selection rules. Peak C is still visible at 77 K, though its low intensity did not permit us to take spectra with acceptable resolution from the unimplanted samples.

The samples studied varied laterally in composition as indicated by shifts in the location of peak A and in impurity/defect concentration as indicated by the relative intensities of peaks A and B. Fig. 5.6 shows an extreme example of the latter in which only peak A is visible at one spot on the sample, though under similar excitation conditions both peaks A and B appear from another spot on the same sample. Variations in relative peak intensity have been correlated with etch-pit density profiles across the diameter of

LEC GaAs wafers, yielding characteristic W- and M-shaped intensity profiles. It might be possible to correlate intensity ratios in LPE MCT to substrate properties in a similar manner. Also note that peak A shifts by 3-4 meV from one spectrum to the other, indicating a change in x-value of ≈ 0.003. We have observed shifts of up to 20 meV for peak A, corresponding to $\Delta x \approx 0.015$, in other samples. Such composition fluctuations will also broaden the luminescence peaks as discussed by Hunter, et al. [5.17].
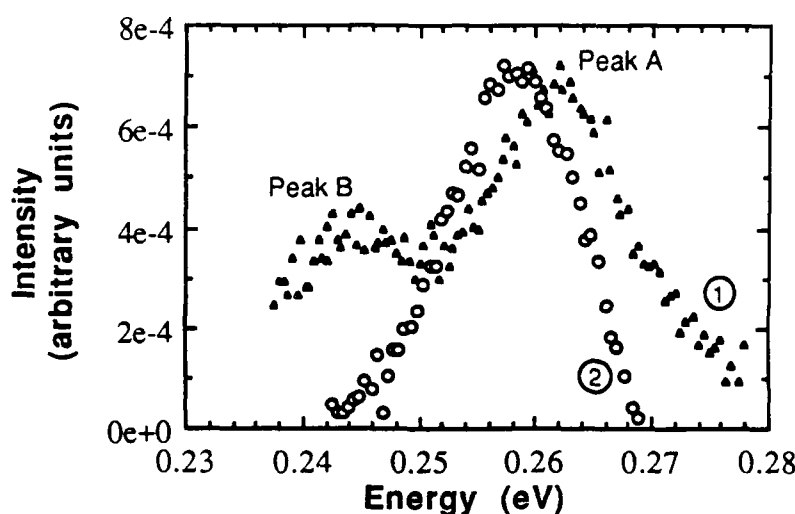
Fig. 5.6 Spectra of unimplanted MCT showing photoluminescence intensity vs photon energy at liquid He temperature. Peak A, at the highest energy, is attributed to band-to-band recombination and peak B is attributed to band-to-acceptor recombination. In spectrum (1) we observe both of the near band gap peaks, though in spectrum (2), taken from another spot on the same sample, only peak A appears. This indicates that the impurity/defect concentration varies with position. Also, peak A shifts by 3-4 meV between (1) and (2) which corresponds to a change in x-value of ≈ 0.003.

5.4.3.B After Implantation

Attempts at taking PL spectra of as-implanted samples indicate that implantation of any of the above ions either reduces the photoluminescence below the level of detection of our system or completely quenches it in agreement with [5.24]. After annealing we were at first able to detect only faint luminescence from samples after each of the annealing stages with the "brightest" signals coming from samples after Anneal 2. Though the weakness of the signals severely limited the resolution, the spectra showed the same peaks as spectra

from samples before implantation with no obvious dependence on the identity of the implanted ion.

The PL intensity increased remarkably in these samples following the removal of the top 1000 - 1800 Å, with a signal of up to 40 times that of the brighest unimplanted sample. This indicates that the combination of oxide growth followed by annealing forms a thin layer with a high surface recombination velocity that reduces the PL intensity. (Such a layer is also consistent with anomalous results sometimes observed for the first layer of differential Hall measurements on annealed samples. After the top 500-600 Å is removed, subsequent Hall measurements behave as expected.) PL spectra taken from unimplanted samples that have undergone multiple anneals show similar behavior. Unetched samples only luminesce faintly, but after the top 1200 Å is removed the signal is significantly brighter than it was before annealing.

The reappearance of luminescence following Anneal 1 is consistent with RBS results showing nearly complete repair of implantation damage after this annealing step. The fact that it is brighter than in unimplanted samples indicates that many nonradiative recombination centers present even before implantation have been removed by annealing. Following Anneal 3, peak A increases in intensity by a factor of ≈ 2 over its intensity after Anneal 1, which is also consistent with RBS results showing a reduction in damage between these annealing steps.

PL spectra taken from etched, annealed samples still show the same features as those taken before implantation, but the increase in signal allows us to use a greater range of power levels and to get better resolution, especially of Peak C. Figs. 5.7a and b show spectra obtained at liquid He temperature from a boron-implanted sample after Anneal 3 with the top 4800 Å removed (approximately at R_p). At these power levels all three peaks are visible (the long, low energy tail of peak A is actually due to peak B). We see no
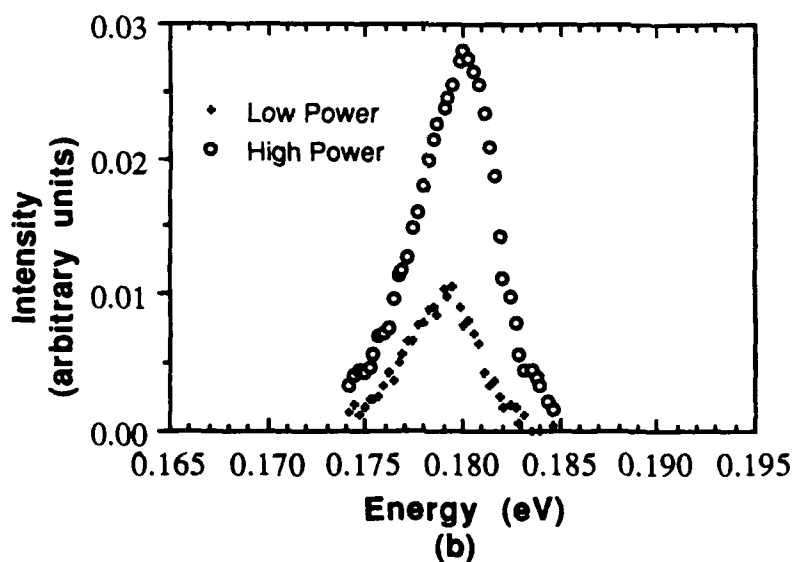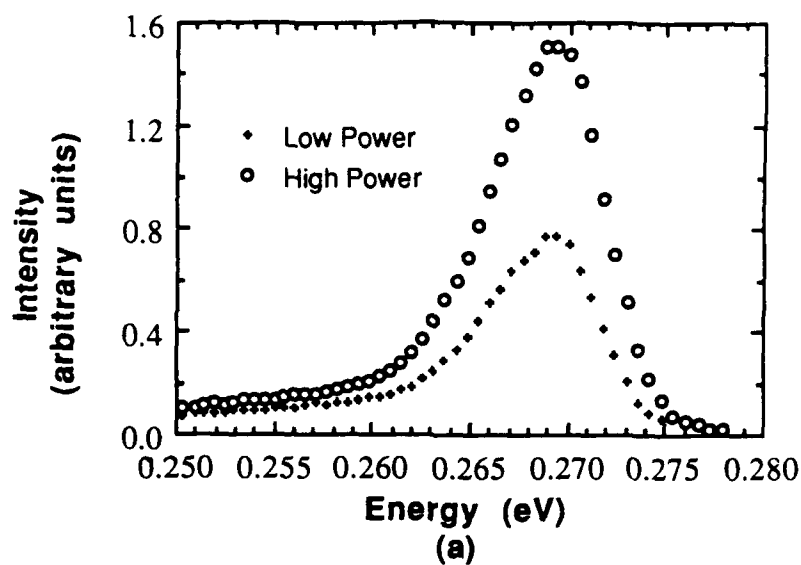
Fig. 5.7 Photoluminescence spectra of post-implant annealed MCT showing the behavior of (a) peak A and (b) peak C as the pump power is varied at liquid He temperature. The same detector was used for collecting all four spectra, so the intensities can be compared between (a) and (b). The intensity of peak C appears to vary more strongly with pump power than that of peak A, but this is due increasing overlapping of peaks A and B as the pump power is decreased.

evidence of the implantation induced level at E_c - 0.19 eV reported by Cotton, *et al.* [5.25] at any power level. Obviously this does not mean that it is not there, just that it is a nonradiative center, and its formation and properties must be studied by some other method. As the laser power is decreased, Fig. 5.8, peak B increases in intensity relative to peak A. Peak C is too faint to get acceptable resolution at these power levels and is not shown. This behavior of peaks A and B is again consistent with their origins in band-to-band and band/donor-to-acceptor recombination, respectively. At this low temperature and
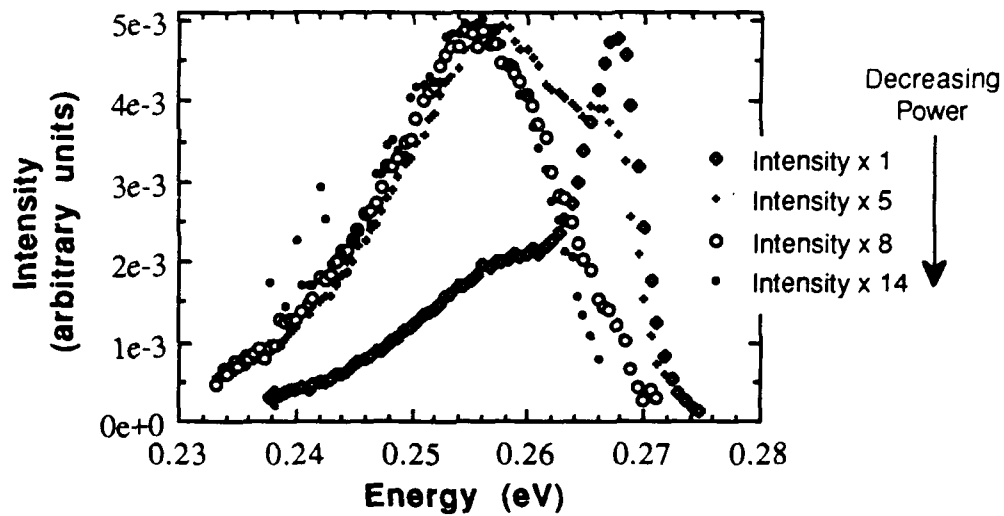
Fig. 5.8 Photoluminescence spectra of post-implant annealed MCT at liquid He temperature at lower pump powers than in Fig. 5.6. Peak C is not visible at these low pump powers. As the pump power is decreased, peak B increases in intensity relative to peak A. These spectra were taken with a different detector so peak intensities cannot be directly compared with Fig. 5.6.

at low power levels the transition probability for donor-to-acceptor recombination should be $\propto AN_AN_D$ and should increase as AN_An_e with increasing power since more electrons are being excited to the conduction band (the expected peak shift due to the estimated donor binding energy of ≈ 1 meV as the transition changes from donor-to-acceptor to band-to-acceptor is very hard to detect in this case due to overlap with peak A). The corresponding expression for band-to-band recombination is $Bn_hn_e = Bn_en_e$. Since N_A and N_D do not

change with pump power, the ratio of band-to-band to band-to-acceptor intensity should go as $\approx$ constant n_e, which increases with increasing pump power, exactly the behavior that is observed.

Peak B has been tentatively identified as an acceptor level due to an isolated anion-site impurity, perhaps As or P [5.19]. However, the fact that we observe this peak both before and after implantation in undoped samples suggests that if it is due to impurities substituting on the Te sublattice, they must be uncontrolled residual impurities. Another possible source for the level is Hg vacancies, known to be acceptors. More samples should be studied and relative peak intensities should be correlated with carrier concentrations and impurity levels to see if this peak is indeed due to residual acceptors or to Hg vacancies.

Though it is not possible to identify the origin of peak C based on the information we have at this time, we can make a few observations about its behavior:

1) The intensity of the peak increases superlinearly with pump power, consistent with a transition involving a free carrier or carriers.

2) As temperature is increased the peak shifts to higher energy by $\approx \frac{1}{2} k_b \Delta T$ in addition to the band gap increase. The shift as temperature is increased also implies that free carriers are involved in the transition, but the shift is of smaller magnitude than that of peak A with temperature, which is consistent with a transition involving one free carrier instead of two.

3) As the pump power increases, the peak shifts asymmetrically to higher energies at both He temperature and 77 K. At He temperature, as the pump power is increased by a factor of three, the peak shifts to higher energy by 2 meV, and the energy of the half maximum of the high energy side increases by 4.2 meV. At nitrogen temperature, the shifts are about half those at He temperature. These are large energy shifts to be caused by such small variations in pump power. Such a shift is consistent with transitions from the

conduction band of MCT to a deep level because of the very low density of states in the conduction band of MCT ($N_C \approx 2 \times 10^{15}$ cm^{-3} at 77 K, $\approx 2 \times 10^{13}$ cm^{-3} at 4 K [5.26]). In fact, at the levels of excitation used in this thesis, the quasi-Fermi level for electrons has been driven into the conduction band. Thus, as the pump power increases, states higher in the conduction band become filled, permitting emission at higher photon energies. This causes the high energy edge of the peak to shift to higher energies and increases the fwhm of the peak. Because of the larger density of states in the valence band ($N_V \approx 10^{18}$ cm^{-3} at 77 K [5.27]), if the transitions were from the valence band to a deep level, we would expect no peak shift or only a very small shift with this small a variation of pump power. The band-to-band peak should show similar behavior as the pump power is changed, but the peak shift is masked by interference from peak B.

Optical transitions of similar energy to peak C have been seen using optical modulation spectroscopy [5.28] at 94 K and ascribed to the $\frac{3Eg}{4}$ level. They suggest a model in which the initial state is the same shallow acceptor that we identify with peak B and the final state is a donor-like deep level. However, the energy of a transition between two localized levels should not be a function of pump power as we observe using PL. Based on these observations, we tentatively associate peak C with a transition from the conduction band to a deep level. We can further identify it with the $\frac{3Eg}{4}$ level observed in DLTS measurements of undoped material, in which case it has been suggested that the defects are donors and are cation impurity related [5.19, 5.22]. Because of the high concentrations observed in DLTS it is considered that the most likely candidate is antisite Te [5.22].

5.5 SIMS Measurements

SIMS measurements were performed on samples at various points in the annealing sequence to see how annealing affects the profile shapes for boron, indium, and fluorine. We were not able to measure the neon profiles because of high background levels. Some

of the LPE samples that we used have a fairly rough surface which decreases the accuracy of the depth measurement, but general trends and shapes are obvious.

5.5.1 Boron

Boron has been reported to be rather immobile in MCT by other workers [5.7] and this agrees with previous work done in this program [5.4]. SIMS results show only slight broadening of the profile shape for post-implant annealed samples when compared to as-implanted sample. This broadening could be due to a small amount of boron diffusion or it could be an artifact of the surface roughness of the LPE samples. Because of its immobility, no boron loss during annealing is expected or observed.

5.5.2 Indium

In contrast to boron, indium is known to redistribute in MCT for typical annealing temperatures (T ≥ 250° C) [5.5, 5.29]. To see if indium is mobile under our annealing conditions, long 200° C anneals and a short pulse at 320° C, we made SIMS measurements on samples at different stages in the annealing sequence, as illustrated in Fig. 5.9. The samples were implanted with 300 keV indium to a dose of 6 x 10^{12} cm^{-2} at 77 K and the resulting peak in the as-implanted atomic profile appears at ≈ 850 Å, in excellent agreement with the calculations in Chapter 3. After a nine hour furnace anneal at 200° C the indium peak appears at ≈ 1000 Å, but the general shape of the profile remains the same. The difference in peak depths is probably due to uncertainty in the depth scale rather than indium diffusion. Five minutes at 320° C does not cause the peak to move any deeper, but the tail of the distribution is slightly deeper either because of a small amount of diffusion or depth scale uncertainties again. These results show that ozone oxide growth does not appear to affect the indium profile, *i.e.* the oxide neither preferentially rejects nor incorporates indium. The as-grown ozone oxide also does not allow significant loss of indium when annealed at 200° C, even for many hours, and it still forms an effective barrier to indium during the short higher temperature anneal.
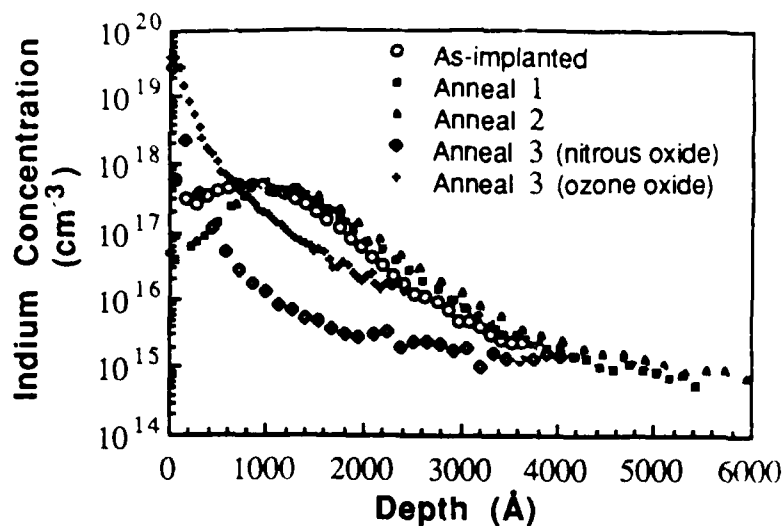
Fig. 5.9 SIMS profiles of indium-implanted MCT as a function of annealing step. Little movement of indium is observed following Anneal 1 or Anneal 2, but most of the indium is lost following Anneal 3. This happens because (1) nitrous oxide is porous to indium at 200° C and (2) degradation of the ozone oxide during Anneal 2 makes it porous to indium during Anneal 3.

During the third anneal, however, significant amounts of indium are lost, both with the standard, regrown nitrous oxide and when the same ozone oxide is used for all three annealing steps. The latter experiment proves that the indium loss is not due to segregation into the nitrous oxide during oxide growth. One explanation is that the nitrous oxide, unlike the ozone oxide, is porous to indium at 200° C because of its higher number of defects. When ozone oxide is used for all three annealing steps it is not as good a barrier to indium during the last step because it is degraded by Anneal 2. It is likely that growing a fresh ozone oxide instead of a nitrous oxide after Anneal 2 would keep the indium in the sample since it worked for Anneal 1, but we did not have enough samples to try this experiment. Also, growing ozone oxide twice during processing it not practical since this would devote twelve days to oxide growth alone. A better solution would be to deposit a additional layer on top of the oxide to serve as a barrier to indium, either for all three annealing steps or only for Anneal 3. Note that though it is commonly used as cap for

MCT, ZnS is not a good choice for our purpose here since it has been shown to permit out diffusion of indium during post-implant annealing [5.29].

5.5.3 Fluorine

Little information is available on implanted fluorine ranges and diffusion behavior in MCT, though fluorine would be expected to be a fast diffuser because of its small size. Our samples were implanted with 350 keV fluorine to a dose of 3.8 x 10^{13} cm^{-2} at 77 K. The resulting profile peaked at ≈ 3200 Å with $R_p \approx 3700$ Å and $\Delta R_p \approx 2000$ Å which is somewhat more shallow and broad than TRIM calculations. Since fluorine is a light ion it was necessary to correct the electronic stopping so we fit BTE calculations to the SIMS data as discussed in Chapter 3.

We found that implanted fluorine redistributes dramatically in response to annealing, forming a distinct double peak structure as shown in Fig. 5.10. Almost all of the movement occurs during Anneal 1. The main change occurring during Anneals 2 and 3 is that the height of the deeper peak steadily decreases. Because of sample roughness, the differences in peak depths for the different annealing steps are within experimental error.

The redistribution of implanted fluorine in MCT is similar to that seen in silicon following annealing of BF$^+_2$ implants [5.30, 5.31]. In these studies the first peak was found between the sample surface and the original amorphous-crystalline interface and was thus attributed to fluorine being shoved ahead of the interface during regrowth in a manner reminiscent of zone-refining. The second peak is assumed to be due to gettering by implantation damage deeper in the sample since the F concentration in this region is found to be higher than it was after implantation. It was later found that double peak formation occurs even if the sample is not amorphized by the implant [5.32], indicating that repair of heavily damaged regions also causes fluorine segregation. The minima in the profiles

generally correspond to the location of the crystalline-amorphous interface or the heavily damaged layer.

The behavior of fluorine in post-implant annealed MCT can be explained in a similar way. Though the MCT is not amorphized during the implant, the minimum between the peaks corresponds roughly to the end of the heavily damaged region as measured by RBS channeling. The shallower peak could thus be due to fluorine being shoved out as the most heavily damaged crystal regrows locally on the less damaged crystal underneath. Comparison with BTE stoichiometry calculations shows that the minimum also corresponds with the Te-rich region. Since F is expected to substitute on the Te sublattice, the presence of excess Te during annealing could cause even more fluorine to be shoved away to either side of the region. The second peak is attributed to F decorating deeper damage below the level detectable by channeling and also corresponds to the anomalous p⁻ region extending from ≈ 5500 Å to 8000 Å found in differential Hall measurements on as-implanted samples.
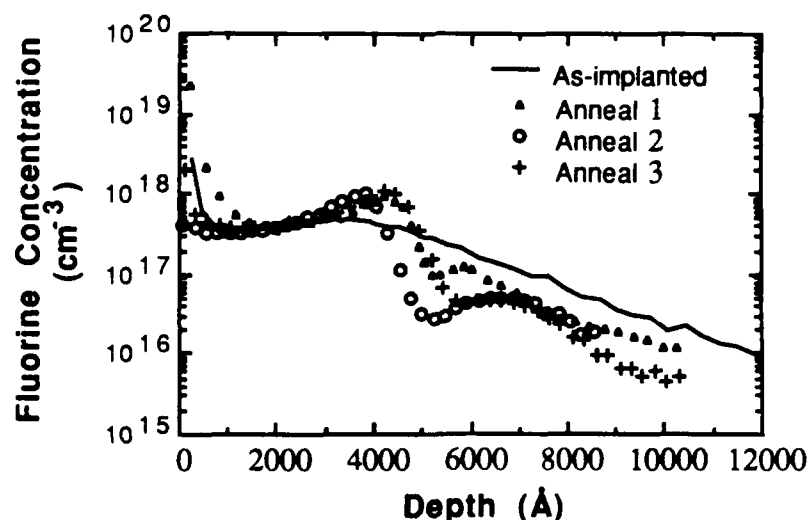

Fig. 5.10 SIMS profiles of fluorine-implanted MCT as a function of annealing step. The fluorine redistributes dramatically following Anneal 1 into a double peak structure. The shallower peak forms as fluorine is pushed ahead of the regrowing crystal during annealing and the deeper peak is due to the decoration of implant damage below the level detectable by channeling.

It is interesting to note that the F concentration in the peak 1 is greater than that at the same depth in the as-implanted case, indicating that some damage gettering may also occur in this region. This F must be bound in stable defects since the height of this peak does not decrease with further annealing. In contrast, the deeper peak, peak 2, has a lower F concentration than in the as-implanted state and the peak broadens and decreases in height with each annealing step. This indicates that though a good deal of the implanted F in this region becomes bound in stable defects during Anneal 1, some F is able to diffuse away. Also, these defects do not getter additional F as they do in Si. The decrease in height of the peak in going from Anneal 1 to 2 is much greater than that in going from Anneal 2 to 3. Assuming that bound F is released as the defect concentration decreases, this suggests that defects stable at 200° C may not be stable at 320° C, but that five minutes is not long enough to repair them all. This is consistent with the discussion above where we suggested that Anneal 2 repairs most remaining implant damage, but is not long enough to activate the implanted ions.

The fact that the F redistributes so dramatically during Anneal 1 and so little during the subsequent anneals is evidence that the initial diffusion is enhanced by implantation damage. After this damage is repaired by the first anneal, most of the F is bound in stable defects and the mobility of the small amount of free F is considerably reduced. This reduction in mobility is only relative to the very fast initial diffusion since we can see from the behavior of the deeper peak that F can diffuse in MCT at only 200° C. It is not surprising that F is very mobile in MCT simply because it is so small, but it is interesting to compare its mobility in MCT to that in Si where no movement is detected for temperatures below 700° C [5.31].

Impurity redistribution in MCT as a result of implantation has also been observed for other impurities, specifically Li and Na [5.6, 5.33]. In those studies, however, the Li

and Na were already present as background impurities and redistributed during boron implants and during post-implant annealing. It was concluded that the alkaline impurities have an affinity for native acceptor sites (Hg vacancies) and that Li also decorates implantation damage. Following annealing the Li profile had a minimum slightly beyond R_p for boron (this depth corresponds to the end of the damaged region measured by channeling as discussed in Chapter 3) which is similar to the location of the F minimum in the present work. These results suggest that defect analysis employing implanted F in combination with residual impurities could be a powerful tool to profile as-implanted damage below the level detectable by RBS or TEM and thus further our understanding of the process of junction formation.

5.6 Summary

This chapter has presented measurements of damage repair and dopant activation in MCT as a function of annealing step following the implantation of different ions. We confirmed that boron can be at least partially activated by a multiple step anneal because neon, similar in mass to boron, does not show any n-type activity when the same annealing sequence is followed. Since neon is inert, this proves that the electrical activity seen in post-implant annealed boron samples is due to actual activation of the implanted boron and not to radiation induced defects, thus resolving the controversy over boron activation. We find that indium shows n-type activity following annealing and the fluorine-implanted sample shows no signs of fluorine activation.

Results from MeV ion channeling show that most of the implantation damage is removed by annealing, but that a small amount of defects, probably dislocation loops, remain in all samples. Photoluminescence measurements indicate that this residual damage has little effect on the optical properties of the samples since luminescence peaks from post-implant annealed samples are brighter than peaks in the same material before implantation. We see no evidence of near band gap defect levels induced by implantation in our

luminescence spectra nor do we see any additional transitions due to dopant activation. We do see a longer wavelength peak in both unimplanted and post-implant annealed material that, to the best of our knowledge has not been previously reported from PL spectra of MCT of this composition. Though our measurements indicate that the peak energy is closer to $\frac{2E_g}{3}$, uncertainties in the composition-band gap relation and peak location make it possible that this peak can be identified with the $\frac{3E_g}{4}$ peak observed using DLTS.

SIMS measurements show that boron does not redistribute under our annealing conditions, confirming previous observations that boron is not very mobile in MCT [5.7]. Indium shows little movement due to the first two annealing steps, but most of the indium is lost through the surface during Anneal 3, indicating that improvements are needed in oxide growth. Fluorine redistributes dramatically during Anneal 1 and decorates implantation damage. Its mobility is apparently enhanced by the damage since it shows only a small amount of movement at the same time that ion channeling shows that most of the damage is repaired.

5.7 References

[5.1]   M.A. Herman and M. Pessa, J. Appl. Phys. **57**(8), 2671 (1985).

[5.2]   K.C. Dimiduk, Mercury Loss, Annealing and Ion Implantation in Mercury Cadmium Telluride, Ph.D. Thesis, Stanford University, July 1983.

[5.3]   T.-M. Kao, T.W. Sigmon, and L.O. Bubulac, J. Vac. Sci. Technol A **5**(5), 3175 (1987).

[5.4]   T.-M. Kao, Development of Direct Ion Implantation Processes and Characterization Techniques for Mercury Cadmium Telluride Epilayers, Ph.D. Thesis, Stanford University, May 1987.

[5.5]   L.O. Bubulac, D.S. Lo, W.E. Tennant, D.D. Edwall, and J.C. Robinson, J. Vac. Sci. Technol. A **4**(4), 2169 (1986).

[5.6]   G.L. Destefanis, J. Crystal Growth, **86**, 700 (1988).

[5.7]   J. Barrs, A. Hurrle, W. Rothermund, C.R. Fritzsche, and T. Jakobus, J. Appl. Phys. **53**(3), 1461 (1982).

[5.8] T.-M. Kao and T.W. Sigmon, presented at the Dielectric Films on Compound Semiconductors Syposium, 172nd Meeting of the Electrochemical Society, Inc., Honolulu, Hawaii. October, 1987.

[5.9] T.-M. Kao and T.W. Sigmon, J. Appl. Phys. 64(2), 864 (1988).

[5.10] B.K. Janousek and R.C. Carscallen, J. Vac. Sci. Technol., A 3(1), 195 (1985).

[5.11] G.D. Davis, S.P. Buchner, J.S. Ahearn, and N.E. Byer, SPIE 409, 35 (1983).

[5.12] G.L. Destefanis, Nuc. Inst. and Meth. 209/210, 567 (1983).

[5.13] B. Pelliciari, J. Crystal Growth 86, 146 (1988).

[5.14] C.T. Elliott, I. Melngailis, T.C. Harman, and A.G. Foyt, J. Phys. Chem. Solids. 33, 1527 (1972).

[5.15] V.I. Ivanov-Omskii, V.A. Maltseva, A.D. Britov, and S.D. Sivachenko, Phys. Stat. Sol. (a) 46, 77 (1978).

[5.16] B.L. Gelmont, V.I. Ivanov-Omskii, V.A. Maltseve, and V.A. Smirnov in *Proceedings of the 4th International Conference on the Physics of Narrow Gap Semiconductors*, held at Linz, Austria, September 1981, edited by E. Gornik, H. Heinrich, and L. Palmetshofer, Springer-Verlag, New York, 1982.

[5.17] A.T. Hunter and T.C. McGill, J. Appl. Phys. 52(9), 5779 (1981).

[5.18] A.T. Hunter and T.C. McGill, J. Vac. Sci. Technol., 21(1), 205 (1982).

[5.19] C.W. Myles, P.F. Frazer, R.A. Chapman, and E.G. Bylander, J. Appl. Phys. 57(12), 5279 (1985).

[5.20] P. Gille, K.H. Herrmann, N. Puhlmann, M. Schenk, J.W. Tomm, and L. Werner, J. Crystal Growth 86, 593 (1988).

[5.21] C.E. Jones, V. Nair, and D.L. Polla, Appl. Phys. Lett. 39(3), 248 (1981).

[5.22] C.E. Jones, V. Nair, J. Lindquist, and D.L. Polla, J. Vac. Sci. Technol., 21(1), 187 (1982).

[5.23] L. Werner and J.W. Tomm, Phys. Stat. Sol. (a) 103, K61 (1987).

[5.24] C. Uzan, Y. Marfaing, R. Legros, R. Kalish, and V. Richter, J. Crystal Growth, 86, 744 (1988).

[5.25] V.A. Cotton and J.A. Wilson, J. Vac. Sci. Technol. A 4(4), 2177 (1986).

[5.26] M.A. Kinch, M.J. Brau, and A. Simmons, J. Appl. Phys., 44(4) 1649 (1973).

[5.27] J.A. Mroczkowski and D.A. Nelson, J. Appl. Phys. 54(4), 2041 (1983).

[5.28] D.L. Polla, R.L. Aggarwal, J.A. Mroczkowski, J.F. Shanley, and M.B.Reine, Appl. Phys. Lett. 40(4), 338 (1982).

[5.29] G.L. Destefanis, J. Vac. Sci. Technol A 3(1), 171 (1985).

[5.30] M.Y. Tsai, B.G. Streetman, P. Williams, and C.A. Evans, Jr., Appl. Phys. Lett. 32(3), 144 (1978).

[5.31] M.Y. Tsai, D.S. Day, B.G. Streetman, P. Williams, and C.A. Evans, Jr., J. Appl. Phys. 50(1), 188 (1979).

[5.32] M. Delfino, and M.E. Lunnon, J. Electrochem. Soc., 132(2), 435 (1985).

[5.33] L.O. Bubulac, W.E. Tennant, R.A. Riedel, J. Bajaj, and D.D. Edwall, J. Vac. Sci. Technol. A 1(3), 1646 (1983).

Chapter 6

Summary and Suggestions for
Future Work

6.1 Summary

Though it is a very convenient method of forming p-n junctions for photovoltaic devices, ion implantation in MCT is still a poorly understood process. In this work we have attempted to further the understanding of the effects of implantation in MCT by calculating atom and damage profiles, studying the effects of systematically varying implantation parameters, and monitoring the repair of implant damage and dopant activation during annealing.

We used two implant simulators to model the implantation process, the Boltzmann Transport Equation method (BTE) and TRIM, a Monte Carlo method. The basic assumptions and limitations of these two calculation schemes were described in some detail along with the fundamentals of ion implantation. Atom and damage profiles were calculated as a function of energy using both methods for ^{4}He, ^{9}Be, ^{11}B, ^{19}F, ^{20}Ne, ^{27}Al, ^{35}Cl, ^{114}Cd, ^{115}In, ^{127}I, and ^{130}Te and we saw that TRIM calculations for both the light and the heavy ions and BTE calculations for the heavy ions are in excellent agreement with SIMS measurements performed for this thesis and data from the literature. The treatment of electronic stopping in the BTE method, however, is less sophisticated than that in TRIM so for BTE calculations of light ion profiles (for which electronic stopping dominates nuclear stopping) the electronic stopping must be empirically modified for the calculated profiles to agree with the SIMS data. For this reason we suggest that TRIM be used to calculate light ion profiles in MCT and the BTE method, because it is faster, be used to calculate heavy ion profiles.

We have also discussed the calculation of recoil range distributions and stoichiometry imbalances due to implantation. We saw that light ion implantation results in excess metal atoms (H_g and Cd) near the projected range of the ion and excess Te beyond the projected range. For heavy ions, the magnitude of the stoichiometry disturbance is greater, as expected, with excess metal atoms located more shallow than the projected range and excess Te again beyond the projected range. Stoichiometry imbalances may affect damage repair and redistribution of implanted atoms during annealing as illustrated by the behavior of fluorine in annealed fluorine-implanted samples.

MeV ion channeling measurements of as-implanted MCT show that residual damage depends strongly on collision cascade density and implant temperature with low cascade densities and higher temperatures resulting in more "efficient" dynamic annealing and thus lower damage levels. Implantation of light ions at 77 K and room temperature and heavy ions at room temperature results in extended defects whereas implantation of heavy ions at 77 K leaves a high density of point defects near the surface. We see evidence that MCT implanted with heavy ions at 77 K may actually be amorphized during the implant, but anneals as it is brought back to room temperature. In addition, the lower density collision cascades and higher implant temperatures are found to consistently result in higher sheet carrier concentrations in as-implanted material. This suggests that several types of defects are formed during implantation, some electrically active and some inert or compensating. When ion tracks can anneal "efficiently", more of the electrically active defects form, but denser collision cascades and lower defect mobilities promote the formation of the inactive defects.

The transient temperature rise under the ion beam as it passes over a spot on a MCT sample was calculated and found to be acceptable for conservative implant conditions (beam current ≤ 1 μA cm^{-2}). It was found, however, that bulk heating can significantly

affect the damage profile in poorly heat sunk samples implanted at low temperatures (no such effect was seen for poorly heat sunk samples implanted at room temperature). Also, residual implantation damage as measured by MeV ion channeling was found not to depend upon the beam current for values ranging from 0.2 to 5 μA.

We showed that multiple step annealing using a native oxide cap removes almost all of the implantation induced damage that can be seen with MeV ion channeling, leaving behind a low level of defects that does not depend on the identity of the implanted ion for the ions studied in this work. Bright photoluminescence spectra from post-implant annealed samples indicate these remaining defects are not detrimental. This work also confirms that the n-type activity following native oxide encapsulation and multiple stage annealing of boron- and indium-implanted MCT is due to partial activation of the dopants since neon- and fluorine-implanted samples undergoing the same processing steps revert to p-type activity.

Photoluminescence is quenched in as-implanted samples, but reappears following the first annealing step. Following the last anneal the PL intensity is up to 50 x brighter than in unimplanted samples, indicating that annealing removes nonradiative centers from the material. We see no evidence of near band gap defect levels induced by implantation, nor do we see any additional transitions due to dopant activation. We do, however observe a long wavelength peak in both unimplanted and post-implant annealed material that, to the best of our knowledge has not been previously reported from PL spectra of MCT of this composition. We tentatively identify it with the $\frac{3E_g}{4}$ peak observed using DLTS.

6.2 Suggestions for Future Work

One very obvious extension of the work described in this thesis is to extend atom range and profile calculations and implant damage studies to other MCT compositions of interest *ie*. x ≈ 0.2, used for detectors sensitive to wavelengths from 8-14 μm. Ion ranges

should be slightly shorter in the lower x value material because of its higher density and the damage should be somewhat greater due to the increased number of Hg-Te bonds (weaker than Cd-Te bonds). An earlier study of implantation damage as a function of x-value at 170 K, however, indicates that damage measured by MeV ion channeling first increases and then saturates as the x value is decreased from x = 1 (CdTe) to x = 0.2 [6.1]. Based on our implantation damage studies, we suggest that this saturation behavior was due to annealing as the samples were warmed to room temperature, rather than actual damage saturation during the implant. Further work in this area would be very interesting.

Another area that it might be useful to explore is implanting MCT at slightly elevated temperatures. Our results show consistently higher sheet carrier concentrations and lower residual damage for warmer implants. For devices still using damage junctions the higher carrier concentration in the n region should lower the dark current because the number of minority carriers will be reduced and the lower damage levels will result in better mobility and fewer noise sources. For annealed junctions, the lower damage level should make annealing easier. Implantation through the native oxide cap would allow even higher target temperatures while minimizing the introduction of foreign species into the MCT layer through recoil implantation.

The success of the native oxide cap and multiple stage anneal in repairing radiation damage and partially activating implanted boron and indium suggests that further work should be pursued with these dopants to optimize the annealing process. To increase dopant incorporation it may be wise to study substituting a shorter, higher temperature laser pulse for the five minute thermal pulse currently used. The right combination of time and laser power would ideally avoid degrading the native oxide cap, while allowing the sample to reach a high enough temperature to move most of the implanted ions onto lattice sites and complete damage repair. In addition the implantation and annealing studies should be expanded to include other n-type (Al, Cl, I, *etc.*) and p-type (P, As, Sb, *etc.*) dopants.

DLTS, variable temperature Hall, and photoluminescence should be employed to study energy levels related to implantation or to activated dopants. The present photoluminescence studies could be improved by using detectors sensitive to wavelengths > 12 μm (the longest wavelength studied in this work) to look for shallow transitions and by using a tunable laser to excite the luminescence.

6.3 References

[6.1] H.L. Dunlap, K.V. Vaidyanathan, L.K. Magel, T.W. Sigmon, and C.Y. Huang, presented at EMC, Boulder, Colorado (1985).

Appendix

Ion Profile Statistics for Ions Implanted into $Hg_{0.7}Cd_{0.3}Te$

Ion	Energy (keV)	Rp (Å)	ΔRp (Å)	γ (Å)	ß (Å)
^{4}He *	10	865	452	0.41	2.64
	50	2609	1145	-0.03	2.31
	100	4343	1650	-0.28	2.50
	130	5247	1813	-0.43	2.69
	160	6089	1998	-0.47	2.79
	190	6928	2163	-0.55	2.88
	220	7703	2334	-0.60	3.02
	250	8530	2503	-0.67	3.12
	300	9811	2677	-0.74	3.39
	350	10986	2933	-0.77	3.41
	400	12094	3121	-0.77	3.44
^{9}Be *	10	422	229	0.47	2.69
	50	1533	719	0.08	2.38
	100	2740	1143	-0.14	2.30
	160	3965	1510	-0.30	2.51
	200	4690	1757	-0.35	2.54
	260	5797	1998	-0.47	2.66
	300	6460	2142	-0.52	2.81
	360	7448	2347	-0.64	3.04
	400	7989	2473	-0.63	3.01
^{11}B **	10	361	196	0.53	2.89
		376	201	0.25	2.38
	50	1295	622	0.14	2.37
		1344	604	-0.14	2.28
	100	2328	1010	-0.07	2.38
		2391	927	-0.40	2.49

Ion	Energy (keV)	Rp (Å)	ΔRp (Å)	γ (Å)	ß (Å)
^{11}B 'cont.	150	3205	1310	-0.17	2.42
		3319	1158	-0.58	2.77
	200	4032	1574	-0.25	2.40
		4171	1342	-0.73	3.05
	250	4799	1755	-0.35	2.51
		4965	1492	-0.84	3.33
	300	5497	2000	-0.41	2.64
		5728	1611	-0.94	3.62
	350	6188	2103	-0.47	2.74
		6449	1715	-1.04	3.90
	400	6918	2242	-0.52	2.81
		7122	1809	-1.12	4.18
^{19}F **	10	232	132	0.61	3.00
		233	132	0.43	2.68
	50	803	422	0.37	2.65
		751	348	-0.02	2.32
	100	1444	692	0.16	2.40
		1285	533	-0.22	2.43
	150	2043	952	0.05	2.34
		1768	667	-0.39	2.59
	200	2611	1162	-0.01	2.33
		2197	770	-0.52	2.75
	250	3156	1349	-0.10	2.38
		2600	859	-0.61	2.93
	300	3715	1477	-0.20	2.43
		2976	933	-0.69	3.10
	350	4228	1641	-0.24	2.46
		3233	1010	-0.69	3.13
	400	4650	1813	-0.28	2.50
		3679	1050	-0.84	3.49
^{20}Ne *	10	221	126	0.68	3.15
	50	760	400	0.40	2.66
	100	1366	689	0.26	2.56
	180	2285	1065	0.06	2.37
	200	2517	1148	-0.01	2.38

Ion	Energy (keV)	Rp (Å)	ΔRp (Å)	γ (Å)	ß (Å)
^{20}Ne	250	3065	1346	-0.07	2.34
'cont.	300	3567	1524	-0.15	2.38
	350	4063	1671	-0.19	2.40
	400	4564	1834	-0.21	2.40
^{27}Al *	10	184	107	0.70	3.12
	50	628	351	0.56	2.95
	100	1145	615	0.39	2.59
	160	1749	899	0.24	2.44
	200	2196	1072	0.21	2.44
	260	2787	1309	0.07	2.39
	300	3172	1472	0.12	2.40
	360	3790	1682	-0.01	2.39
	400	4148	?851	-0.06	2.33
^{35}Cl *	10	144	89	0.78	3.56
	50	470	264	0.54	2.86
	100	827	435	0.38	2.70
	160	1263	641	0.25	2.51
	200	1528	745	0.18	2.46
	260	1954	905	0.08	2.42
	300	2218	1026	0.03	2.35
	360	2624	1163	0.01	2.39
	400	2884	1248	-0.05	2.42
^{114}Cd †	10	90	51	0.66	3.28
	50	208	114	0.60	3.18
	100	362	191	0.51	3.00
	150	510	260	0.44	2.90
	200	655	326	0.39	2.81
	250	798	390	0.35	2.78

Ion	Energy (keV)	Rp (Å)	ΔRp (Å)	γ (Å)	ß (Å)
^{114}Cd	300	939	451	0.32	2.75
'cont.	350	1079	510	0.29	2.71
	400	1219	567	0.26	2.69
^{115}In **	10	77	45	0.78	3.61
		89	51	0.66	3.28
	50	214	123	0.71	3.37
		205	112	0.61	3.20
	100	360	201	0.65	3.26
		355	187	0.51	3.02
	150	489	267	0.62	3.18
		500	255	0.45	2.92
	200	617	327	0.53	3.05
		641	319	0.40	2.85
	250	752	391	0.53	3.10
		781	382	0.36	2.79
	300	877	466	0.55	3.05
		893	443	0.39	2.82
	350	1012	521	0.44	2.84
		1016	497	0.36	2.78
	400	1128	578	0.42	2.76
		1139	550	0.38	2.75
^{130}Te †	10	87	49	0.65	3.28
	50	197	107	0.62	3.24
	100	338	176	0.53	3.06
	150	474	240	0.47	2.96
	200	607	300	0.42	2.89
	250	738	359	0.38	2.83
	300	867	415	0.35	2.79
	350	996	469	0.32	2.76
	400	1124	522	0.30	2.74

Ion	Energy (keV)	Rp (Å)	ΔRp (Å)	γ (Å)	ß (Å)
^{127}I [†]	10	87	49	0.65	3.28
	50	195	106	0.62	3.24
	100	334	174	0.53	3.05
	150	468	237	0.47	2.96
	200	598	297	0.42	2.89
	250	727	354	0.38	2.83
	300	855	410	0.35	2.79
	350	954	465	0.38	2.82
	400	1067	514	0.36	2.79

* TRIM only

** TRIM and BTE method

† BTE method only